博士論文

Production of Antihydrogen Beam and Development of Microwave Spectrometer to Measure the Lamb Shift

(反水素ビームの生成とラムシフト測定のための マイクロ波分光装置の開発)

Takumi TANAKA

田中 碧海

Graduate School of Arts and Sciences, The University of Tokyo

東京大学大学院
総合文化研究科 広域科学専攻相関基礎科学系

December 9, 2024

2024年 12月 9日

Contents

List of Figures

List of Tables

Chapter 1

Introduction

1.1 The Lamb Shift

In 1947, W. E. Lamb and R. C. Retherford carried out microwave (MW) spectroscopy on a hydrogen atom (H) where the magnetic field strength was varied, to find an energy split of around 1.05 GHz between the $2S_{1/2}$ and $2P_{1/2}$ levels [1, 2].

While the Dirac equation explains the energy split between $2P_{1/2}$ and $2P_{3/2}$ levels of H atom caused by spin-orbit interaction, it cannot describe the removal of degeneracy between the $2S_{1/2}$ and $2P_{1/2}$ levels. Shortly after Lamb and Retherford's experiment, H. A. Bethe's theory, which considered the difference between the self-interaction of the electron in the hydrogen atom and that of a free electron, explained the mechanism of the Lamb shift [3].

This work paved a way to the renormalization theory, and quantum electrodynamics (QED), which integrated quantum mechanics and electromagnetism and was completed by S. Tomonaga, R. P. Feynman, J. Schwinger, and others. Today, the Lamb shift has been understood in the theory of quantum electrodynamics (QED), as an energy split contributed by such perturbative effects as electron's self-energy, vacuum polarization, nuclear recoil effect, and so on.

1.2 PCR and Recent Measurements of Lamb Shift

Besides the QED effects, further contributions to the Lamb shift start to be seen in high-precision measurements. The leading-order of such contribution is known as the finite nuclear size effect E_{FNS}, which is formulated for a hydrogen-like atom as [4]:

$$E_{\mathrm{FNS}} = \frac{2}{3}\frac{(Z\alpha)^4}{n^3}\left(\frac{m_r}{m}\right)^3 R_C^2 \delta_{\ell 0} \tag{1.1}$$

where R_C is the root-mean-square (rms) charge radius of the nucleus:

$$R_{\mathrm{C}}{}^2 = \int d^3 r r^2 \rho(r) \tag{1.2}$$

and $\rho(r)$ is the nuclear charge distribution. Z, α, n, m_r, m, and δ_{l0} stand for the atomic number, fine structure constant, principle quantum number, reduced mass, electron mass, and Kronecker-delta, respectively. Relativistic units are taken here. In the case of a H atom, $R_{\mathrm{C}}{}^2$ corresponds to the proton charge radius (PCR), which was first determined by an electron scattering experiment to be around 1 fm in 1955 [5].

Along with the progress of MW technology, high-precision spectroscopic measurements of the $2S_{1/2} - 2P_{1/2}$ Lamb shift in H atoms demonstrated determination of the PCR [6, 7]. In the highest precision Lamb shift spectroscopy, adopting the frequency-offset separated oscillatory field (FOSOF) method — an advanced technique of Ramsey method [8] — the resonance frequency was measured to a precision of 3 ppm, with the PCR determined to a precision of 1% [9].

Furthermore, by utilizing a muonic hydrogen (μp) atom — a two body system of a proton and a muon — ultra high-precision spectroscopic measurements of the Lamb shift were achieved [10,11], and the PCR has been determined most accurately as 0.840 87(39) fm [11] among all the experiments conducted so far.

In the case of a H atom, by substituting this PCR value of the highest precision to Equation (1.1), the frequency shift due to $E_{\rm FNS}$ was calculated as 0.138 45(13) MHz [4]. Including this shift, contributions of the QED effects to the $2S_{1/2}$ - $2P_{1/2}$ Lamb shift are tabulated in Table 1.1.

Table 1.1: Contributions of the QED effects and $E_{\rm FNS}$ to the $2S_{1/2}$ - $2P_{1/2}$ Lamb shift in MHz, adapted from Table 7 in Reference [4].

Contribution	$2S_{1/2}$	$2P_{1/2}$	$2S_{1/2} - 2P_{1/2}$
SE	1072.958 455	−12.858 661 (1)	1085.817 116 (1)
Ue	−26.897 303	−0.000 347	−26.896 956
WK	0.000 302	0	0.000 302
Ue(μhad)	−0.001 06 (1)	0	−0.001 06 (1)
SESE	0.292 48 (16)	0.027 253 (4)	0.265 23 (16)
SEVP	0.036 015 (20)	−0.001 241	0.037 256 (20)
VPVP	−0.236 911	−0.000 003	−0.236 908
QED(ho)	0.000 23 (12)	−0.000 216	0.000 45 (12)
RRM	−1.633 931	0.011 741	−1.645 672
REC	0.340 469	−0.016 656	0.357 125
REC(ho)	−0.003 227 (92)	−0.001 335 (4)	−0.001 892 (92)
$E_{\rm FNS}$	0.138 45 (13)	0	0.138 45 (13)
NUCL5	−0.000 014	0	−0.000 014
NUCL6	0.000 140 (49)	0.000 001	0.000 139 (49)
FNS(rad)	−0.000 017	0	−0.000 017
NSE	0.000 585 (20)	0.000 001 (20)	0.000 584 (28)
Total	1044.994 66 (23)(13)	−12.839 463 (21)(0)	1057.834 12 (31)(13)

All the values in the column $2S_{1/2}$ and $2P_{1/2}$ are adapted from Table 7 in Reference [4], which summarized the following QED effects:

- SE (Self-Energy):
  Interaction of the electron with its own electromagnetic field.
- Ue (Uehling):
  Vacuum polarization effects from virtual electron-positron pairs.
- WK (Wichmann-Kroll):
  Higher-order vacuum polarization effects.
- Ue(μhad) (Muon and Hadronic Vacuum Polarization):
  Contributions from virtual muon pairs and hadronic effects.
- SESE (Two-Loop Self-Energy):
  Complex interactions between the electron and its field, including second-order effects.
- SEVP (Self-Energy with Vacuum Polarization):
  Interaction between the electron's self-energy and vacuum polarization effects.
- VPVP (Two-Loop Vacuum Polarization):
  Higher-order vacuum polarization effects involving multiple virtual particles.

- QED(ho) (Higher-Order QED Effects):
  Various higher-order quantum electrodynamics corrections.
- RRM (Relativistic Reduced Mass):
  Relativistic effects due to the reduced mass of the electron-nucleus system.
- REC (Recoil Correction):
  Motion of the nucleus in response to the electron's movement.
- REC(ho) (Higher-Order Recoil Correction):
  Higher-order corrections to the recoil effect.
- FNS (Finite Nuclear Size):
  The nucleus is not a point particle but has a finite size.
- NUCL5 (Fifth-Order Nuclear Correction):
  Fifth-order corrections related to nuclear effects.
- NUCL6 (Sixth-Order Nuclear Correction):
  Sixth-order corrections related to nuclear effects.
- FNS(rad) (Radiative Finite Nuclear Size):
  Radiative effects combined with the finite size of the nucleus.
- NSE (Nuclear Self-Energy):
  Energy shift due to the nucleus's own electromagnetic field.

Then, the last column shows the values in $2S_{1/2}$ state subtracted from the values in $2P_{1/2}$ state. At the last row, the total values of each contribution are given, with the value in the first bracket representing the theoretical uncertainty and the value in the second bracket representing the uncertainty of the frequency shift due to the E_{FNS} measured in Reference [11]. In this evaluation, the resonance frequency of $2S_{1/2}$ - $2P_{1/2}$ Lamb shift transition in H atoms is computed to be 1057.834 12 (31)(13) MHz.

1.3 PCR Puzzle

Prior to the 2000's, a number of groups measured the PCR in electron-proton (e-p) scattering experiments and spectroscopy experiments using H atoms, yielding an average value of about 0.88 fm. In 2010, however, the μp Lamb shift spectroscopy experiment was conducted for the first time and reported an ultra precise PCR value of 0.841 84(67) fm [10], which was significantly smaller than the conventional value around 0.88 fm. Since a muon is 207 times more massive than an electron, a μp atom has S state wave functions distributed closer to the proton. Consequently, the screening effect arising from the finite charge distribution of the proton is amplified, allowing for a very precise determination of the PCR. This report prompted additional measurements as well as re-analyses of the past measurements.

Figure 1.1 shows the PCR values obtained from these post-2010 measurements. The data point on the top represents the CODATA 2010 recommended value determined by conventional e-p scattering and spectroscopic studies on H atoms [12]. The next value is from the μp Lamb shift spectroscopy, which first reported the smaller PCR [10] and motivated additional measurements. The first measurement after the discovery of the smaller PCR was made by an e-p scattering experiment, which reported a value supporting the conventional PCR [13], represented as the third data point from the top. Shortly after, however, the μp Lamb shift spectroscopy group updated their value represented as the forth data point from the top, which has given the most precise PCR of 0.840 87(39) fm so far [11]. In 2017, a $2S$ - $4P$ spectroscopy experiment on H atoms reported a smaller PCR [14] for the first time. The next value, from a $1S$ - $3S$ spectroscopy experiment in 2018, supported the conventional PCR [15]. The following value is derived from re-analysis

by A. Marsman and E.A. Hessels et al. [16] on the value obtained from the H Lamb shift spectroscopy in 1981 [7]. Shortly after the re-analysis, Hessels's group performed the highest precision H Lamb shift spectroscopy [9] adopting the FOSOF method, which supported the smaller PCR. In 2019, a new e-p scattering [17] experiment was conducted to find the smaller PCR. The next two values are from a new $1S$ - $3S$ [18] and $2S$ - $8D$ [19] spectroscopic studies on H atoms, both of which are a little off from the smaller PCR. The last value is the CODATA 2022 recommended value of 0.840 75(64) fm [20], which is represented as the vertically filled area as a reference.

While recent multiple works support the smaller PCR, some others still favor the larger PCR or disagree to the smaller PCR. The debate remains unsettled, and the PCR puzzle continues to be actively discussed.

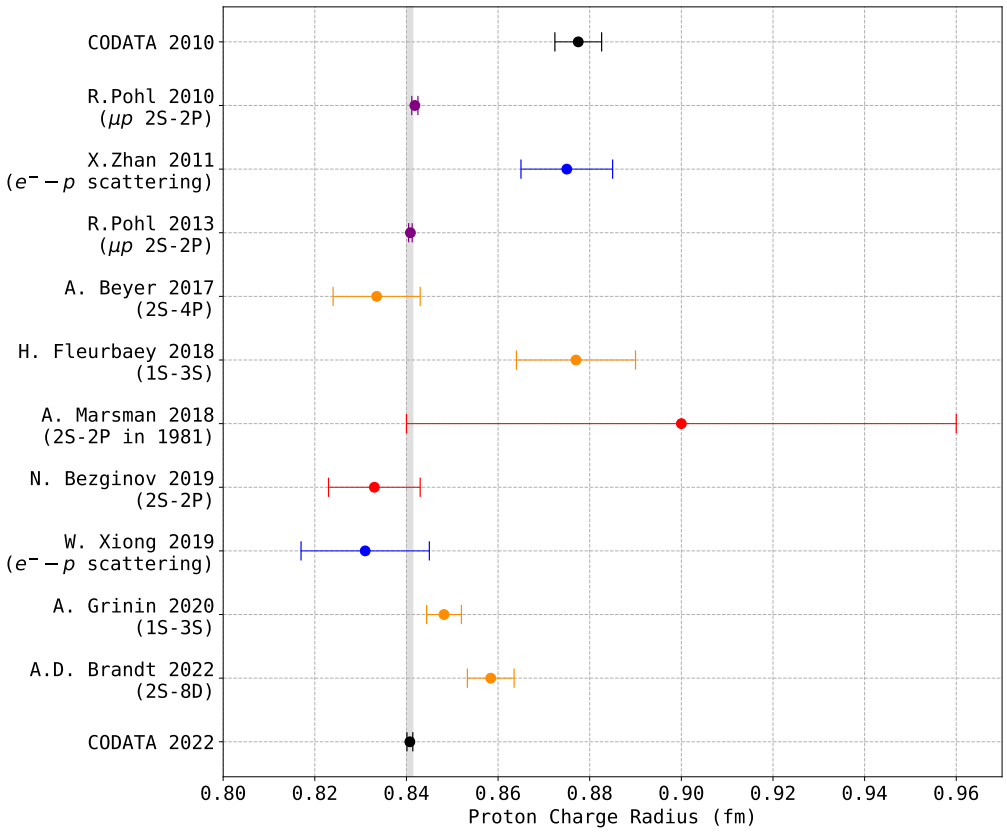

Figure 1.1: Measured values of the PCR. See the text for details.

1.4 CPT symmetry and Antihydrogen Atom

Local quantum field theory is a fundamental theoretical framework in modern physics, which incorporates Lorentz symmetry as a postulate, ensuring that the laws of physics remain consistent across all inertial reference frames.

In local quantum field theory, CPT symmetry — the invariance of physical laws under the simultaneous transformation of charge conjugation, parity inversion, and time reversal — emerges as a consequence of Lorentz invariance, locality, and unitarity. This theory serves as the foundation for the standard-model of particle physics. Under CPT symmetry, the fundamental quantities of particles are supposed to be identical to those of antiparticles, such as mass, lifetime, and so on.

Meanwhile, a theoretical framework was proposed to incorporate microscopic CPT and Lorentz violating effects into the standard-model [21, 22]. This framework, known as the standard-model extension, allows for additional terms in the Lagrangian of the standard model, resulting in a modified Dirac equation:

$$\left(\mathrm{i}\gamma^{\mu}D_{\mu} - m_{\mathrm{e}} - a^{\mathrm{e}}_{\mu}\gamma^{\mu} - b^{\mathrm{e}}_{\mu}\gamma_5\gamma^{\mu} - \frac{1}{2}H^{\mathrm{e}}_{\mu\nu}\sigma^{\mu\nu} + \mathrm{i}c^{\mathrm{e}}_{\mu\nu}\gamma^{\mu}D^{\nu} + \mathrm{i}d^{\mathrm{e}}_{\mu\nu}\gamma_5\gamma^{\mu}D^{\nu}\right)\Psi = 0 \tag{1.3}$$

where γ^{μ} represents the Dirac matrices, m_{e} denotes the electron mass, $D_{\mu} = \partial_{\mu} - \mathrm{i}qA_{\mu}$ serves as the covariant derivative with q representing the charge and A_{μ} the Coulomb potential. The fifth Dirac matrix is represented by γ_5, while $\sigma^{\mu\nu} = \frac{\mathrm{i}}{2}[\gamma^{\mu}, \gamma^{\nu}]$ generates the Lorentz group in the spinor representation. The coefficients $a^{\mathrm{e}}_{\mu}, b^{\mathrm{e}}_{\mu}, c^{\mathrm{e}}_{\mu\nu}, d^{\mathrm{e}}_{\mu\nu}, H^{\mathrm{e}}_{\mu\nu}$ represent Lorentz-violating parameters. Among these coefficients, a^{e}_{μ} and b^{e}_{μ} also violate CPT symmetry. The state of the field is denoted by Ψ. This modified Dirac equation can be applied to other fermions as well. For free protons, the coefficients are adjusted accordingly:

$$a^{\mathrm{e}}_{\mu} \to a^{\mathrm{p}}_{\mu}, \quad b^{\mathrm{e}}_{\mu} \to b^{\mathrm{p}}_{\mu}, \quad c^{\mathrm{e}}_{\mu\nu} \to c^{\mathrm{p}}_{\mu\nu}, \quad d^{\mathrm{e}}_{\mu\nu} \to d^{\mathrm{p}}_{\mu\nu} \tag{1.4}$$

This generalized framework calls for stringent experimental test of Lorentz and CPT symmetry violations in various particle sectors.

In this context, an antihydrogen ($\bar{\mathrm{H}}$) atom — the simplest anti-atom system composed of an antiproton ($\bar{p}$) and a positron (e^+) — serves as a promissing experimental probe for testing fundamental symmetries between matter and antimatter. Such tests put constraints on the coefficients in the standard model extension such as the one in Equation (1.3) [22].

$\bar{\mathrm{H}}$ atoms were first produced at the Low Energy Antiproton Ring (LEAR) facility at CERN, located near Geneva, Switzerland [23]. This was followed by an observation at Fermi National Accelerator Laboratory [24].

After the LEAR facility, the Antiproton Decelerator (AD) / Extra Low ENergy Antiproton (ELENA) facility [25–27] started to operate in CERN, which provides an $\bar{p}$ beam with a relatively low kinetic energy of 100 keV.

At the AD/ELENA facility, various groups have been conducting fundamental physics experiment on $\bar{\mathrm{H}}$ atoms, such as ALPHA [28] and ASACUSA [29–31] for spectroscopic measurements.

Recently, spectroscopic studies on $\bar{\mathrm{H}}$ atoms under a high magnetic field by the ALPHA collaboration have reported the resonance frequencies of ground state hyperfine structure transition ν_{GSHFS} [32], $1S$-$2S$ two photon transition ν_{1S-2S} [33], and $1S$-$2P$ Lyman-α transition ν_{1S-2P} [34] as follows:

$$\nu_{\mathrm{HFS}} = 1420.4(5)\,\mathrm{MHz} \tag{1.5}$$

$$\nu_{1S-2S} = 2466061103079.4(5.4)\ \mathrm{kHz} \tag{1.6}$$

$$\nu_{1S-2P} = 2\,466\,051.70(12)\,\mathrm{GHz} \tag{1.7}$$

Furthermore, from the measurement results of ν_{1S-2S} and ν_{1S-2P}, the resonance frequencies of the $2S_{1/2}$ - $2P_{3/2}$ fine structure transition $\nu_{2S_{1/2}-2P_{3/2}}$ [35] and the $2S_{1/2}$ - $2P_{1/2}$ Lamb shift transition ν_{Lamb} [35] were reported to be:

$$\nu_{2\mathrm{S}_{1/2}-2\mathrm{P}_{3/2}} = 10.88(19)\,\mathrm{GHz} \tag{1.8}$$

$$\nu_{\mathrm{Lamb}} = 0.99(11)\,\mathrm{GHz} \tag{1.9}$$

Besides the spectroscopic studies, measurements of the gravitational response of $\bar{\mathrm{H}}$ atoms are also in progress by a couple of groups at the AD/ELENA facility such as ALPHA-g [28], GBAR [36–39], and AEgIS [40–42]. These measurements are aimed to test the Weak Equivalence Principle (WEP).The world first observation of $a_{\bar{g}}$ — the gravitational acceleration of $\bar{\mathrm{H}}$ atoms under the Earth's gravitational field — was accomplished by ALPHA-g in 2023 [43], to find:

$$a_{\bar{g}} = (0.75 \pm 0.13\,(\mathrm{statistical} + \mathrm{systematic}) \pm 0.16\,(\mathrm{simulation}))g \tag{1.10}$$

where g denotes the gravitational constant of $9.81\,\mathrm{ms}^{-2}$.

1.5 Motivation of Research

In the context that the PCR has been actively investigated by a variety of methods including the Lamb shift spectroscopy, and that spectroscopic studies on the $\bar{\mathrm{H}}$ atoms have been achieved at the AD/ELENA facility, this research aims to perform high-precision spectroscopy of the $2S_{1/2}$-$2P_{1/2}$ Lamb shift transition in $\bar{\mathrm{H}}$ atoms.

While the ALPHA collaboration has indirectly determined the Lamb shift transition frequency of $\bar{\mathrm{H}}$ atoms to be 0.99(11) GHz by comparing their results of laser spectroscopy under a high magnetic field environment [35], direct MW spectroscopy of the Lamb shift in $\bar{\mathrm{H}}$ atoms for precision measurements has not yet been attempted, and the antiproton charge radius has not yet been experimentally investigated.

In the GBAR experiment [36–39] a beam-like $\bar{\mathrm{H}}$ atom has been produced via a charge-exchange reaction with a positronium atom (Ps) — a bound state of e^- and e^+ — and an $\bar{p}$ with a kinetic energy at a few keV [44]. Under this production scheme, theoretical calculations predict the presence of $2S$ state $\bar{\mathrm{H}}$ atoms [45]. Moreover, this atomic beam of $\bar{\mathrm{H}}$ atoms are transported through a magnetic field-free environment.

As such, we have proposed a direct MW spectroscopy of the $2S_{1/2}$ - $2P_{1/2}$ Lamb shift transition in $\bar{\mathrm{H}}$ atoms in the GBAR $\bar{\mathrm{H}}$ beam line [46, 47]. This will be the world's first attempt of direct MW spectroscopy of the Lamb shift transition in $\bar{\mathrm{H}}$ atoms, and a high-precision result is expected. Furthermore, this study could contribute to the verification of CPT symmetry through a comparison of the PCR and antiproton charge radius.

Chapter 2

The GBAR Experiment

2.1 $\bar{p}$ Beam From AD/ELENA

The AD facility at CERN, is the only facility in the world capable of providing a low-energy $\bar{p}$ beam. At the AD facility, the $\bar{p}$ beam is decelerated through repeated stochastic and electron cooling down to a kinetic energy of 5.3 MeV. Moreover, the ELENA facility has begun operation, which further decelerates and cools the $\bar{p}$ beam from the AD down to 100 keV.

Through the transfer lines shown in Figure 2.1, each experiment at the AD/ELENA facility receives the pulsed $\bar{p}$ beam with a kinetic energy of 100 keV, and a bunch length of about 150 ns as a full width half maximum (FWHM) [26, 27], almost every 110 seconds. The intensity of the $\bar{p}$ beam provided to each experiment reached 11×10^6 stably as of 2024, and has been improving. Concerning the LNE50 transfer line, which connects to the GBAR experiment, the horizontal and vertical emittances at the extraction from the ELENA were measured by the ELENA team in 2022 to be 2.9 mm mrad and 2.1 mm mrad, respectively. These values are 2.5 times larger than the design value [25].

Additionally, a negative hydrogen ion (H^-) beam with similar beam characteristics to the $\bar{p}$ beam can be supplied almost every 15 seconds as needed, allowing for a fast optimization of the beam transport parameters at each experiment.

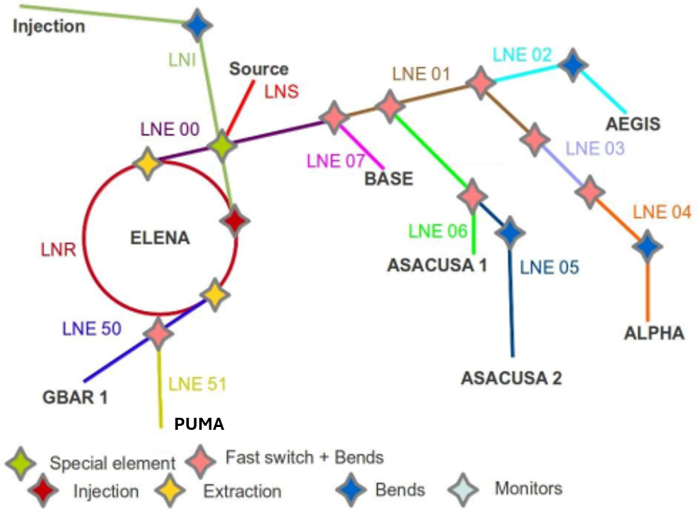

Figure 2.1: Scheme of the AD/ELENA facility including beam transfer lines to each experiment.

2.2 Goal of GBAR

The GBAR (Gravitational Behaviour of Antihydrogen at Rest) experiment [36–39] aims to observe the free fall of $\bar{H}$ atoms cooled to several μK and measure the gravitational acceleration $\bar{g}$ on antimatter with a precision of 1% . The objective of this experiment is to directly test the WEP, which states the equivalence of motion in a gravitational field for any object including antimatter.

Adopting an $\bar{H}$ atom as a probe for measuring such gravitational free-fall motion has several advantages. Firstly, $\bar{H}$ atoms are electrically neutral, thus less susceptible to electromagnetic fields compared to charged antiparticles such as an $\bar{p}$ or a e^+. Additionally, $\bar{H}$ atoms theoretically have an infinite lifetime, allowing for longer measurement durations compared to neutral particle-antiparticle bound systems like Ps atoms.

In the GBAR experiment, an $\bar{H}^+$ ion, which contains one extra e^+, is to be produced and trapped in an radio frequency (RF) ion trap. The $\bar{H}^+$ ion undergoes sympathetic cooling with beryllium ions (Be^+) and Raman sideband cooling to achieve ultra-low temperatures below the recoil limit at μK levels. Finally, the extra e^+ is dissociated using a laser, enabling a precise measurement of the free-fall motion of the $\bar{H}$ atom.

2.3 Cross-sections of $\bar{H}/\bar{H}^+$ Formation

In ALPHA or ASACUSA, $\bar{H}$ atoms are synthesized via the three body recombination process of one $\bar{p}$ and two e^+s by mixing each of them as a non-neutral plasma. In contrast, in the GBAR experiment, a cloud of Ps atoms in the ground state or low-lying excited state is first prepared, then $\bar{p}$s are injected as a beam with a kinetic energy of several keV, to synthesize the $\bar{H}$ atoms or $\bar{H}^+$ ions via the following two-stage consecutive charge-exchange reactions:

$$\bar{p} + \mathrm{Ps} \longrightarrow \bar{H} + e^- \tag{2.1}$$

$$\bar{H} + \mathrm{Ps} \longrightarrow \bar{H}^+ + e^- \tag{2.2}$$

This production scheme is predicted to result in high cross-sections of $\bar{H}$ atom formation in low-lying excited state, while the three body recombination process leads to synthesizing a large amount of $\bar{H}$ atoms in the Rydberg states.

Figure 2.2(a) shows theoretical cross-sections of the $\bar{H}$ atom formation in different low-lying excited state via the first reaction expressed by Equation (2.1) [45] assuming a reaction with the ground state Ps, calculated by the Close Coupling method [45]. The cross-sections were calculated as a function of the kinetic energy of the incident $\bar{p}$. In Figure 2.2(a), around 6 keV, the total cross-section of $\bar{H}$ formation is $13.4 \times 10^{-16}\mathrm{cm}^2$, while another work based on the Coulomb-Born approximation predicts a value of $30.6 \times 10^{-16}\mathrm{cm}^2$ [48].

In the case of $\bar{H}(2S)$ formation, in Figure 2.2(a), the cross-section peaks around 6 keV with a value of $1.87 \times 10^{-16}\mathrm{cm}^2$, while the Coulomb-Born approximation predicts a value of $6.01 \times 10^{-16}\mathrm{cm}^2$ [48].

Given the cross-section by the Close Coupling method, about 15% of the total $\bar{H}$ atoms produced via the reaction are expected to be $\bar{H}(2S)$ at the incident energy of 6 keV [45], which will be available for the Lamb shift spectroscopy.

Concerning the $\bar{H}^+$ ion formation via the second reaction expressed by Equation (2.2), Figure 2.2(b) shows theoretical cross-sections for $\bar{H}(1S)$ (black) and $\bar{H}(2S)$ (blue) incident on Ps(1S) [49]. For each state of the $\bar{H}$ atom, cross-sections calculated by using the Le

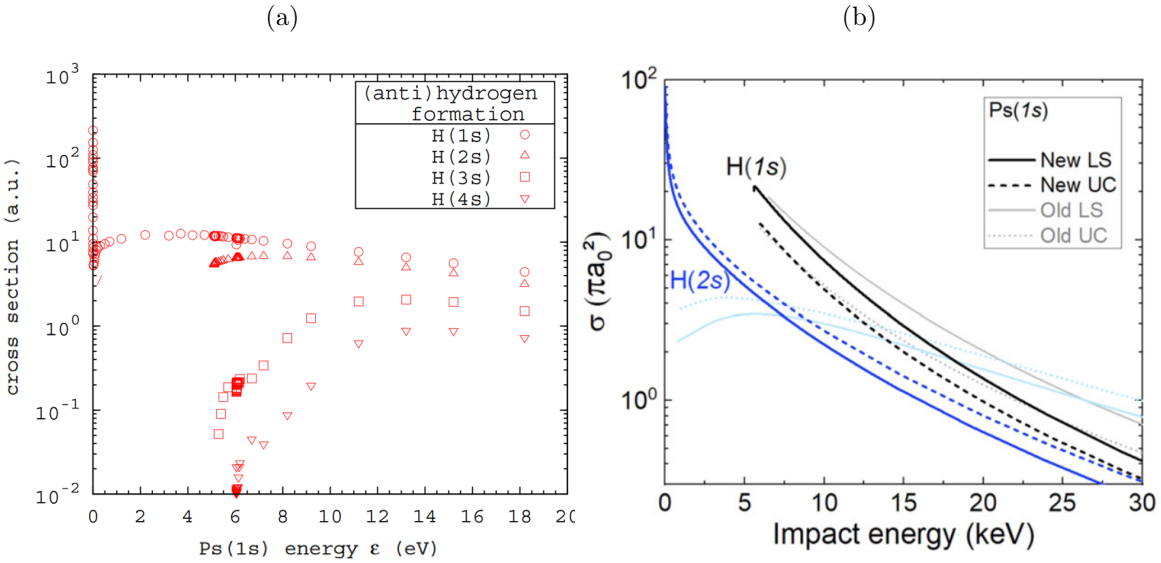

Figure 2.2: Theoretical cross-sections of (a) $\bar{H}$ atom formation in low-lying excited state via the first reaction shown in Equation (2.1), adapted from Reference [45], and (b) $\bar{H}^+$ ion formation via the second reaction shown in Equation (2.2) assuming $\bar{H}$(1S) and $\bar{H}$(2S) incident on Ps(1S), adapted from Reference [49]

Sech (LS) wave function (the solid curve) and uncorrelated Chandrasekhar (UC) wave function (the dashed curve) are displayed. In addition, 'New' and 'Old' (in lighter shades) calculation results are shown for each case. The 'Old' results are from Reference [50–52]. These works were corrected given Reference [53], and the corrected calculations described in Reference [49] are shown as the 'New' results. One can see that the cross-section of $\bar{H}^+$ ion formation increases towards the reaction threshold around 5.6 keV. Further works to calculate cross-sections related to this reaction can be found in Reference [54, 55].

Needless to say, experimental verifications of the theoretical cross-section in these charge-exchange reactions themselves are of interest. In the $\bar{H}$ production experiment in 2022 [44], a lower limit of the cross-section in the first reaction (2.1) with 6.1 keV $\bar{p}$ and Ps(1S) was evaluated to be $11(5) \times 10^{16}$ cm^2 in Reference [56]. For the charge conjugate version of the first reaction (2.1), cross-section measurements were performed in 1997 using a proton beam incident on a Ps target at 11.3 keV, 13.3 keV, and 15.8 keV [57]. Besides, the SPHINX project [58] in the GBAR collaboration aims at measuring the cross-section in the charge conjugate version of the second reaction (2.2) by producing a H beam from the H^- ion beam provided by the ELENA facility.

2.4 Reaction Target

The consecutive charge-exchange reactions take place either on the flat target illustrated in Figure 2.3(a) or inside the cavity target illustrated in Figure 2.3(b). In Figure 2.3, the part denoted as 'Converter(s)' is made of a nanoporous silica layer. The e^+ beam is implanted onto this layer with an incident energy of a few keV, and Ps atoms are formed inside the layer. After a few ns, only the ortho-positronium (oPs) atoms — having a life time of 142 ns while the para-positronium has a life time of only 125 ps — make it back to the surface of the layer and form a cloud, which starts thermally diffusing in the vacuum. In the case of the cavity target, the Ps cloud can be confined and participate in the charge-exchange reactions with a higher density than the case of using the flat target.

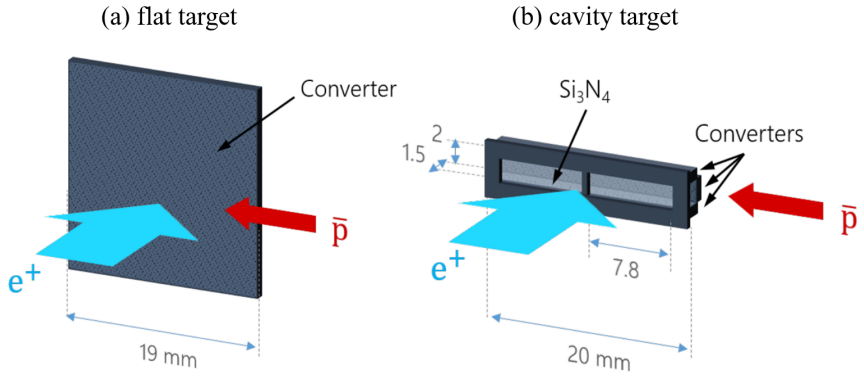

Figure 2.3: Schemes of the (a) flat target and (b) cavity target, adapted from Reference [59].

These targets were attached on a movable holder shown in Figure 2.4. The flat target and cavity target are the second and third component from the bottom illustrated respectively in the scheme on the left side in Figure 2.4. Right behind each target, there is an electrostatic deflector to remove the $\bar{p}$ beam for reducing background for an $\bar{H}$ detector downstream when the experiment is focused on the $\bar{H}$ detection. The target holder was installed inside the reaction chamber schematically represented in Figure 2.5.

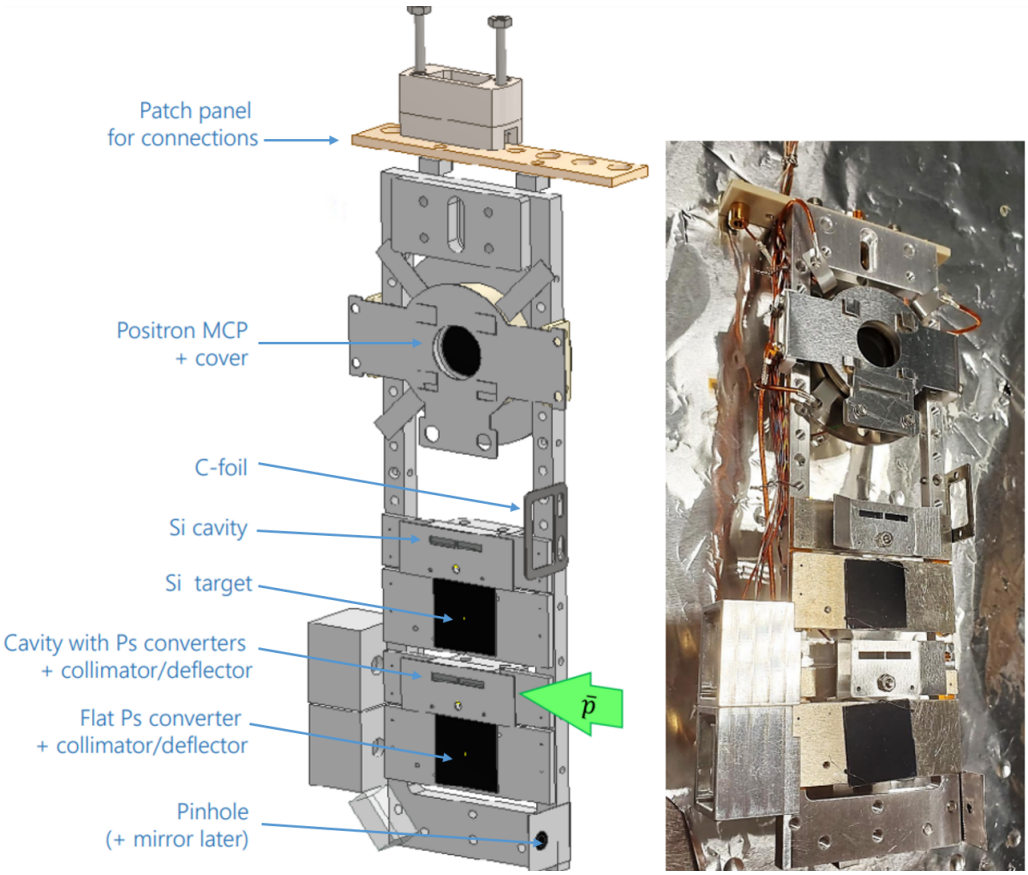

Figure 2.4: Scheme and Photograph of the target holder.

2.5 The GBAR Beam Line

Figure 2.5 shows the scheme of the GBAR beam line at the final phase of the experiment set for measuring the gravitational acceleration $\bar{g}$.

The 100 keV $\bar{p}$ beam from the ELENA first gets decelerated by a drift tube decelerator [56, 61]. In 2023, a Penning-Malmberg trap [62] started operations to trap the decelerated $\bar{p}$. The $\bar{p}$s are cooled, bunched, and extracted to the reaction target.

The e^+ beam is generated by using an electron linear RF accelerator (LINAC) with a relatively low electron energy of 9 MeV [63]. The generated e^+ beam is accumulated by using two Penning-Malmberg traps [64]. The first trap is a Surko-Greaves type buffer gas trap (BGT) [65, 66] The second trap, called high field trap (HFT), accumulate e^+s on the order of 10^8 during the AD cycle of 110 seconds [67]. The trapped e^+s are then extracted towards the field-free region around the reaction target [68] to be implanted onto the reaction target.

Inside the reaction chamber in Figure 2.5, the movable target holder shown in Figure 2.4 is installed, and the charge-exchange reactions expressed by Equation(2.1, 2.2) take place. After the reaction target, the $\bar{p}$, $\bar{\mathrm{H}}$ atom, and $\bar{\mathrm{H}}^+$ ion pass through the Lamb shift setup and their trajectories are separated by an electrostatic switchyard, to transport the $\bar{\mathrm{H}}^+$ ion to the free fall chamber, where the apparatuses and detectors will be installed for the gravitational free-fall measurement.

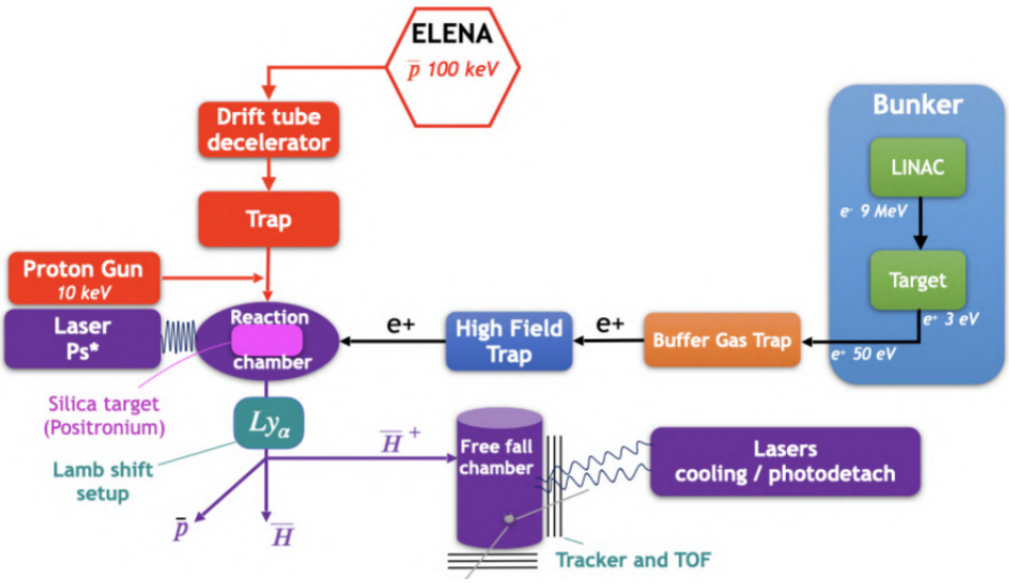

Figure 2.5: Scheme of the GBAR beam line at the final stage, adapted from Reference [60].

2.5.1 $\bar{p}/\bar{\mathrm{H}}$ Beam Line

The 100 keV $\bar{p}$ beam from the ELENA is slowed down to several keV by the drift tube decelerator, as illustrated in Figure 2.6 which is seen from the side. All the dimensions in the figure are in mm. The x-axis and z-axis at the bottom left in the figure denote the $\bar{p}$ beam axis and the vertical axis, respectively. The $\bar{p}$ beam first gets focused by a triplet of electrostatic lenses ('V0, V1, V2'), or an Einzel lens (EL), and injected to the drift tube ('Drift Tude'). There used to be one more EL right before the drift tube in 2022, as in the original design [61]. However, it was removed in 2023 given the analysis described in

Reference [56].

A specific value of high voltage is applied on the drift tube in advance, and rapidly switched to the ground at the arrival time of the incident $\bar{p}$ beam to decelerate the $\bar{p}$ beam to the desired value of kinetic energy. Decelerations down to 3 keV were stably achieved as of 2024.

After the drift tube, another EL ('EL out') and an electrostatic steerer ('Steerer Decel') are available to compensate the divergence of the decelerated beam and adjust the trajectory. The beam is then transported to the $\bar{p}$ trap.

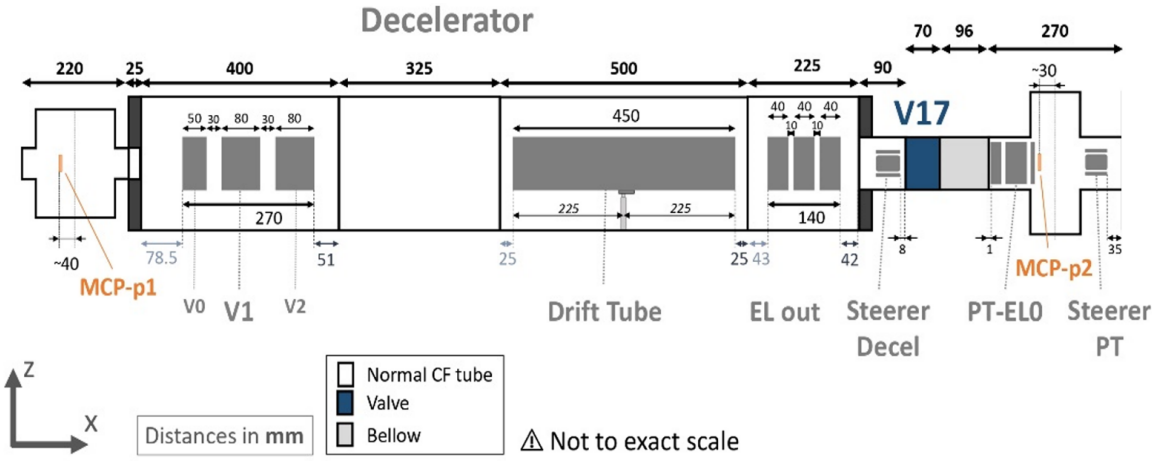

Figure 2.6: Scheme of the drift tube decelerator updated in 2023.

Figure 2.7 shows a cross sectional side view of the $\bar{p}$ trap and the beam line before and after. The design of the trap is based on the MUSASHI trap from ASACUSA [69], which is further based on the $\bar{p}$ trap from ALPHA. A uniform magnetic field with a central field strength of 5 T is formed by a superconducting solenoid magnet cooled by a Gifford-McMahon (GM) cryocooler. The incident $\bar{p}$ beam is first trapped by using the high voltage (HV) electrodes and the multi ring electrode ('MRE'). For an efficient trapping, the $\bar{p}$ beam decelerated down to 3 keV is injected to the trap, and the trapping HVs are set at 8 kV. The trapped $\bar{p}$s are then cooled for 5 seconds with electrons on the order of 10^8, which are pre-loaded inside a harmonic potential well of a depth of 140 V and a width of around 100 mm formed by the MRE.

One of the ring electrode in the MRE is divided into four segments radially. By applying RF signals phased at intervals of $\pi/4$, a rotating E-field is formed to compress the $\bar{p}$ plasma radially while performing the electron cooling. This is known as the rotating wall (RW) technique [70, 71]. The radial compression is typically performed with the RF signal of 8 MHz and 10 V. Once the cooling and compression are completed, electrons are first kicked out. Then, the $\bar{p}$s are bunched, focused, and extracted towards the reaction chamber. The bunch length after the extraction at 6 keV was preliminarily measured as 150 ns as FWHM, which is almost the same value as that of the 100 keV $\bar{p}$ beam from the ELENA.

Figure 2.8 shows the beam line components seen from above after the $\bar{p}$ trap till the end of the $\bar{\text{H}}$ beam line. The $\bar{p}$ beam extracted from the trap first passes through an EL ('QB-EL') and a steerer ('Steerer QB'), and its trajectory is further adjusted by an electrostatic quadrupole triplet ('Quad-Triplet') and another steerer ('Steerer QT'). Finally, the $\bar{p}$ beam is injected to the reaction chamber ('Reaction Chamber').

Inside the reaction chamber, there is an iris diaphragm ('Iris') to cut the halo of the

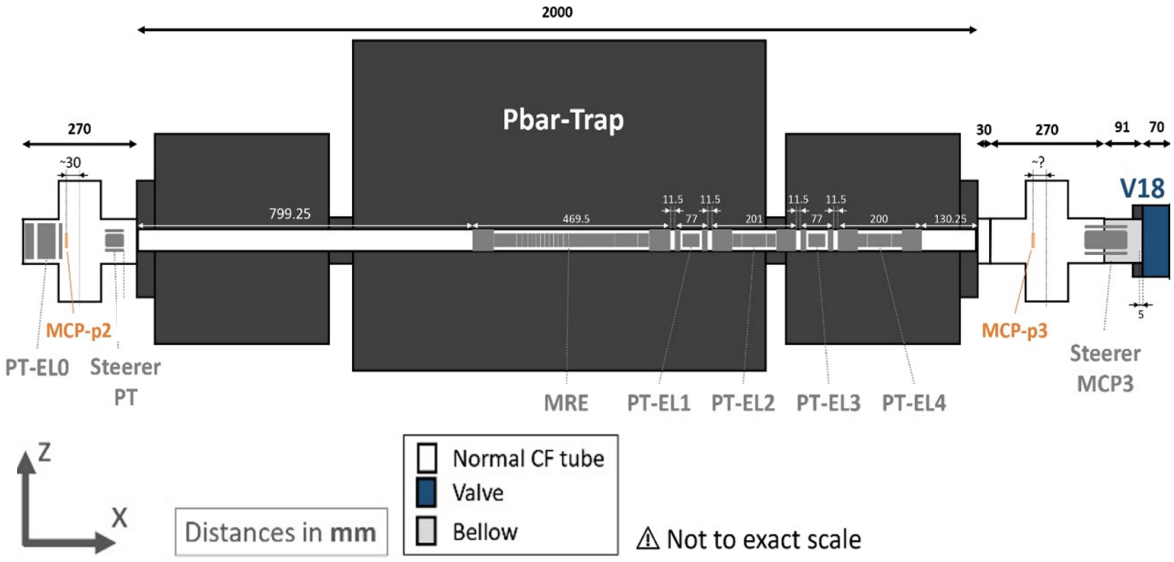

Figure 2.7: Scheme of the $\bar{p}$ trap in the GBAR experiment.

$\bar{p}$ beam, which is followed by the reaction target ('Target') attached on the target holder shown in Figure 2.4. A photograph of the iris diaphragm and target holder is shown in Figure 2.9. The component between the iris and target holder is an assembly of high voltage electrodes and Faraday cup to be used in the SPHINX project [58].

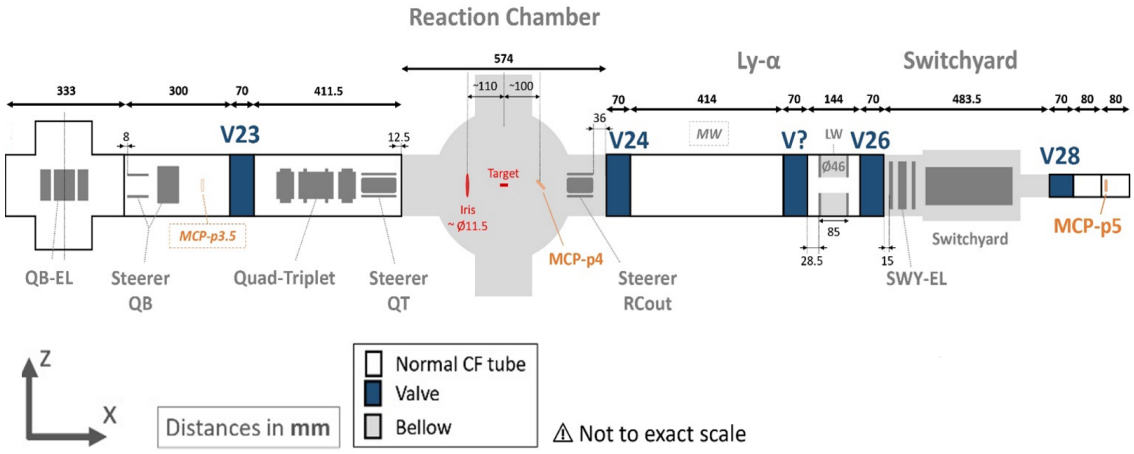

Figure 2.8: Scheme of the $\bar{p}$ beam line after the $\bar{p}$ trap until the end of the $\bar{H}$ beam line.

After the reaction chamber, there are a vacuum chamber ('MW') to house a MW spectrometer, and a Lyman-α photon detector ('Ly-α') for the Lamb shift spectroscopy, which are followed by an electrostatic switchyard ('Switchyard') and an $\bar{H}$ detector ('MCP-p5'). Concerning these components, detailed descriptions are given in Section 3.

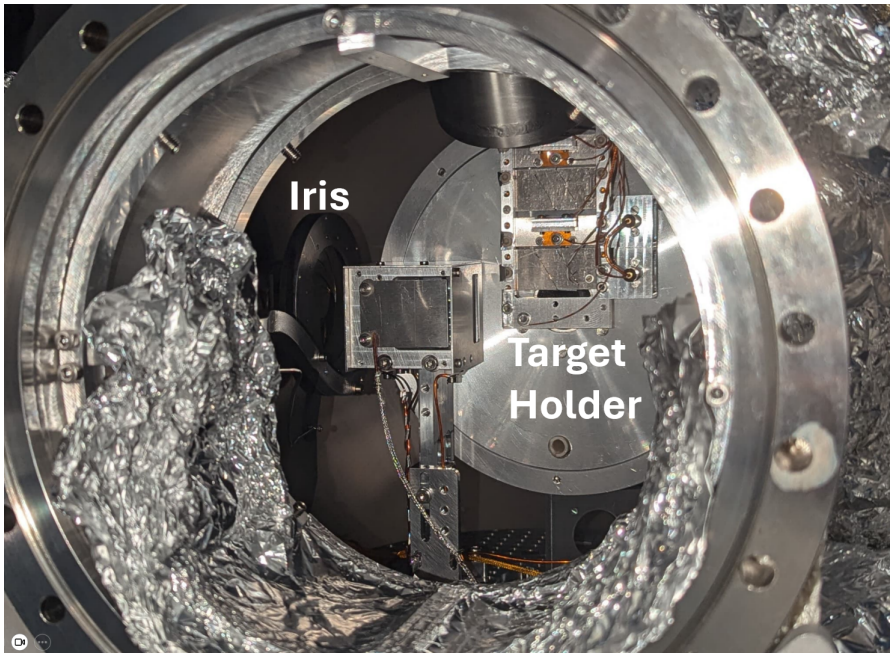

Figure 2.9: Photograph of the beam line components inside the reaction chamber.

2.5.2 e^+ Beam Line

Figure 2.10 [63] is an illustration of the LINAC used in the GBAR experiment to generate a pulsed e^+ beam. On the left side of the figure, RF linear accelerator ('Linac'), a tungsten (W) target ('Linac target'), and coils for transporting the generated e^+s ('Coils') are shown.

The LINAC produces a pulsed beam of electron with a kinetic energy of 9 MeV and a repetition frequency ranging from 5 Hz up to 300 Hz. The electron beam is irradiated onto the W target to produce e^+s with a kinetic energy up to 7 MeV through the pair creation process by γ-rays induced inside the W target. Since the energy of the produced e^+s is too high, the e^+s are immediately passed through a moderator made of 20 μm thin W wires. The wires were annealed at very high temperature to increase the effective e^+ diffusion length and to clean the surface. Subsequently, the e^+s are extracted at 50 eV from the moderator surface into vacuum. As such, the GBAR LINAC type e^+ source is capable of generating a pulsed e^+ beam with a relatively high production rate of about 5×10^7 per second, even with a relatively low-energy and low-power electron beam [63].

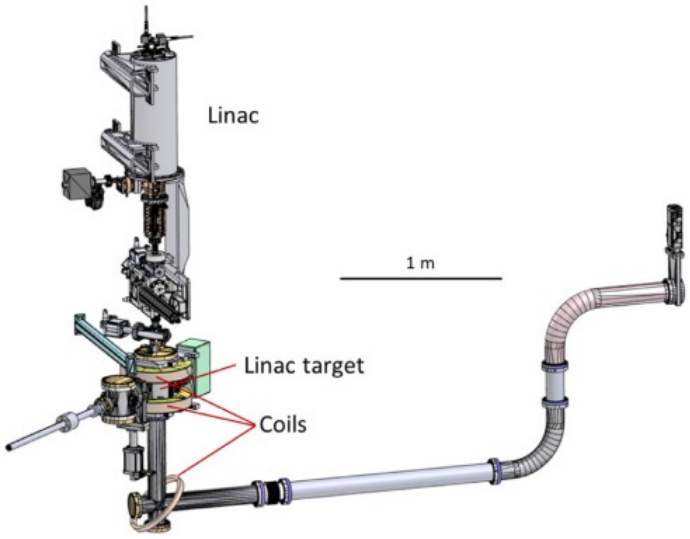

Figure 2.10: The GBAR LINAC type e^+ source, adapted from Reference [63].

The generated e^+s are then trapped, cooled, bunched, and accumulated by using the BGT and HFT. Figure 2.11 shows a scheme of the BGT. The BGT consists of three stages under a solenoid magnetic field of 45 mT. The BGT used to have the Surko-Greaves type structure composed of three different stages as it was originally designed [64]. However, in 2023, the BGT was upgraded to accommodate a remoderator made of a silicon carbide (SiC) single-crystal wafer at the end of the first stage of the BGT, and the electrode stacks in the first and second stage were modified.

The SiC remoderator basically has replaced the nitrogen (N_2) gas in the original design, for capturing the incoming e^+s. The e^+s extracted from the LINAC has a kinetic energy from 50 eV to 150 eV, and get implanted onto the SiC wafer. The e^+s are then re-emitted with a kinetic energy around 3 eV, and trapped in the potential well of the first and second stage more efficiently than in the original design. The trapped e^+s are cooled through inelastic collisions with carbon dioxide (CO_2) gas, and radially compressed by the RW wall technique [70, 71]. The gas cooling and radial compression are performed for 125 ms, then the e^+s are transported to the third stage. In the third stage, further cooling

and compression are performed at a lower CO_2 pressure, then the e^+s are transported to the HFT as it was done in the original design [64].

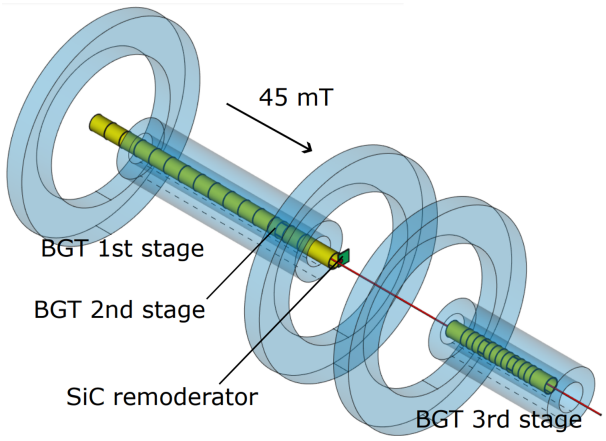

Figure 2.11: Scheme of the BGT in the GBAR experiment.

Figure 2.12 shows a scheme of the HFT. The HFT forms a uniform magnetic field with a central field strength of 5 T by using a superconducting solenoid cooled by a GM cryocooler. The e^+s transported every 125 ms from the third stage of the BGT are accumulated until the extraction of the $\bar{p}$ from the $\bar{p}$ trap.

In 2021, accumulations of approximately 1.36×10^8 e^+s in 100 seconds and $1.4(2) \times 10^9$ e^+s in 1100 seconds were achieved [64]. The ultimate goal for the gravitational free-fall measurement is to accumulate about 10^{10} e^+ in 100 seconds.

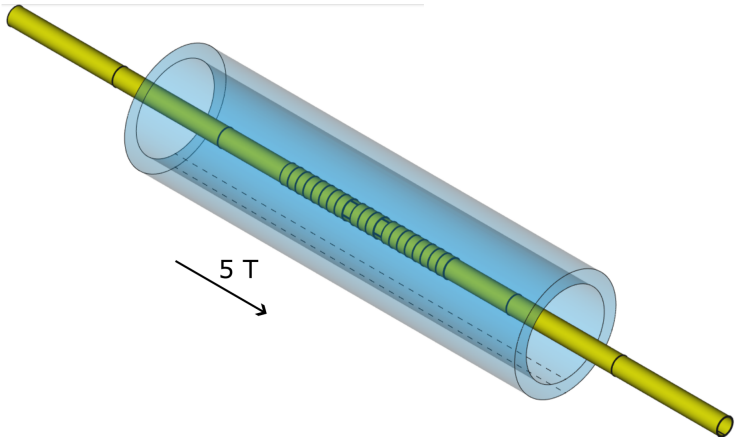

Figure 2.12: Scheme of the HFT in the GBAR experiment.

The trapped e^+s are then non-adiabatically accelerated towards the field-free region around the reaction target [68] and implanted onto the target with a kinetic energy of around 4.5 keV, which is an optimum energy for the produced Ps cloud to efficiently overlap with the trap-extracted $\bar{p}$ beam.

2.6 $\bar{\mathrm{H}}$(2S) Production Rate

To estimate the number of $\bar{\mathrm{H}}$(2S) available for the Lamb shift spectroscopy, assuming the charge-exchange reaction of Equation (2.1) between the $\bar{p}$s with a kinetic energy of $E_{\bar{p}}$ and the ground state Ps($1s$), the $\bar{\mathrm{H}}$ production rate $N^{\bar{\mathrm{H}}}_{\mathrm{Ps}(1s)}(E_{\bar{p}})$ per pulse can be approximated as the following equation:

$$N^{\bar{\mathrm{H}}}_{\mathrm{Ps}(1s)}(E_{\bar{p}}) = \int_{-\infty}^{\infty}\int_{V_0} \sigma_{\mathrm{Ps}(1s)}(E_{\bar{p}}) \cdot n_{\bar{p}}(t,\boldsymbol{r}) \cdot n_{\mathrm{Ps(1S)}}(t,\boldsymbol{r})\boldsymbol{dr} \cdot v_{\bar{p}}(E_{\bar{p}})dt \tag{2.3}$$

where $\sigma_{\mathrm{Ps}(1s)}(E_{\bar{p}})$, $n_{\bar{p}}(t,\boldsymbol{r})$, and $n_{\mathrm{Ps(1S)}}(t,\boldsymbol{r})$ denote the cross-section of the reaction as a function of $E_{\bar{p}}$ (shown in Figure 2.2), density of $\bar{p}$ beam, and density of Ps(1S) cloud taking the decay rate into account. The densities are functions of time t and coordinate $\boldsymbol{r}$ in the laboratory frame. $v_{\bar{p}}(E_{\bar{p}})$ represents speed of the $\bar{p}$ at the energy $E_{\bar{p}}$. The time t is integrated from negative to positive infinite, and the coordinate $\boldsymbol{r}$ is integrated over the volume of the reaction target V_0. Supposing uniform and static densities for the $\bar{p}$ beam and Ps(1S) cloud, this equation can further be approximated to the following form:

$$N^{\bar{\mathrm{H}}}_{\mathrm{Ps}(1s)}(E_{\bar{p}}) = \sigma_{\mathrm{Ps}(1s)}(E_{\bar{p}}) \cdot N_{\bar{p}} \cdot n_{\mathrm{Ps(1S)}} \cdot L \tag{2.4}$$

where $N_{\bar{p}}$ and L denote the total number of $\bar{p}$ contributing to the reaction and the length of the reaction target along the trajectory of the $\bar{p}$ beam, respectively.

Quoting design values discussed in the GBAR proposal [36], which are $N_{\bar{p}} = 10^7$, $n_{\mathrm{Ps(1S)}} = 10^{12}$ cm^{-3}, and $L = 1$ cm, Equation (2.4) gives $N^{\bar{\mathrm{H}}}_{\mathrm{Ps}(1s)}(6\,\mathrm{keV}) = 10^4$ assuming the cross-section of 10×10^{-16} cm^2, which does not contradict to the estimated value of $(11 \pm 5) \times 10^{-16}$ cm^2 as a lower limit at 6 keV [56]. For the $\bar{\mathrm{H}}$(2S) production rate, one could expect $N^{\bar{\mathrm{H}}(2\mathrm{S})}_{\mathrm{Ps}(1s)}(6\,\mathrm{keV}) = 1500$ by simply taking the $2S$ state ratio of about 15% [45].

Chapter 3

Lamb Shift Spectroscopy

3.1 Spectroscopy Setup

A scheme of our spectroscopy setup is illustrated in Figure 3.1. Trajectories of $\bar{p}$, e^+, and $\bar{\mathrm{H}}$ are represented by the orange, blue, and green arrows, respectively. The Ps production target is depicted as a cloud. The $2S$ state $\bar{\mathrm{H}}$ atom, having a lifetime of 0.12 seconds, first passes through the MW spectrometer, which irradiates a MW electric field (MW E-field) in the range of 0.6 GHz to 1.5 GHz. If the Lamb shift transition is induced, the $2S$ state is de-excited to the $2P$ state. The $2P$ state $\bar{\mathrm{H}}$ atom, having a lifetime of only 1.6 ns, spontaneously decays to the ground state through the Lyman-α transition.

After the spectrometer, the number of remaining $\bar{\mathrm{H}}(2S)$ atoms is counted by a Lyman-α photon detector. The detector is equipped with two ring-shaped electrodes to form a direct current electric field (DC E-field), to de-excite the $\bar{\mathrm{H}}(2S)$ atoms to the ground state through the Lyman-α transition via Stark mixing. The Lyman-α photons emitted here are detected by CsI coated microchannel plates (MCPs) [72].

By repeating this procedure with different MW frequencies for each pulse of $\bar{\mathrm{H}}$ beam, the Lamb shift resonance spectrum will be obtained as a decrease in the Lyman-α photon counts.

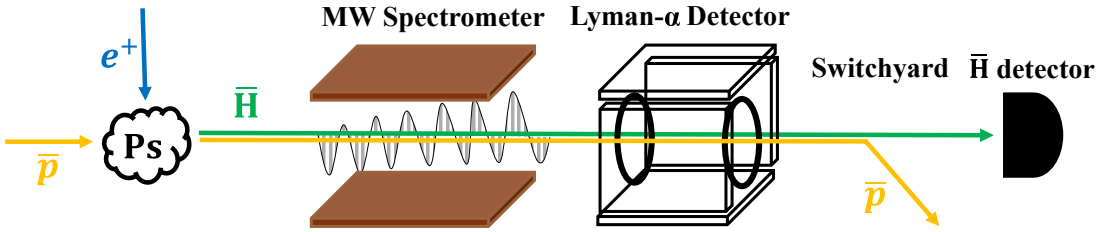

Figure 3.1: $2S_{1/2} - 2P_{1/2}$ Lamb shift spectroscopy setup in the GBAR experiment.

After the spectroscopy region, an electrostatic switchyard and a $\bar{\mathrm{H}}$ detector are located. The switchyard deflects $\bar{p}$ beam and only the neutral $\bar{\mathrm{H}}$ atoms arrive at the $\bar{\mathrm{H}}$ detector downstream.

Right behind the switchyard, on the straight trajectory of the neutral $\bar{\mathrm{H}}$ atoms, a $\bar{\mathrm{H}}$ detector is situated. The $\bar{\mathrm{H}}$ detection here will be used for taking a coincidence with the signal at the Lyman-α detector.

3.2 Spectrum Broadening

Under CPT symmetry, the $2S_{1/2}$ and $2P_{1/2}$ states of an $\bar{\mathrm{H}}$ atom should have the same hyperfine structure levels $F = 0$ and 1 as those of a H atom, where F denotes the total angular momentum. Concerning H atoms, the transition frequency between the $2S_{1/2}$ $F = 0$ and $F = 1$ level was measured to be 177.556 834 3(67) MHz [73], and the transition frequency between the $2P_{1/2}$ $F = 0$ and $F = 1$ level was reported to be 59.22(14) MHz [74] experimentally and 59.1695(6) MHz theoretically [75].

As illustrated in Figure 3.2(a), the Lamb shift transition induced by a linearly polarized MW E-field is composed of three transitions originating from the variation of the total magnetic quantum number denoted by m_F. The transition frequencies, without being affected by any external fields, are about 910 MHz, 1088 MHz, and 1147 MHz, respectively.

The energy splits corresponding to each of these transitions ΔE_{910} (910 MHz transition), ΔE_{1088} (1088 MHz transition), and ΔE_{1147} (1147 MHz transition) can relate with the energy split of Lamb shift ΔE_{Lamb} using the following equations [76]:

$$\Delta E_{910} = \Delta E_{\mathrm{Lamb}} - \frac{3}{4}\Delta E_{2S}^{\mathrm{HFS}} - \frac{1}{4}\Delta E_{2P}^{\mathrm{HFS}} \tag{3.1}$$

$$\Delta E_{1088} = \Delta E_{\mathrm{Lamb}} + \frac{1}{4}\Delta E_{2S}^{\mathrm{HFS}} - \frac{1}{4}\Delta E_{2P}^{\mathrm{HFS}} \tag{3.2}$$

$$\Delta E_{1147} = \Delta E_{\mathrm{Lamb}} + \frac{1}{4}\Delta E_{2S}^{\mathrm{HFS}} + \frac{3}{4}\Delta E_{2P}^{\mathrm{HFS}} \tag{3.3}$$

where $\Delta E_{2S}^{\mathrm{HFS}}$ and $\Delta E_{2P}^{\mathrm{HFS}}$ denote the energy split in the $2S$ state hyperfine structure and $2P$ state hyperfine structure, respectively.

Each resonance line shape of these corresponding transitions has a natural width due to the spontaneous decay rate of $2P$ state, which is known to be $99.7Z^4$ MHz for hydrogen-like atoms [77], where Z represents the atomic number. As a result, each line shape mutually overlaps and the experimentally observable line shape of $2S_{1/2} - 2P_{1/2}$ Lamb shift transition appears as the black solid curve in Figure 3.2(b), where the contributions of the three transitions are represented by orange (910 MHz transition), blue (1088 MHz transition), and green (1147 MHz transition) filled area.

Concerning the 1088 MHz transition and 1147 MHz transition, the resonance frequencies are too close for each peak in the line shape to be distinguishable. Consequently, a merged single peak around 1100 MHz and the peak of the 910 MHz transition are observed in the spectrum. This broadening in the spectrum is one of the difficulties to precisely determine the Lamb shift resonance frequency.

3.3 high-precision Setup

To circumvent the spectrum broadening, spectroscopy setups consisting of multiple MW apparatuses have been adopted in the history of the H Lamb shift spectroscopy [6,7,9]. In our case, due to the limited length of beam line, the setup consisting of two consecutive MW apparatuses is adopted as illustrated in Figure 3.3(a).

The first apparatus *Hyperfine Selector* (HFS) filters out the $2S_{1/2}$ $F = 1$ states beforehand by irradiating a MW field at frequency of 1.1 GHz to simplify the resonance. The second apparatus *Microwave Scanner* (MWS) sweeps the MW frequency in the range of 0.6 GHz to 1.5 GHz to obtain a spectrum with a single peak dominantly made by the pre-selected $2S_{1/2}$ $F = 0$ state. Consequently, the line shape of the transition appears as the black curve in Figure 3.3(b), where the contributions of the 1088 MHz transition and 1147 MHz transition are suppressed.

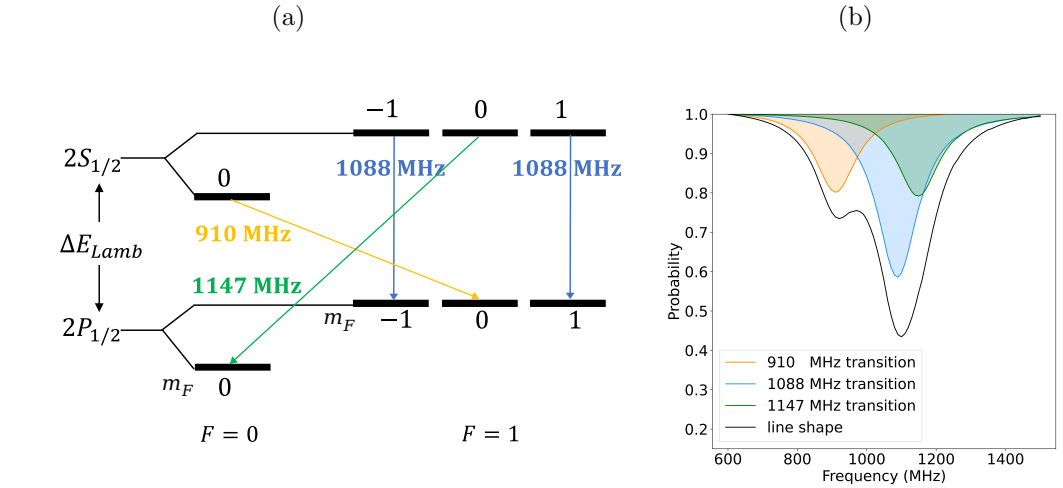

Figure 3.2: (a) $2S_{1/2} - 2P_{1/2}$ Lamb shift transition and (b) observable line shape with the decomposed contributions of the three transitions.

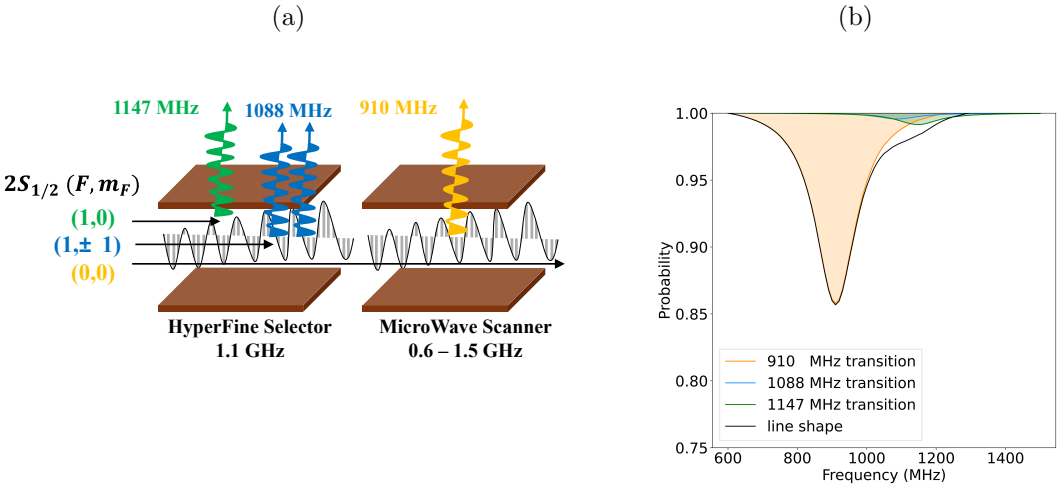

Figure 3.3: (a) Spectroscopy setup consisting of two consecutive MW apparatuses, and (b) observable line shape with the decomposed contributions, when the HFS is utilized.

3.4 Structure of MW apparatus

For both the MWS and HFS, the same structure of MW apparatus and the associated MW circuit components are deployed, which are schematically illustrated in Figure 3.4.

The MW signal is first generated by a high-frequency signal generator, typically at −3 dBm. Then the signal is amplified by a 43 dB amplifier to 10 W (40 dBm), and split by a 180 ° phase inverting divider. Inside the MW apparatus, the phase inverted signals are fed to the upper and the lower electrode via SMA connectors fixed on the rectangular box with their pin stuck into the electrodes. In this manner, a constructively oscillating MW E-field is formed between the electrodes. Then, the signals are transmitted through to the SMA connectors on the other side. After the MW apparatuses, the signals are combined, attenuated, and the power is measured at the end, in order to estimate the frequency-dependence of the MW field amplitude during the spectroscopy. For all the circuit components, including the coaxial cables, 50 Ω impedance-matched products are

adopted.

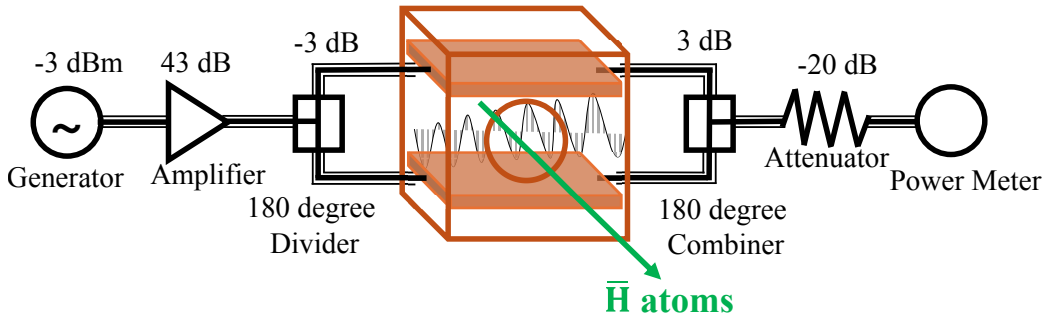

Figure 3.4: Structure of MW apparatus and the associated MW circuit components.

3.5 Lyman-α Detector

After the MW spectrometer, the Lyman-α detector is situated. The detector has adopted MCPs for the following reason.

Our $\bar{\mathrm{H}}(2S)$ atoms are produced by charge-exchange reaction between the pulsed $\bar{p}$ beam with a specific kinetic energy around a few keV and the Ps cloud. This means that the produced $\bar{\mathrm{H}}(2S)$ atoms should have a characteristic arrival time to the Lyman-α detector derived from the kinetic energy of $\bar{p}$ beam. In contrast, background particles lack this characteristic time structure in principle. In the GBAR experiment, $\bar{\mathrm{H}}$(2S) atoms on the order of 1000 are ultimately expected to be produced per AD cycle within the characteristic time window on the order of 100 ns. Assuming the total detection efficiency of the detector to be on the order of 10% (evaluated in Section 5.5), 100 Lyman-α photon signals are expected to be seen within the 100 ns time window. If one approximates that these signals are randomly distributed within the time window, a timing resolution on the order of 1 ns is roughly required for the detector, which is achievable by using MCPs [78]. See Reference [72, 79] for detailed design of Lyman-α detector.

3.5.1 Working Principle

A 3D drawing of the Lyman-α Detector is shown in Figure 3.5. A DC E-field with amplitude of a few hundreds kV/cm is formed by a pair of ring-shaped high voltage electrodes to de-excite the remaining $\bar{\mathrm{H}}(2S)$ to the ground state by inducing the Stark mixing with the short-lived $2P$ state.

Subsequently to the decay, a Lyman-α photon is emitted, which can be detected by a quartet of MCP, each having a Chevron configuration and an open area ratio of 0.45 [79]. The MCP itself is capable of detecting photons in ultraviolet (UV) region in principle. For channel multipliers in general, the detection efficiency was reported to be from 1 to 5% for UV photons with a wavelength from 110 nm to 150 nm [78]. Concerning a Z stack MCP configuration, the detection efficiency was reported to be around 20% for UV photons of 110 nm wavelength [80].

In order to enhance the detection efficiency for the Lyman-α photons with a wavelength of 122 nm, a layer of CsI is coated on the front surface of each of our MCPs, effectively converting the Lyman-α photons to photoelectrons. The quantum efficiency of CsI for the Lyman-α photons is known to be around 50% [81, 82]. Taking the CsI quantum efficiency into account, the efficiency of our MCPs was evaluated to be 22(2)% [72, 79]. The total

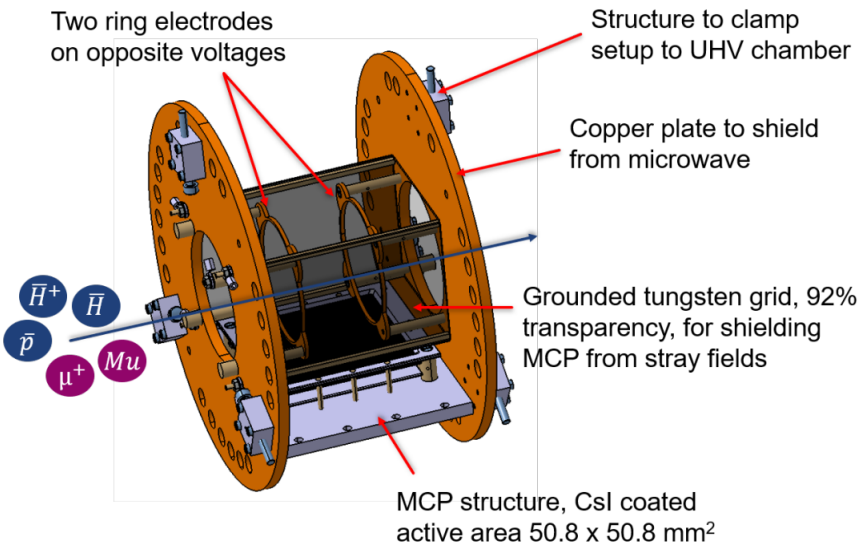

Figure 3.5: 3D drawing of the Lyman-α Detector, adapted from Reference [79]

detection efficiency, taking into account the geometrical efficiency, is evaluated to be about 10%, as discussed in Section 5.5.

3.5.2 MCP Bias Scheme

The MCPs can be operated in two different bias schemes. One scheme is to apply negative high voltages on the front side (the beam side) of the MCPs, with the back side (read out side) grounded, as illustrated in Figure 3.6(a) The other scheme is to apply positive high voltages on the back side of the MCPs, with the front side grounded or biased slightly positively or negatively, as illustrated in Figure 3.6(b).

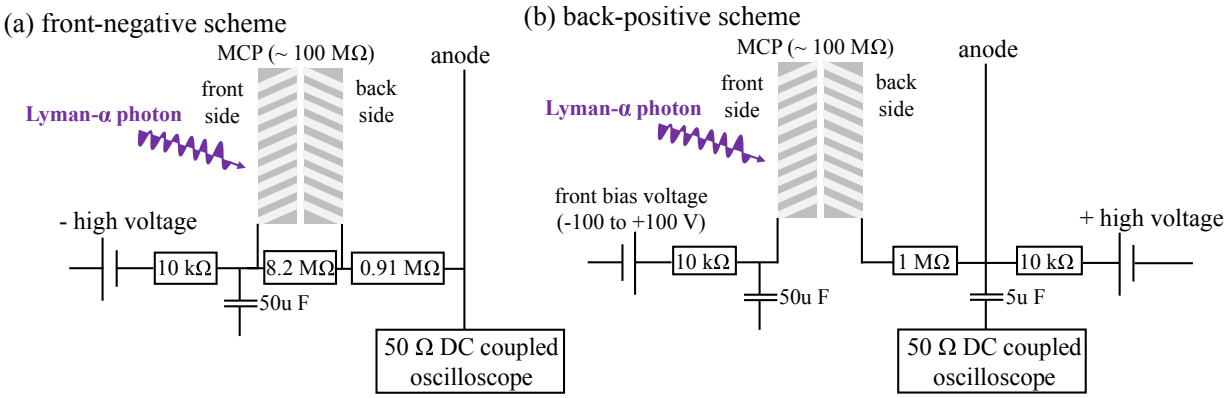

Figure 3.6: Two different schemes of biasing MCPs, (a) applying negative high voltages on the front side of the MCPs, and (b) applying positive high voltages on the back side of the MCPs.

An advantage of the front-negative scheme is that any background noise due to negatively charged particles can be repelled away from the MCP. However, this could reduce the signal count rate by repelling the photoelectron produced by the Lyman-α photon on the CsI coating. In this scheme, a voltage divider is adopted to reduce the risk of damaging the MCPs.

On the other hand, an advantage of the back-positive scheme is, especially when the front side is biased positively, that the photoelectrons can be effectively collected, possibly improving the detection efficiency for the Lyman-α photons. However, this could also increase the background count rate by attracting any negatively charged particles around the MCPs. In this scheme, this trade-off could be investigated by sweeping the bias voltage on the front side.

3.5.3 Read Out

The electric pulse signals from each MCP are recorded using a 4-channel oscilloscope (LeCroy Wavesurfer 3054Z). Each channel is DC-coupled to the anode in the front-negative scheme and AC-coupled to the anode in the back-positive scheme. The oscilloscope is triggered at the moment of extracting the $\bar{p}$ beam. Waveforms at each channel are typically recorded with the following parameters:

- Sampling rate: 1 GHz
- Recording duration: 10 µs (10,000 samples per trigger)
- Resolution: 20 mV per division
- Digitization: 8 bit
- Bandwidth: 200 MHz to 500 MHz

After recording, waveforms from all the four channels are output to a binary trace file for offline analysis.

3.6 Precedent Measurement

Deploying the MW apparatuses discussed in Section 3.4, and Lyman-α detector of the similar structure discussed in Section 3.5, a high-precision MW spectroscopic measurement has been running in Mu-MASS collaboration [46] to measure the Lamb shift transition in Mu atoms. In 2022, they achieved the Lamb shift spectroscopy at a precision of a couple of MHz [83], as well as a derivation of $2S_{1/2}(F = 1)$ hyperfine structure and an observation of the $3S$ state [84]. In these measurement, MW apparatuses with the borehole diameter and electrode spacing of 20 mm were adopted, as shown in Figure 3.7.

Furthermore, similar MW apparatuses and Lyman-α detector were installed in the GBAR beam line as well [79]. In 2021, the setup was commissioned by performing the Lamb shift measurement on H atoms. For the production of an atomic beam of H, a thin carbon foil and a DC beam of proton generated by a proton gun (Polygon Physics TES-35) were employed. Figure 3.8 shows the Lamb shift spectrum obtained at the time for a several hours of data-taking. The Lamb shift resonance frequency here was determined as 1050.5 ± 13.5 (MHz).

3.7 Switchyard

Behind the Lyman-α detector, an electrostatic switchyard is situated which consists of a pair of long outer electrodes and a pair of short inner electrodes as shown in Figure 3.9. See Reference [85] for details of the design, and [56] for recent optimization of voltages applied on the electrodes.

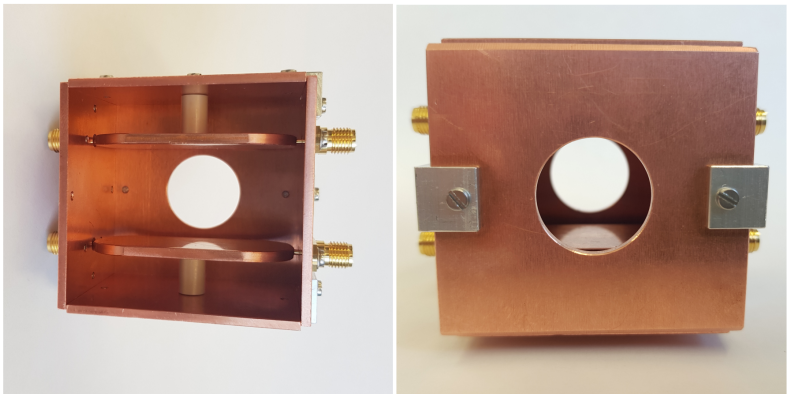

Figure 3.7: Photograph of the MW apparatus with borehole diameter and electrode spacing of 20 mm, showing the view inside on the left and outside on the right, adapted from Reference [79].

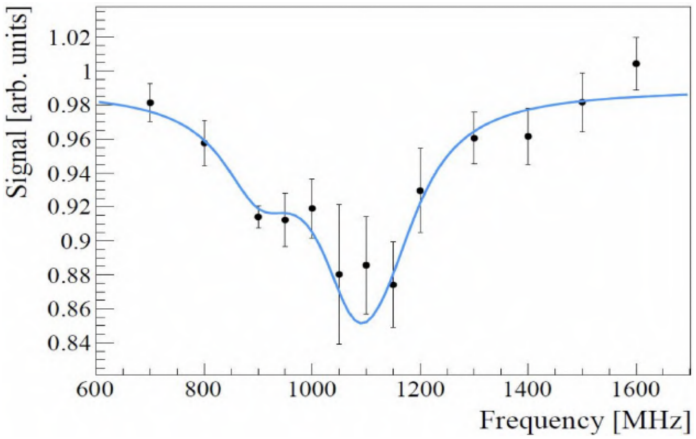

Figure 3.8: Lamb shift spectrum of the H atoms produced at the GBAR beam line, adapted from Reference [60].

On each electrode pair shown in Figure 3.9, an anti-symmetric set of high voltages are applied to separate the neutral $\bar{H}$ beam, negatively charged $\bar{p}$ beam, and positively charged $\bar{H}^+$ beam, respectively.

3.8 $\bar{H}$ Detector

Behind the switchyard, an $\bar{H}$ detector is situated. The detector comprises a MCP, phosphor screen, and CCD camera. The scheme of $\bar{H}$ detection in the GBAR experiment involves single particle detection based on fast electric pulse signal obtained from the MCP and spatially distinguished pixel clusters obtained from the phosphor screen and CCD camera positioned right behind the MCP, as illustrated in Figure 3.10(a). See Reference [86] for details of the design, and Reference [44] for details of the operation as of 2022.

A MCP from Photonis (Advanced Performance Detector Assemblies APD 2 PS 40/12/10/8 I 60:1 EDR P46) shown in Figure 3.10(b) was equipped with our $\bar{H}$ detector. Main features of the MCP are shown below:

- MCP Count: 2×0.5 mm (Chevron configuration)
- Quality Diameter: 40 mm

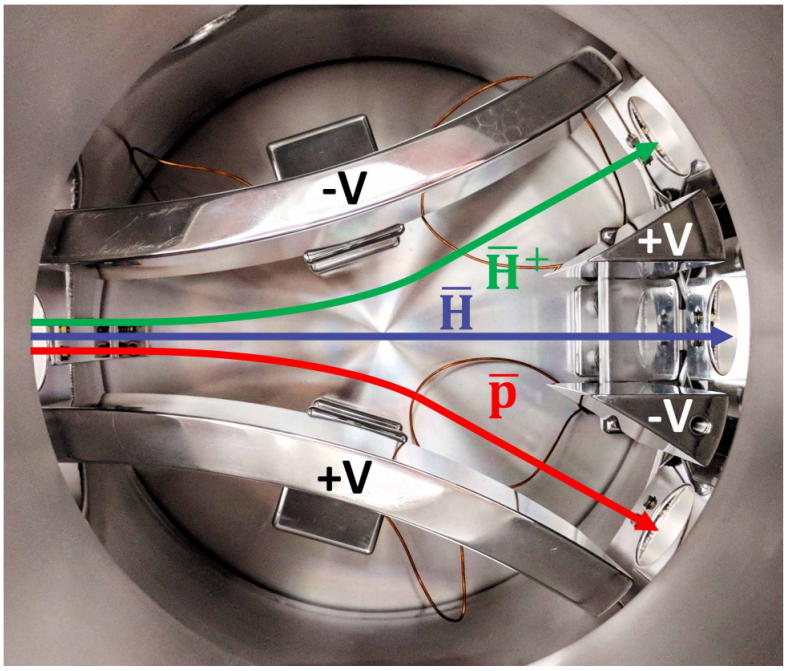

Figure 3.9: Photograph of the switchyard electrodes adapted from Reference [56].

- Pitch: 12 μm
- Pore Size: 10 μm
- Bias Angle: 8 °
- Option: Extended Dynamic Range
- Gain: 1.76×10^7 at 2200 V [44]
- Open Area Ratio: 55%

A positive bias voltage ranging from 2200 V to 2300 V has been applied on the back side of the MCP in the single particle detection mode, and around 1450 V has been applied to diagnose the $\bar{p}$ beam.

To convert electrons amplified by the MCP to visible light, the MCP assembly includes the P46 phosphor screen. The phosphorescent light is detected by the CCD camera (model pixelfly from PCO, with Sony ICX285AL image sensor), having a resolution of 1392 $\times$ 1040 pixels. For the $\bar{H}$ detection, the CCD camera is typically exposed for 1 μs, triggered for the arrival time of $\bar{H}$ atoms.

(a) (b)

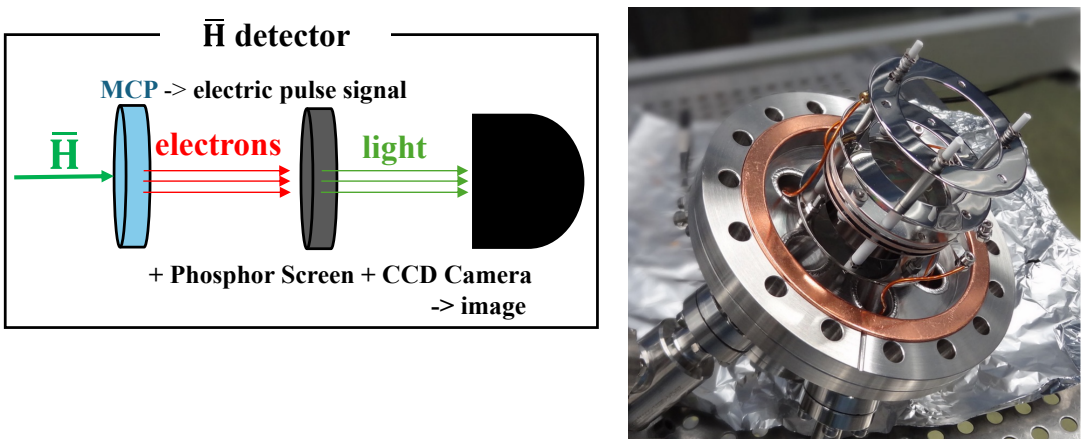

Figure 3.10: (a) Scheme of the $\bar{H}$ Detector, and (b) photograph of the MCP of adapted from Reference [86]

3.9 Thesis Outline

Based on the motivations and methodology of the $\bar{\mathrm{H}}$ Lamb shift spectroscopy discussed so far, this thesis describes several distinct works.

Figure 3.11 shows a road map towards the spectroscopy experiment, which categorizes the works described in this thesis into the following four subjects:

- MW spectrometer
- Simulation
- Experimental consideration
- $\bar{\mathrm{H}}$ production

As shown in the middle of the road map, the MW spectrometer needed to be designed, so that it adapts to the $\bar{\mathrm{H}}$ beam produced in the GBAR experiment. Concerning this subject, Chapter 4 reports the development of the MW spectrometer. The topics range from designing of the spectrometer using MW simulations, production, to power characterization after the installation in the GBAR $\bar{\mathrm{H}}$ beam line.

As shown on the right in the road map, simulations of the spectroscopy were necessary to confirm the feasibility of the measurement given the MW spectrometer produced in this research and the production rate of $\bar{\mathrm{H}}$ atoms achieved in the GBAR experiment. Concerning this subject, Chapter 5 reports the development of a numerical calculation program to simulate the spectroscopy experiment. The topics range from evaluations of the performance of the MW spectrometer and the Lyman-α detector's efficiency, to predictions of the spectroscopy precisions expected for certain data-taking periods.

As shown at the bottom in the road map, in the actual experiment, background signals are expected to be observed at the Lyman-α detector, and a quantitative survey of the background signals was lacking. Concerning this subject, Chapter 6 reports commissioning of the Lyman-α detector to measure the background signals, using the $\bar{p}$ beam extracted from the $\bar{p}$ trap for the first time. This chapter first describes characterizations of the Lyman-α detector's response using a ultraviolet (UV) photon source, and some attempts to detect the Lyman-α photons using an atomic beam of H. Then, the background measurements using the $\bar{p}$ beam are discussed.

As shown on the top in the road map, sufficient amount of $\bar{\mathrm{H}}$ atoms are essential to carry out the spectroscopy experiment. During this research, the GBAR collaboration conducted the $\bar{\mathrm{H}}$ production experiments for the first time, which are described in the Chapter 7. In this chapter, the first experiment conducted in 2022 is reviewed, which demonstrated the production of the $\bar{\mathrm{H}}$ atoms. Then, a preliminary analysis from the experiment conducted in 2024 is reported. For these experiments, this research mainly contributed to the data-taking during the beam time and the data analysis.

Lastly, the summary and prospects of the thesis are described in Chapter 8.

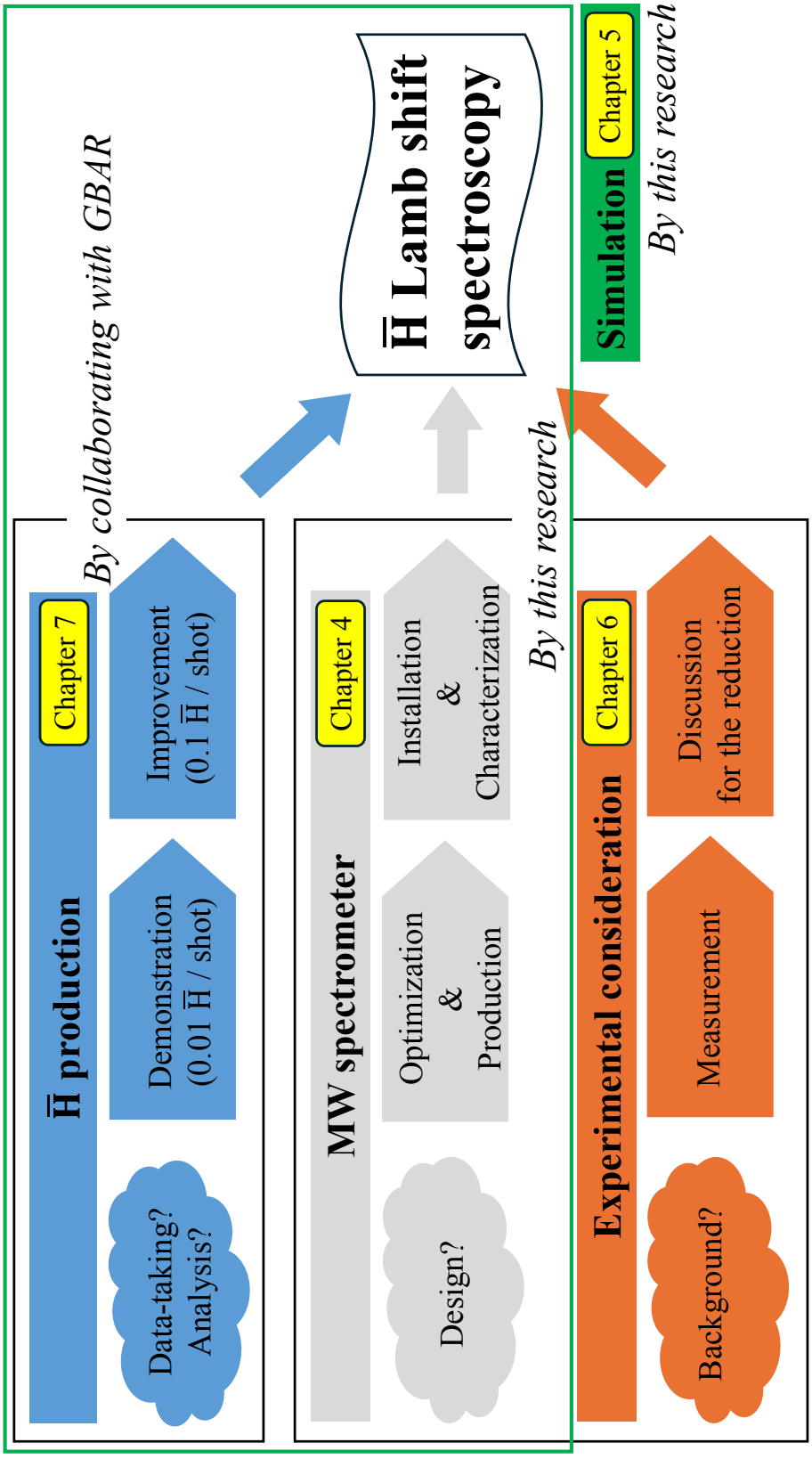

Figure 3.11: Road map towards the $\bar{H}$ Lamb shift spectroscopy experiment.

Chapter 4

Microwave Spectrometer

We developed the MW spectrometer which has the borehole diameter and electrode spacing of 30 mm, to adapt for the $\bar{\mathrm{H}}$ beam with a relatively large beam profile. In this chapter, optimizations of the spectrometer by using MW simulations and its production are described, as well as the power characterization after the installation to the GBAR $\bar{\mathrm{H}}$ beam line.

4.1 Upgrade to 30 mm bore model

The $\bar{\mathrm{H}}$ beam produced in the GBAR experiment is expected to have a larger beam diameter of a couple of cm than that of the Mu beam in the Mu Lamb shift spectroscopy at PSI.

During the $\bar{\mathrm{H}}$ production experiment in 2022, a few shot of $\bar{p}$ beam were transported through the spectroscopy setup to measure the background signals for the Lyman-α detector. At the time, prototypes of the MW apparatuses with the borehole diameter and electrode spacing of 20 mm had been installed, which had almost identical structures to the apparatuses used in the Mu Lamb shift spectroscopy described in Section 3.6. In the background measurement at the time, considerable amount of signals were observed due to annihilation of $\bar{p}$s at the location of the MW spectrometer, which indicated that the $\bar{p}$ beam interfered with the MW apparatuses. This could also mean that some of the produced $\bar{\mathrm{H}}$ atoms would be lost at the MW spectrometer as well, since the $\bar{\mathrm{H}}$ beam should have a similar profile to the $\bar{p}$ beam.

Therefore, new MW apparatuses with the borehole diameter and electrode spacing of 30 mm were considered for both the HFS and MWS, to avoid the interference with the $\bar{\mathrm{H}}$ beam and $\bar{p}$ beam. The design of the new MW apparatuses were reported in Reference [87]. In the following, more detailed description of optimizations of geometric parameters of the 30 mm bore model MW apparatuses are given.

4.2 Design of MWS

Concerning the MWS, which is scanned over the frequency range from 0.6 GHz to 1.5 GHz, it is preferable that the MW E-field amplitude should have the minimal frequency-dependence. Also, the amplitude of 10 V/cm will be desired over the frequency range in order to draw clear Lamb shift spectrum, according to a simulation performed by the numerical calculation program described in Chapter 5.

Therefore, we sought for the structure that enables the apparatus to function as a 50 Ω impedance-matched transmission line, suppressing the frequency-dependence of reflection

of the input MW power and keeping the E-field amplitude around 10 V/cm over the frequency range.

4.2.1 Precedent Design

Figure 4.1(a) shows the 2D drawing of the 20 mm MW apparatus which were previously installed in the GBAR beam line [79]. The apparatus consists of a pair of planar plate electrode as the inner conductor, and a rectangular box as the outer conductor, which composes a MW transmission line as a whole. Both the electrode and box are made from copper plates. As shown in Figrue 4.1(b), L-shaped aluminum angle is used to form the box. The apparatus has two input ports, one for each upper and lower electrode, and two output ports, likewise one for each upper and lower electrode. For each port, the MW power is fed through a SMA connector fixed on the rectangular box with its pin stuck into the inner electrode. The apparatus has symmetry with respect to all the xy, yz, and zx plate. A copper sheet was stuffed between the apparatus and the vacuum chamber wall to center the apparatus around the beam axis.

(a) (b)

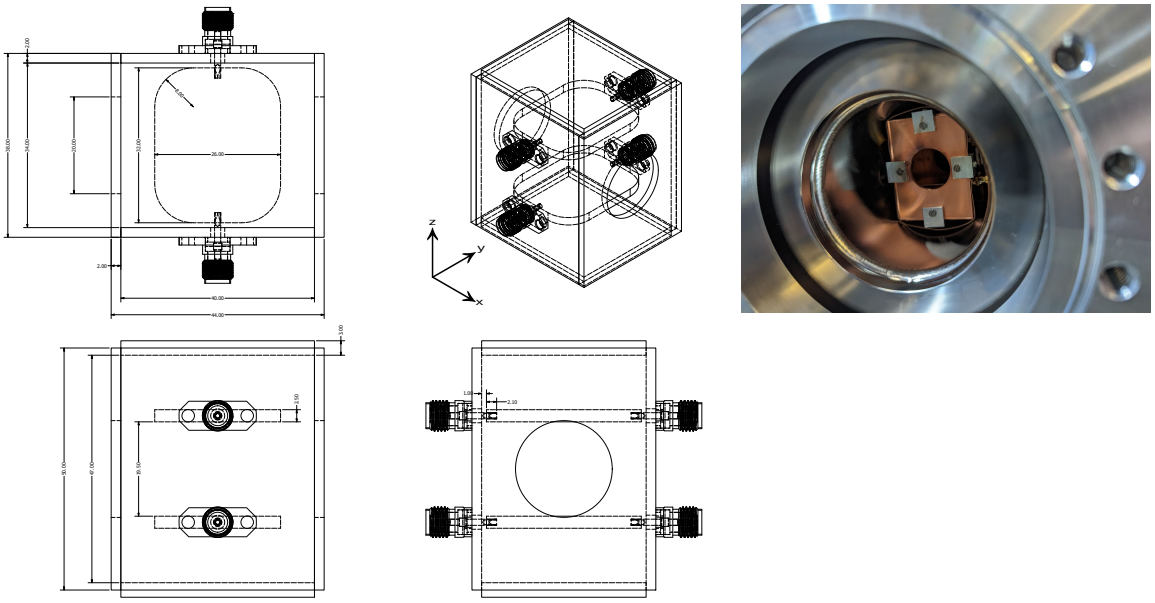

Figure 4.1: (a) 2D drawing and (b) photograph of the 20 mm MW apparatus previously installed in the GBAR beam line.

This apparatus was employed for both the HFS and MWS to demonstrate the Lamb shift spectroscopy of H atoms produced by a proton gun and a thin carbon foil at the GBAR $\bar{\mathrm{H}}$ beam line [60].

4.2.2 Geometrical Optimization of MWS

For the MW simulations to optimize the geometry, CST Studio Suite (Microwave Studio) [88] was utilized, and the S-parameter S_{11} – the ratio of reflected MW power at one single input port – was calculated for different geometries. In principle, the frequency characteristic of the whole apparatus can be fully evaluated by S_{11} of either the upper or lower input port due to the vertical symmetric structure of the apparatus.

Figure 4.2 illustrates the major geometric parameters of the MW apparatus. The parameters X_b, Y_b and Z_b, represents the internal sizes of the box, along the $\bar{H}$ beam direction (x-axis), the horizontal direction parallel to the Poynting vector of the MW (y-axis), and the vertical direction (z-axis), respectively. The X_e and Y_e denotes the lengths of the electrode in the corresponding directions.

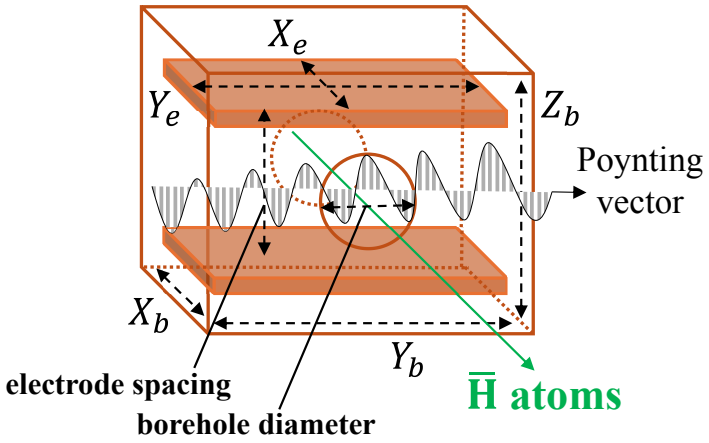

Figure 4.2: Geometric parameters to be optimized using CST Microwave Studio.

In the following simulations, these parameters were swept from *Min.* to *Max.* by *Step* under *Constraints* if any, which are all listed in Table 4.1. Each parameter values adopted for the 20 mm MW apparatus are listed as well in the last column of the table. The electrode spacing and borehole diameter were kept 30 mm throughout the simulations.

Parameter	*Min.*	*Max.*	*Step*	*Constraints*	*Value in the 20 mm MW apparatus*
Y_b	34	114	4.0	-	34
Z_b	40	80	2.0	-	47
X_b	40	120	4.0	-	40
Y_e	32	112	4.0	$Y_b = Y_e + 2$	32
X_e	26	106	4.0	$X_b = X_e + 14$	26

Table 4.1: Sweep condition for each parameters of the MWS represented in 3.4.

Figure 4.3 shows simulated S_{11} of the MWS, for different values of (a) Y_b, and (b) Y_e. One can see in Figure 4.3(a) that, as Y_b increases, the S_{11} is enhanced from high-frequency side, and the dip in the spectrum, which is indeed a sign of resonance property, shifts towards the low-frequency side. More crucially, one can see that the baseline of the spectrum rises up. Thus, the apparatus gradually ceases to function as a transmission line, and instead starts to behave more like a resonant cavity at the resonance frequency around the dip. However, as seen in Figure 4.3(b), when the electrodes are extended simultaneously in the same direction, the S_{11} remains suppressed below -10 dB for the entire frequency range. Consequently, one can say that the frequency characteristic is less influenced than in the case of increasing only Y_b. This suggests that, in general, when designing a transmission line, the apparatus should maintain a constant distribution of conductors and inductors on the cut plane orthogonal to the Poynting vector. This principle seems obvious considering the structure of, for example, coaxial cables or strip lines.

The E-field amplitude was analyzed for some values of Y_e, and the E-field amplitude

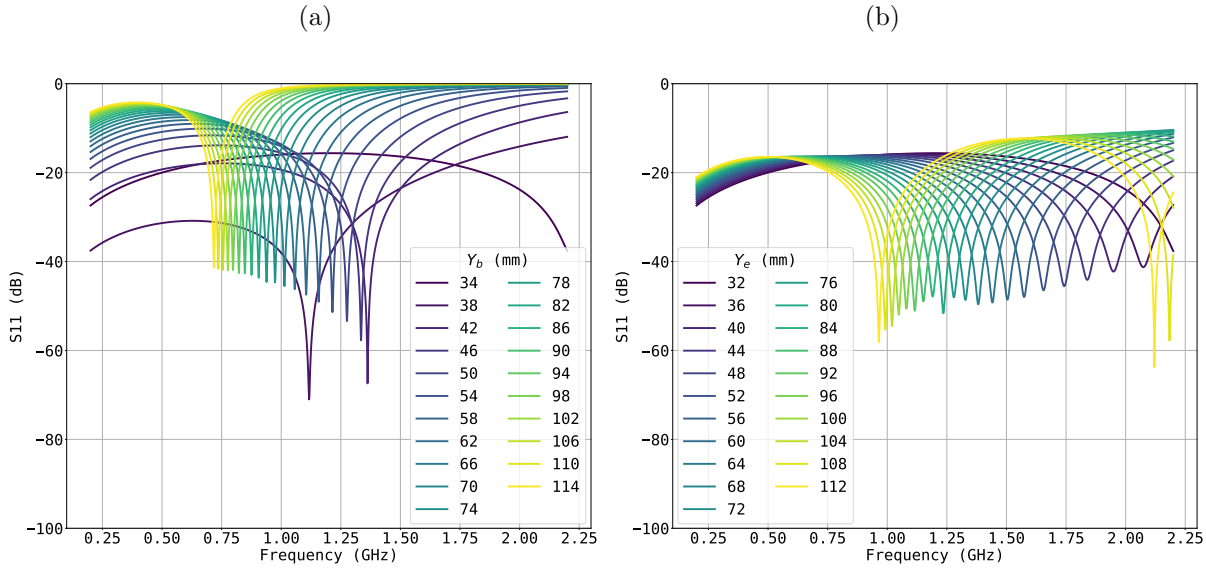

Figure 4.3: Simulated S_{11} of the MWS, for different values of (a) Y_b, and (b) Y_e.

was found to be slightly higher with a larger value of Y_e [89]. Given this tendency and mechanical constraints due to size of the vacuum chamber, Y_b and Y_e were determined to be 100 mm and 98 mm, respectively.

Figure 4.4 shows simulated S_{11} of the MWS, for different values of Z_b. One can see that, as Z_b increases, the S_{11} is suppressed but a resonance property gradually shows up from the high-frequency side, and the dip in the spectrum moves towards the low-frequency side.

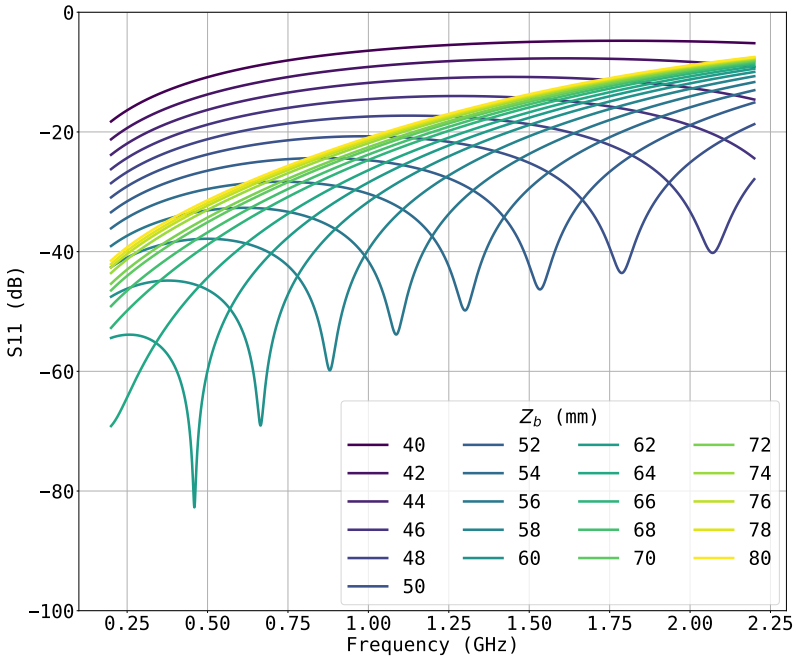

Figure 4.4: Simulated S_{11} of the MWS, for different values of Z_b.

The E-field amplitude was analyzed for some values of Z_b, and frequency-dependence of the amplitude was found to be smaller with a larger value of Z_b [89]. Given this tendency and mechanical constraints due to size of the vacuum chamber, a mechanical realization which enables adjustment of Z_b from 50 mm to 60 mm was conceived as described in Section 4.4.1.

Figure 4.5 shows simulated S_{11} of the MWS for different values of (a) X_b or (b) X_e. One can see in Figure 4.5(a) that, despite the increase of X_b, the S_{11} spectrum maintains more or less the same shape. One can also see that the dip in each spectrum shifts to the low-frequency side by increasing X_b. However, they are anyways signs of minor resonances considering that the baseline of each spectrum is already below around -20 dBm for the entire frequency range. Therefore, one can say that this parameter does not significantly influence the frequency characteristic of the apparatus. On the contrary, as shown in Fgure 4.5(b), increasing the dimension of the electrode simultaneously with the box size in this direction results in a significant power reflection. Therefore, we have adopted the same values as those of the 20 mm MW apparatus for X_b and X_e, which are 40 and 26 respectively as listed in Table 4.1.

To summarize the result of the optimizations, X_b, X_e, Y_b, and Y_e were determined to be 40, 26, 100, and 98 mm, respectively. Concerning Z_b, the produced MWS has a structure which enables adjustment of this parameter in the range from 50 mm to 60 mm, as described in Section 4.4.1.

Regarding the E-field amplitude, a 2D field map of time averaged vertical component of the amplitude is shown in Figure 5.2 in Section 5.2.2, calculated at a total input power of 10 W. One can see that the amplitude at the center of the apparatus is around 10 V/cm

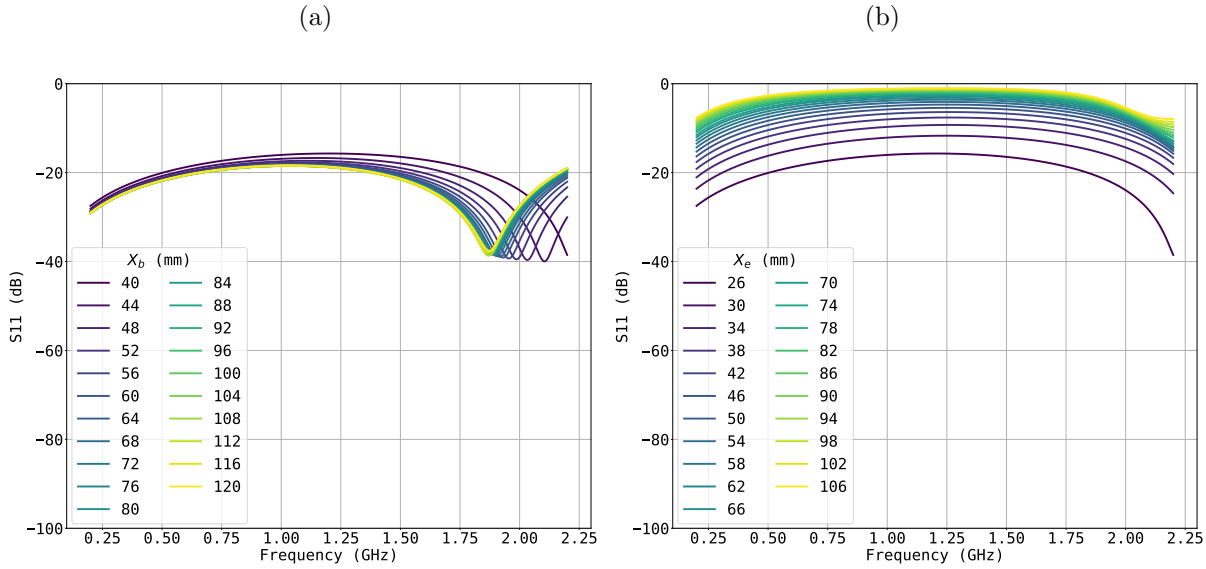

Figure 4.5: Simulated S_{11} of the MWS, for different values of (a) X_b, and (b) X_e.

for different frequencies of (a) 600, (b) 1100, (c) 1500, and (d) 2000 MHz.

4.3 Design of HFS

Concerning the HFS, on the other hand, which is operated at a fixed frequency of 1.1 GHz, it is preferable that the MW E-field amplitude around this frequency should be maximized to efficiently remove the $2S_{1/2}$ $F = 1$ states. The amplitude of 20 V/cm is necessary to fully remove the $2S_{1/2}$ $F = 1$ states, according to a simulation performed by the numerical calculation code described in Chapter 5.

Therefore, we sought for such geometry that enables the apparatus to resonate at an input frequency of 1.1 GHz, to enhance the MW power inside the apparatus and realize the amplitude around 20 V/cm.

4.3.1 Geometrical Optimization of HFS

In the parameter sweep simulation of the MWS, we have seen that the dip in the spectrum shifts towards the low-frequency side and the baseline of the spectrum rises up by increasing Y_b with Y_e fixed. This implies the possibility that a resonance property at a certain frequency can be implemented by tuning these parameters.

Figure 4.6 shows the simulated S_{11} for different values of Y_b, when Y_e was fixed to be 32 mm. The X_b and X_e were set to the same values as those of the MWS. The Z_b was set to 100 mm, which is the maximum value allowed under the mechanical constraints, in order to enhance the E-field intensity in between the electrodes rather than from the electrode to the rectangular box.

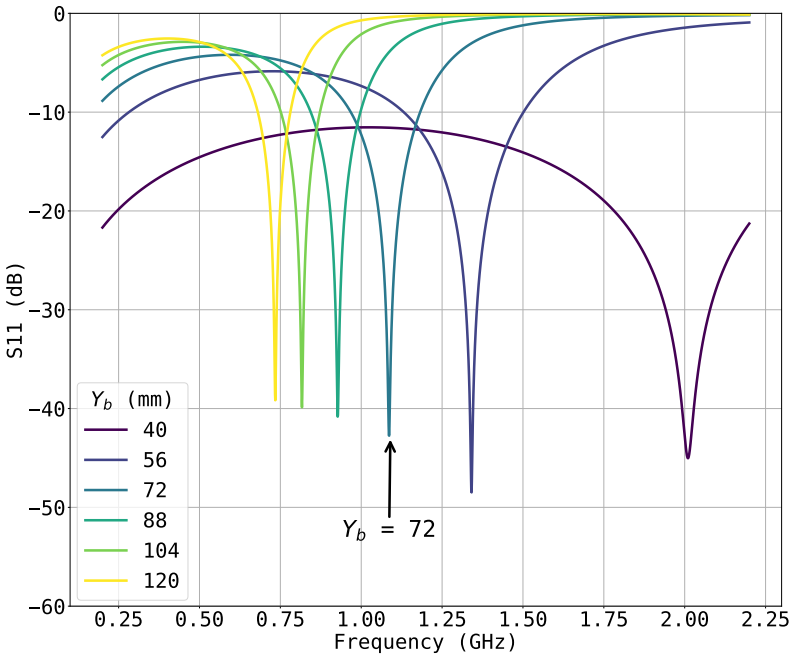

Figure 4.6: Simulated S_{11} of the HFS, for different values of Y_b.

As seen in Figure 4.6, the resonance peak position shifts to the low-frequency side and the baseline of the spectrum rises up by increasing Y_b. This indicates that the resonance property starts to show up at the frequency around the dip, and the Q value increases accordingly. To implement the resonance property at 1.1 GHz, the geometry with Y_b around 72 mm seems suitable, as annotated in Fig 4.6.

Therefore, we have decided to adopt the structure which enables adjustment of Y_b from 64 mm to 76 mm to tune the resonance frequency, with the same value as the 20 mm MW apparatus taken for Y_e, X_b, and X_e. Z_b was determined to be 100 mm, which gains the E-field intensity in between the electrodes.

Regarding the E-field amplitude, a 2D field map of time averaged vertical component of the amplitude is shown in Figure 5.3 in Section 5.2.3, calculated at a total input power of 10 W. One can see that the amplitude at the center of the apparatus is around 20 V/cm at (b) 1100 MHz.

4.4 Assembling and Fabrication

Based on the design optimized by the MW simulations, the 30 mm bore model MWS and HFS were produced. Mechanical realizations of these MW apparatuses, and measurements of S_{11} are described in the following, as well as productions of a support unit and a new vacuum chamber.

4.4.1 Assembling MWS

A mechanical realization similar to the 20 mm MW apparatus was adopted for the 30 mm MWS as well. Figure 4.7(a) shows the 2D drawing of the apparatus. The parameter Z_b is adjustable from 50 mm to 60 mm for tuning the frequency characteristic. For the adjustment, as shown in Figure 4.7(b), the dimension between top and bottom plate can be tuned by changing the number of washers used for screws to form the rectangular box from the copper plates. To fix the inner electrode on the horizontal plane, PEEK spacers were placed between the electrode and the box.

(a) (b)

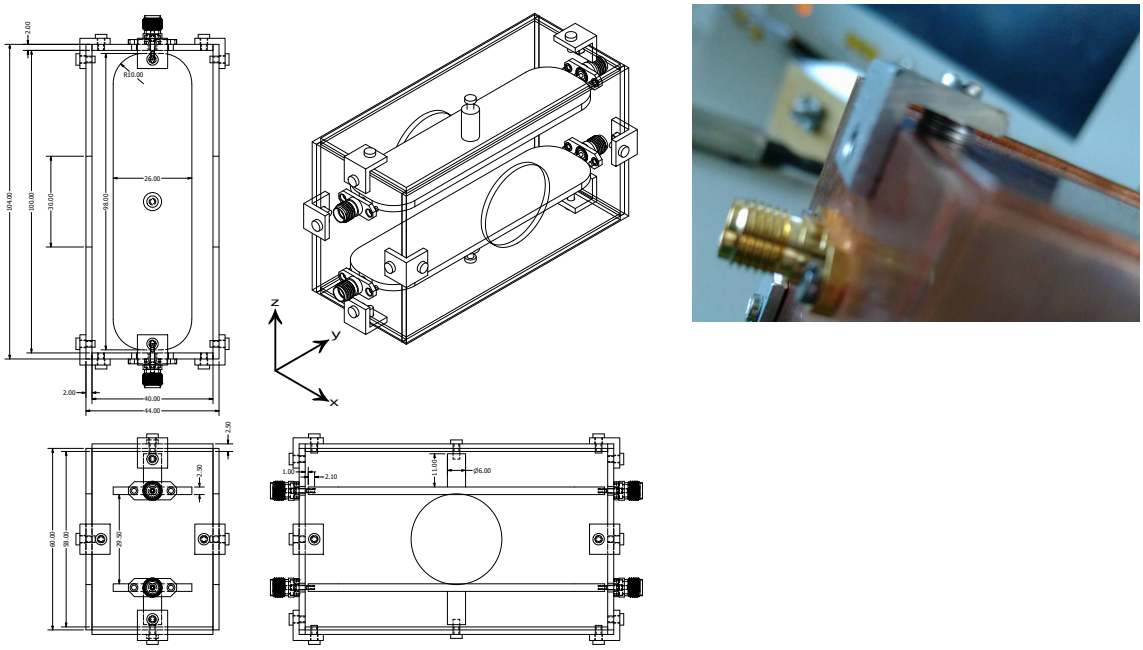

Figure 4.7: (a) 2D drawing of the 30 mm MWS and (b) adjustment of Z_b using washers at the screw to form the box.

The S_{11} of the manufactured MWS was measured using a Vector Network Analyzer

(Keysight E5061B). Figure 4.8 shows (a) Simulated and (b) measured S_{11} of the MWS, for different values of Z_b. One can see a good agreement in the overall shape of the spectrum between the simulations and measurements, and that the S_{11} is suppressed to be less than $-13\,\mathrm{dB}$ for the simulation and $-15\,\mathrm{dB}$ for the measurement, over the entire frequency range for each geometry.

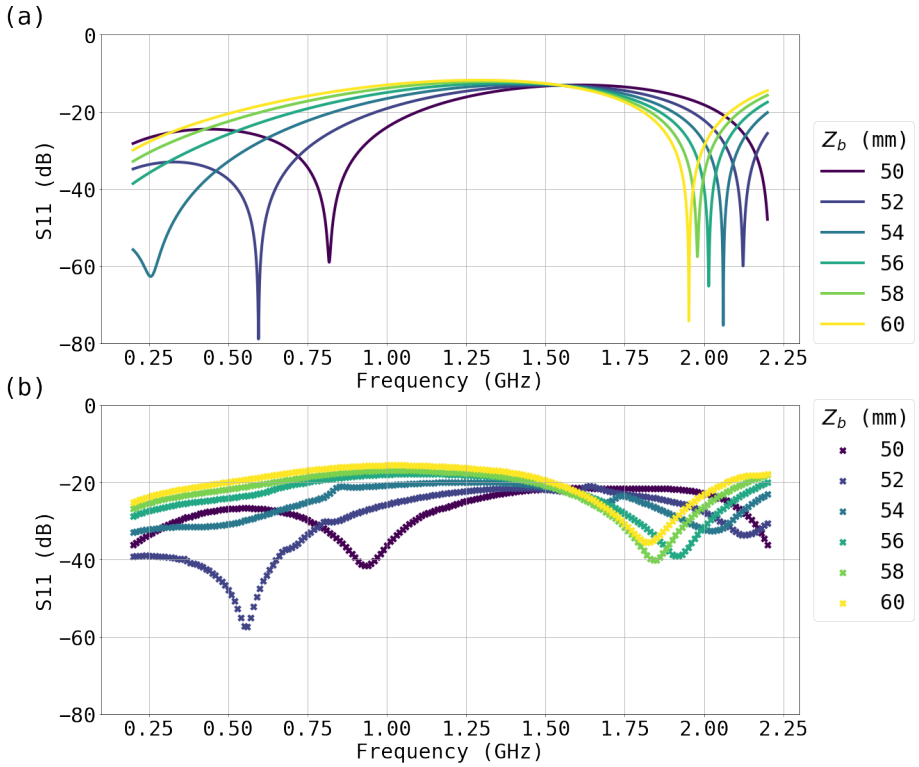

Figure 4.8: (a) Simulated and (b) measured S_{11} of the MWS, for different values of Z_b.

The discrepancy of each resonance peak position in the simulated and measured S_{11} spectrum in Figure 4.8, which is about 150 MHz at maximum for $Z_\mathrm{b} = 50$, is attributed to assembly inaccuracies relative to the ideal geometry of the CAD model used in the simulations.

In order to avoid the dip in the S_{11} spectrum around 0.6 GHz, or to reduce the frequency-dependence around the Lamb shift transition frequency, we have adopted Z_b of 60 mm for the installation as of 2023.

4.4.2 Assembling HFS

Similarly to the MWS, the HFS was assembled from copper plates to form the electrodes and rectangular box. Figure 4.9(a) shows the 2D drawing of the apparatus when the Y_b is set to the shortest value of 64 mm. The parameter Y_b is adjustable from 64 mm to 76 mm for tuning the resonance frequency. The same tuning mechanism as that of the MWS was adopted for the HFS as well.

To connect the electrode to the SMA connectors, as shown in Figure 4.9(b)(c), copper lines were inserted to the electrode for 2 mm, and the other end of the lines were inserted to the pin of the SMA connectors. The pin and copper line were soldered to ensure the electric contact before installing to the beam line. To fix the inner electrode on the horizontal plane, the electrodes were attached to the box through two alumina screws and

rectangular screw stands (7 mm × 7 mm × 5 mm). To avoid an air pocket inside the tap hole, a gas vent hole was made in each of the screw stands.

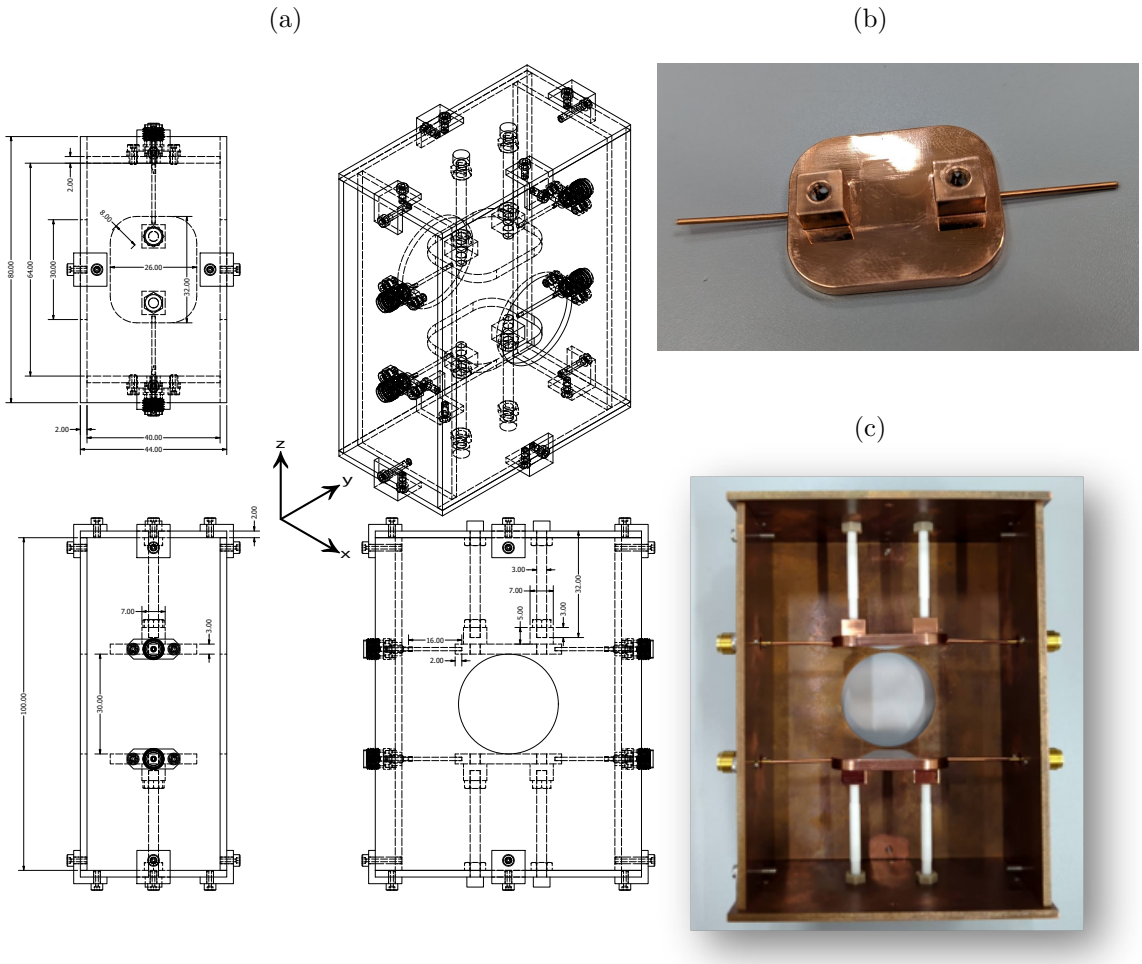

Figure 4.9: (a) 2D drawing of the 30 mm HFS, (b) inner electrode with copper lines to connect to SMA connectors, and (c) view inside the apparatus.

The S_{11} was measured for the HFS as well usign the VNA. In Figure 4.10 the (a) simulated and (b) measured S_{11} are compared for two different values of $Y_{\mathrm{b}} = 72$ and 76 mm.

For both geometries, one can see a dip around 1.1 GHz and a good agreement in the overall shape of the spectrum between the simulations and measurements. Quality factor of the resonance can be roughly evaluated to be on the order of 10, by dividing the resonance frequency on the order of 1 GHz the FWHM of the dip on the order of 100 MHz. The discrepancy between the simulated and measured S_{11} spectrum is attributed to the assembly accuracies, as well as the case of the MWS. We have adopted the Y_{b} of 72 mm for the installation as of 2023, confirming that the dip in the measured S_{11} emerged at 1135 MHz after the installation.

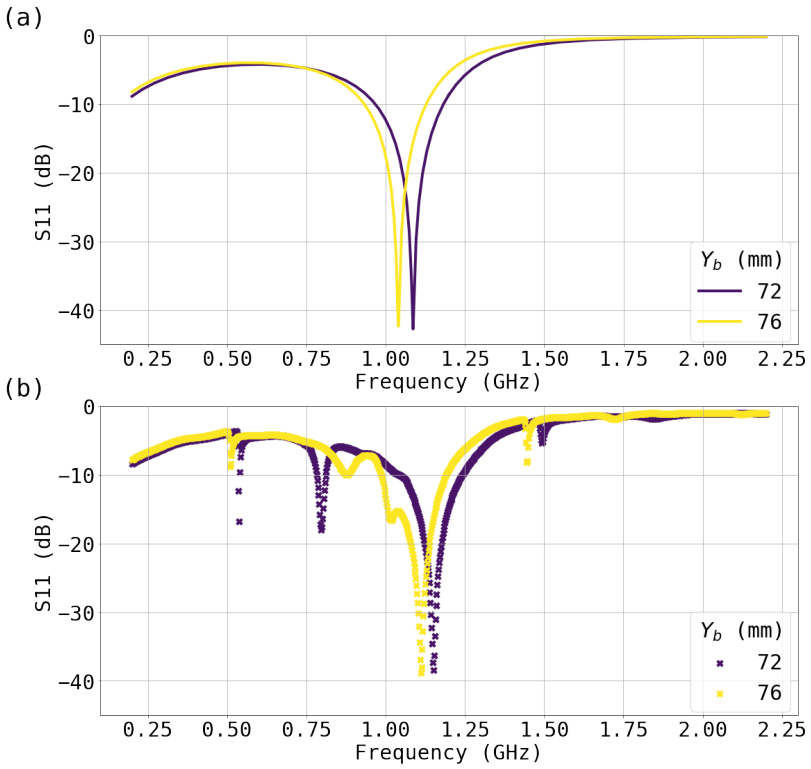

Figure 4.10: (a) Simulated and (b) measured S_{11} of the HFS, for different values of Y_b.

4.4.3 Support and Feedthrough

The produced 30 mm MW apparatuses were mounted on a aluminum support unit, as shown in Figure 4.11. The support consists of two 5 mm thick rings and two 20 mm thick rectangular frames for each MW apparatus. The frames were mounted on the rings by M4 screws. Between the ring and frame, 0.5 mm thick washers were inserted at each screw to reduce the contact surface and circumvent air pockets. On the frames, L-shaped angles were attached to hold the MW apparatus. Each angle has a slot-shaped through-holes to fix the MW apparatus by M2 screws. The distance from the slot center to the end of the angle is designed as (138 mm) for the apparatus to be centered on the beam axis. The slot has a length of 4 mm, so that one can adjust the position of the MW apparatus by up to $\pm$ 2 mm in the y-axis.

This support unit was mounted on the 4 channel SMA feedthrough shown in Figure 4.12. The flange is CF203 and made of SUS316L. On the vacuum side surface of the flange, 10 mm deep M4 tap holes were processed on the circumference of 60 mm radius as shown in Figure 4.12(a). The ring part of the support has through-holes at the corresponding positions to be mounted on the flange of the feedthrough using M4 screws as shown in Figure 4.12(b). The 0.5 mm thick washers were inserted between the flange and the ring as well to circumvent air pockets.

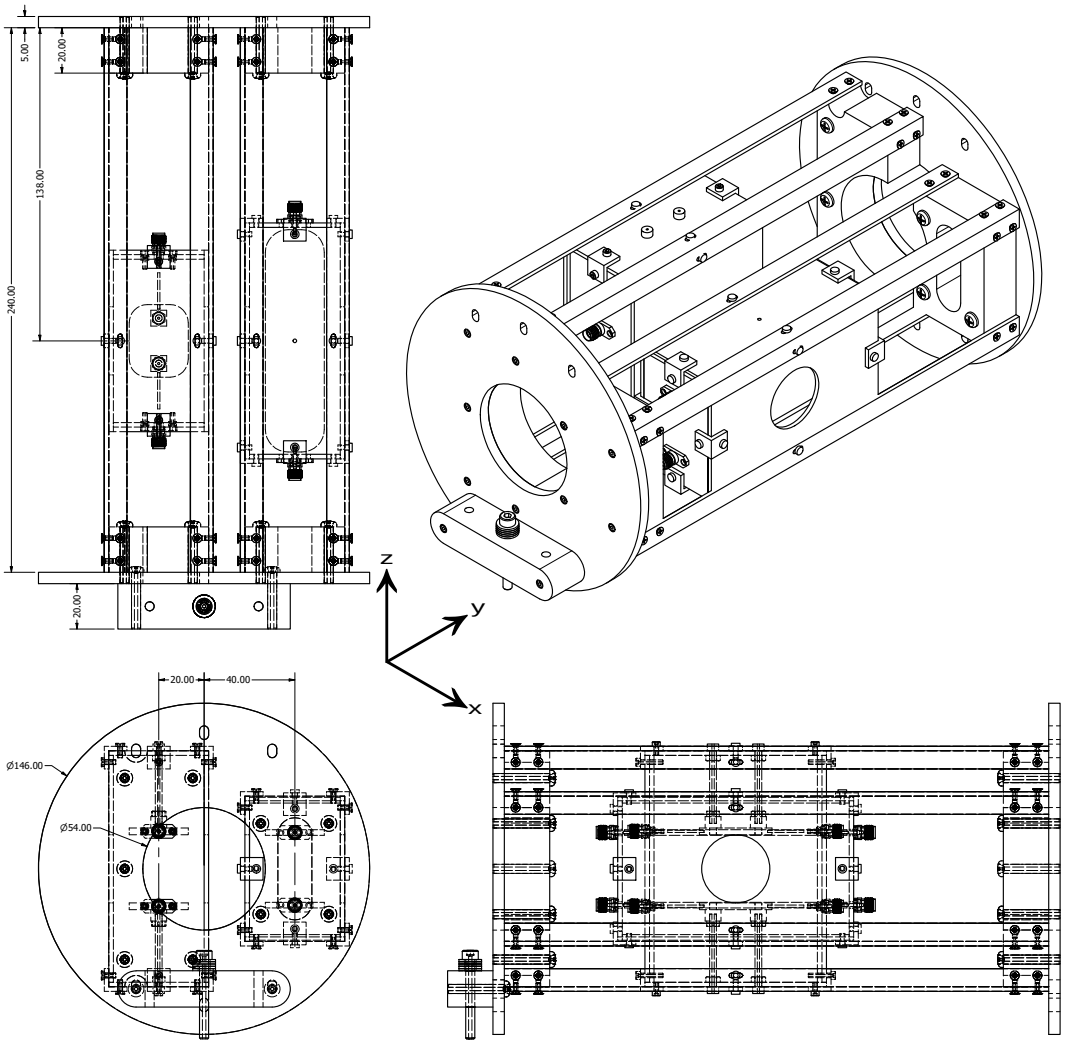

Figure 4.11: 2D drawing of the aluminum support with the MW apparatuses mounted on it.

(a) (b)

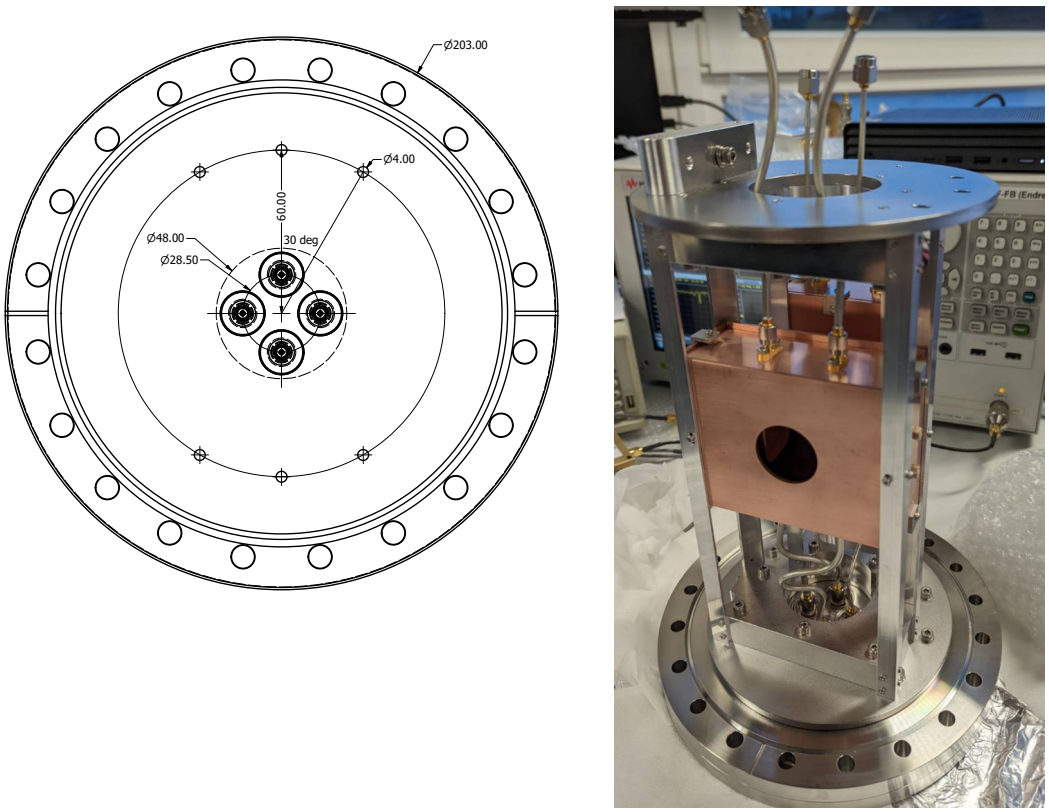

Figure 4.12: (a) 2D drawing of the 4 channel SMA feedthrough and (b) how the support is mounted on the feedthrough.

4.4.4 Vacuum Chamber

To accommodate the 30 mm MW spectrometer, the ultra-high vacuum chamber was also upgraded to a larger one as shown in Figure 4.13. The chamber and the accompanying flanges are all made of SUS316L, and A4 stainless screws were used everywhere to reduce the stray magnetic field. The MW spectrometer unit (the HFS, the MWS, the support, and the feedthrough) was installed through the CF203 port in the y-axis. At the CF152 port in the negaive z-axis, or right below the MW spectrometer, a turbo pump was attached. Above this CF152 port, there is a CF70 port to install a vacuum gauge. The upstream half space of the chamber is available for installation of further equipments in the future.

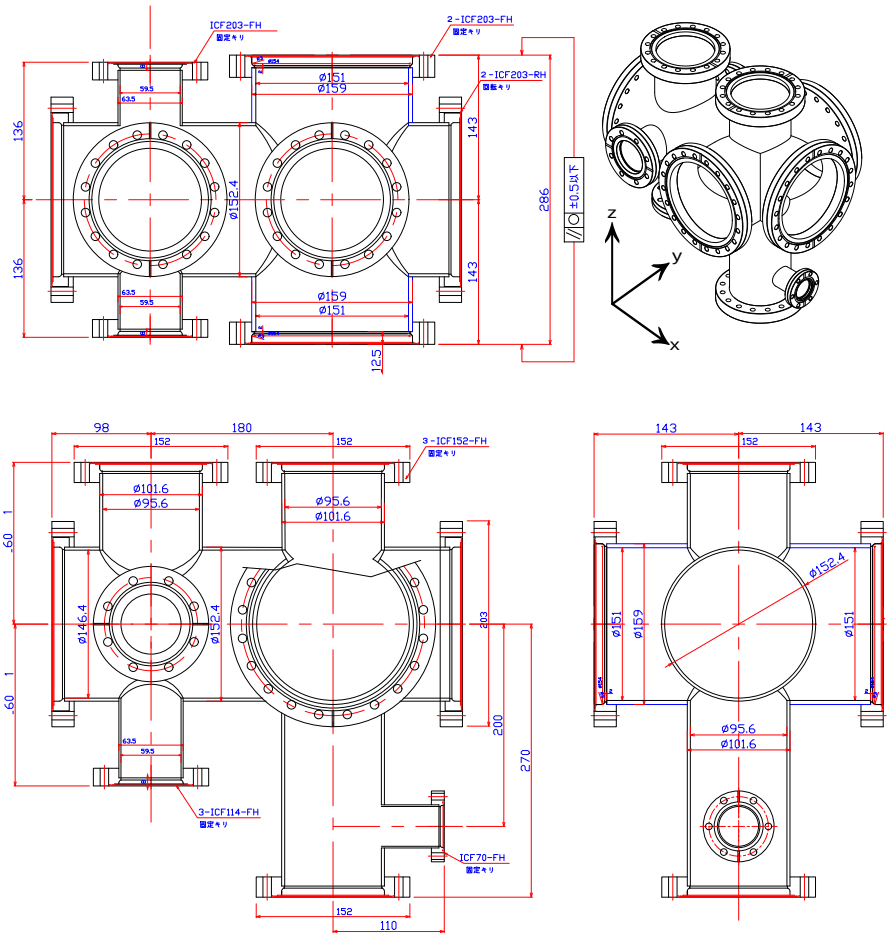

Figure 4.13: Ultra-high Vacuum chamber to install the MW spectrometer.

Figure 4.14 shows how the vacuum chamber looks with the MW spectrometer unit (the spectrometer shown in yellow, the support in blue) installed inside. The MW spectrometer unit was installed from the positive y-axis side, meaning that the ring part of the support is mounted on the feedthrough on this side. On the other side of the support, a clamp stand was machined on the ring part as seen in Figure 4.14. A M4 35 mm long screw was used as the clamp to stand on the inner surface of the chamber and prevent the entire MW spectrometer unit from shifting downward due to its weight.

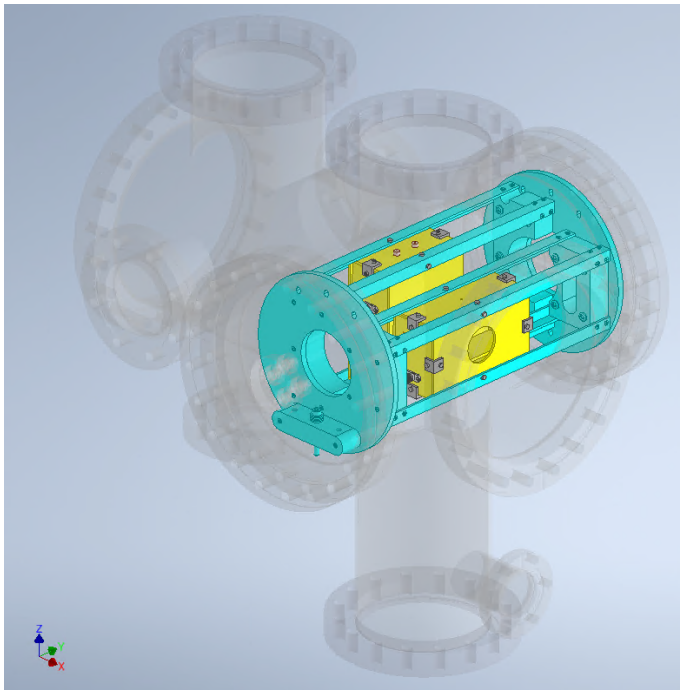

Figure 4.14: View of the vacuum chamber with the MW spectrometer unit installed.

4.5 MW Circuit Components

For both the MWS and HFS, a detailed description of the circuit components is given here. Figure 4.15 illustrates the circuit components for (a) the MWS and (b) HFS. To generate the MW signal, TektronixTSG4100A series products are used for both the MWS and HFS. In the MWS circuit, the signal from the generator is input typically at −3 dBm to the Mini-Circuits ZHL-10W-2G+ amplifier, and the amplified signal is input to the TRM HS101fc900 high power divider/combiner. The divided signals are then input to the feedthrough on the vacuum chamber. In the HFS circuit, the signal from the generator is first input to the Mini-Circuits ZFSCJ-2-232-S+ divider, then each of the divided signals is input to a Mini-Circuits amplifier of the same model as the MWS circuit.

The powers for these three Mini-Circuits amplifiers are provided by the Matsusada PRK30-53 power supply in parallel. The output voltage of the Matsusada power supply is set to 24 V, and the output current is set to 18 A to operate those three amplifiers, each of which requires 6 A to start up as specified on the datasheet. Once they start up, the total current consumption converges to about 12 A.

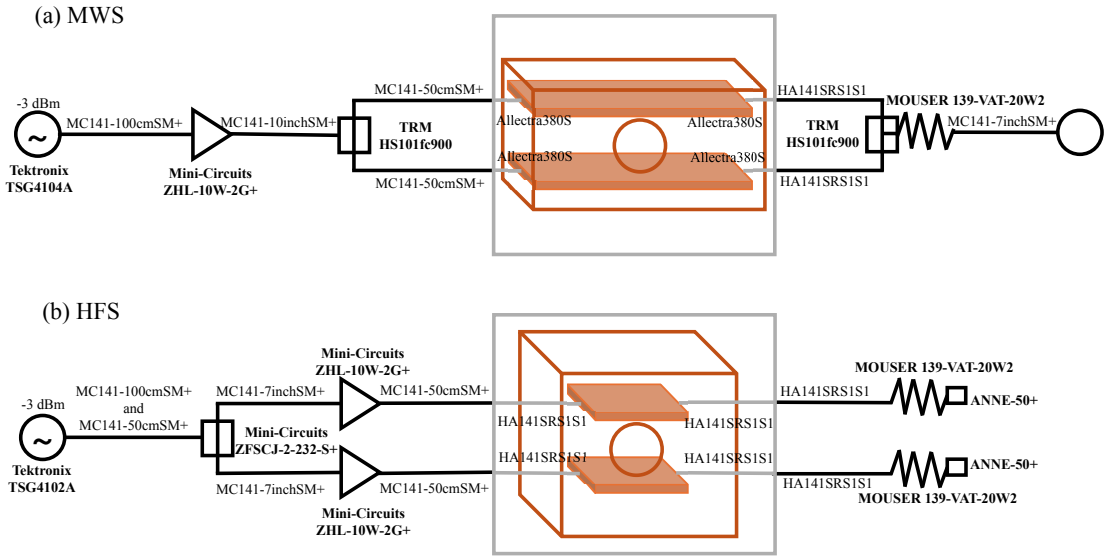

Figure 4.15: MW circuit components of (a) the MWS and (b) HFS.

The amplified signals are then input to the 4 channel SMA feedthrough. To transmit the signal inside the chamber, the Allectra 380-SMAK-MM UHV-compatible cables are used in the MWS circuit, and HASCO 141SR-S1-S1 cables are used in the HFS circuit. Pasternack PE4004 SMA connectors are used to feed the MW signal through the MW apparatus, as described in Section for the MWS and in Section for the HFS. The HASCO cables and the SMA connectors are not vacuum-compatible products. However, the pressure on the order of 10^{-9} mbar has been maintained after the installation and baking the vacuum chamber for 12 hours at temperature plateau of 120 °C. Also, these products as well as all the parts of MW apparatus were washed using a supersonic cleaner with isopropanol before the installation.

The same 4 channel SMA feedthrough is used as the exit port from the chamber as well. The signals in the MWS circuit are combined using TRM HS101fc900 (the same product as the divider), attenuated by a MOUSER 139-VAT-20W2, and monitored at the end using the ROHDE&SCHWARZ NRP18T power meter. In the HFS circuit, each of the signals from the feedthrough is attenuated by the same attenuator and terminated at

the end using Mini-Circuits ANNE-50+.

4.6 Control of MW Spectrometer

To control the Matsusada power supply, Tektronix signal generators, and ROHDE&SCHWARZ power meter, a dedicated control PC was installed. The power supply communicates with the PC via the GP-M cable and GP-MET2-9 connector from Matsusada, which interfaces the cable to a RS232-USB converter connected to the PC. The signal generators communicates with the PC in a local area network including the PC. The power meter communicates with the PC via a USB cable directly connected to the PC. Compiled LabVIEW softwares are running on the PC to control all these instruments using VISA API. Also, the output current of the power supply, and, the frequency, amplitude, temperature at output terminal of the signal generators are logged at the moment of extracting the beam from the $\bar{p}$ trap (or the AD/ELENA for the pass-through beam).

4.7 Characterization of MW spectrometer

For the passive components such as the cables, power divider/combiner, MWS, HFS, and attenuators, the S-parameters were measured using the Keysight E5061B vector network analyzer. For the active components such as the signal generators and the combination of each generator and the amplifiers, the power spectra were measured using the ROHDE&SCHWARZ power meter with the MOUSER attenuators not to exceed the input power limit of 20 dBm for the power meter. From these offline characterizations, each of the MW circuit components was confirmed to have the expected performance.

In the spectroscopy experiment, the amplitude of the MW E-field interacting with the atoms should be calculated in order to interpret the measured line shape. To calculate the E-field amplitude, one should first estimate the power fed on the MW apparatus during the experiment. Then, the estimated power can be input to simulation models of the apparatuses developed on CST Microwave Studio to numerically calculate the distribution of the E-field amplitude.

Such an in situ power estimation can be performed by correcting the value monitored at the power meter using the S-parameters of the circuit components measured in advance by a vector network analyzer.

Figure shows the spectrum of the total input power (blue) and the total output power (orange) when the signal generator outputs the power of −3 dBm (0.5 mW). The total input power is more than 37 dBm (5 W) from 700 MHz to 1300 MHz, and the spectrum peaks around 900 MHz with the power reaching almost 10 W. A part of this frequency-dependence is due to the characteristic of the high power divider, which is a custom made product to realize the highest signal transmission around 900 MHz. Another part of the dependence is due to the characteristic of the amplifier, which guarantees the typical gain of 43 dB in the range from 800 MHz to 2000 MHz.

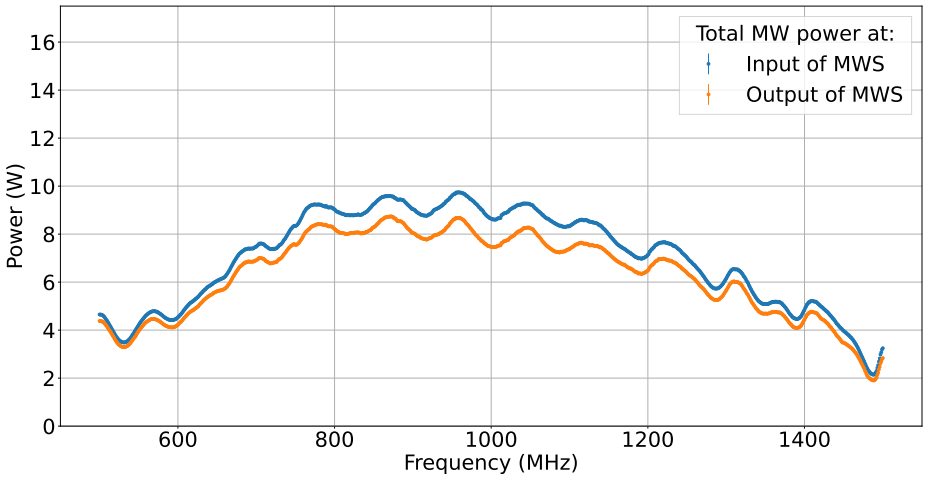

Figure 4.16: Total input power (blue) and the total output power (orange) to the MWS when the signal generator outputs the power of −3 dBm (0.5 mW).

Figure shows the same plots for the HFS. For the HFS, the total input power peaks at 1135 MHz with the power reaching 16 W, which is attributed to the resonance property designed around 1.1 GHz. It should be noted that the resonance peak appears less clear in the plot for the output power than that for the input power. This could indicate that the power is input to the HFS at least but dissipated or absorbed before transmitting through

the HFS, which requires further investigations.

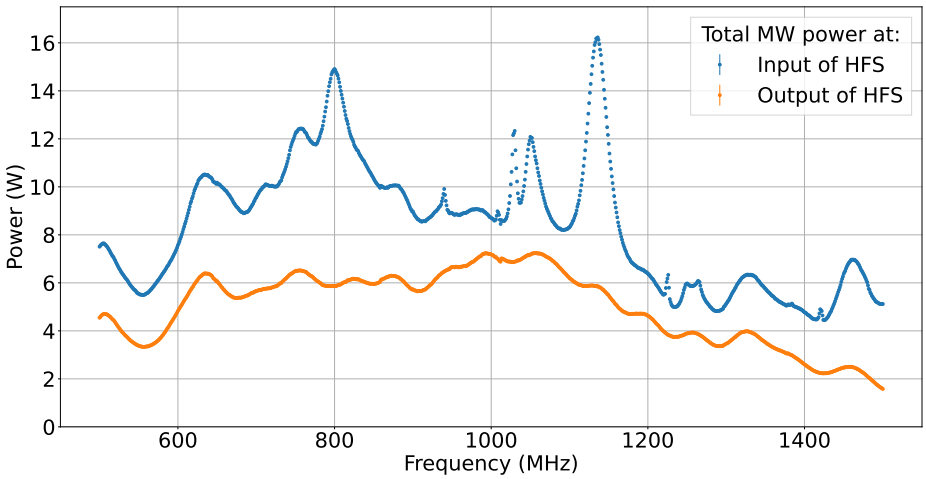

Figure 4.17: Total input power (blue) and the total output power (orange) to the HFS when the signal generator outputs the power of −3 dBm (0.5 mW).

4.8 Conclusion

We developed a 30 mm bore model MW spectrometer for the Lamb shift spectroscopy planned in the GBAR experiment. Concerning the MWS, the geometric parameters were optimized to suppress the frequency-dependence of the power transmission and form a MW E-field with the amplitude around 10 V/cm over the frequency range to scan in order to draw clear Lamb shift spectrum. Concerning the HFS, the geometric parameters were optimized for the apparatus to resonate at 1.1 GHz to form a relatively intense MW E-field with the amplitude around 20 V/cm in order to fully remove the $2S_{1/2}$ $F = 1$ states.

Additionally, a support unit to mount the MW apparatuses and a new vacuum chamber to house the spectrometer were produced, and installed in the GBAR $\bar{\mathrm{H}}$ beam line. Furthermore, LabVIEW softwares were developed to control and log parameters of the MW circuit.

After the installation of the spectrometer, we established a method for an online power characterization of the spectrometer, to confirm that the expected amount of power was input for both the MWS and HFS. Towards the Lamb shift measurement, this online power characterization will enable adjustment of the input power at the signal generator in order to keep constant input power at the MWS over the frequency range to scan.

Chapter 5

Simulation of Spectroscopy

We developed a numerical calculation program to simulate the $\bar{\mathrm{H}}$ Lamb shift spectroscopy. Since the $\bar{\mathrm{H}}$ beam produced in the GBAR beam line is expected to have a relatively large spatial spread, the program takes into account 3D spatial distributions of the E-field formed by the HFS, MWS, and Lyman-α detector.

The developed program was utilized for calculating theoretical line shapes of the Lamb shift transition to check the performance of the MW spectrometer, and also for evaluating the Lyman-α detector's efficiency by executing a Monte Carlo simulation of the Lyman-α photon emission. Furthermore, we predicted the spectroscopy precision that can be achieved for certain periods of the data-taking by combining the line shape calculation and Monte Carlo simulation.

5.1 Time Dependent Schrödinger Equation of Lamb Shift

The core of the numerical calculaition program is the solver of a time-dependent Schrödinger equation with a Hamiltonian $\mathscr{H}_{\mathrm{Lamb}}$ expressed as follows:

$$i\hbar\frac{\partial}{\partial t}\Psi(t) = \mathscr{H}_{\mathrm{Lamb}}(t)\Psi(t) \tag{5.1}$$

Assuming that the state $\Psi(t)$ can be sufficiently represented by a linear combination of the eigenfunctions of all the sublevels in the $2S_{1/2}$ and $2P_{1/2}$ states, $\Psi(t)$ can be expressed as follows:

$$\Psi(t) = \begin{pmatrix} s_{00}(t) \\ s_{1-1}(t) \\ s_{10}(t) \\ s_{11}(t) \\ p_{00}(t) \\ p_{1-1}(t) \\ p_{10}(t) \\ p_{11}(t) \end{pmatrix} \tag{5.2}$$

where each element is the probability amplitude of the eigenfunction of each $2S$ and $2P$ state, with the first subscript denoting the total angular momentum quantum number F, and the second subscript the total magnetic quantum number m_F.

Under this assumption, $\mathscr{H}_{\mathrm{Lamb}}$ can be approximated as a finite matrix in the following:

$$\mathscr{H}_{\mathrm{Lamb}}(t) = \mathscr{H}_0 + \mathscr{H}_{\mathrm{int}}(t) + \mathscr{H}_{\mathrm{decay}} \tag{5.3}$$

where

$$
\mathscr{H}_0 = \begin{pmatrix}
E_{S_{00}} & 0 & 0 & 0 & 0 & 0 & 0 & 0 \\
0 & E_{S_{1-1}} & 0 & 0 & 0 & 0 & 0 & 0 \\
0 & 0 & E_{S_{10}} & 0 & 0 & 0 & 0 & 0 \\
0 & 0 & 0 & E_{S_{11}} & 0 & 0 & 0 & 0 \\
0 & 0 & 0 & 0 & E_{P_{00}} & 0 & 0 & 0 \\
0 & 0 & 0 & 0 & 0 & E_{P_{1-1}} & 0 & 0 \\
0 & 0 & 0 & 0 & 0 & 0 & E_{P_{10}} & 0 \\
0 & 0 & 0 & 0 & 0 & 0 & 0 & E_{P_{11}}
\end{pmatrix}
$$

$$
\mathscr{H}_{\mathrm{int}}(t) = \begin{pmatrix}
-\frac{\hbar}{2}\mathrm{i}\gamma_{2S2P} & 0 & 0 & 0 & 0 & 0 & U(t) & 0 \\
0 & -\frac{\hbar}{2}\mathrm{i}\gamma_{2S2P} & 0 & 0 & 0 & U(t) & 0 & 0 \\
0 & 0 & -\frac{\hbar}{2}\mathrm{i}\gamma_{2S2P} & 0 & U(t) & 0 & 0 & 0 \\
0 & 0 & 0 & -\frac{\hbar}{2}\mathrm{i}\gamma_{2S2P} & 0 & 0 & 0 & U(t) \\
0 & 0 & U^*(t) & 0 & -\frac{\hbar}{2}\mathrm{i}\gamma_{2S2P} & 0 & 0 & 0 \\
0 & U^*(t) & 0 & 0 & 0 & -\frac{\hbar}{2}\mathrm{i}\gamma_{2S2P} & 0 & 0 \\
U^*(t) & 0 & 0 & 0 & 0 & 0 & -\frac{\hbar}{2}\mathrm{i}\gamma_{2S2P} & 0 \\
0 & 0 & 0 & U^*(t) & 0 & 0 & 0 & -\frac{\hbar}{2}\mathrm{i}\gamma_{2S2P}
\end{pmatrix}
$$

$$
\mathscr{H}_{\mathrm{decay}} = \begin{pmatrix}
-\frac{\hbar}{2}\mathrm{i}\gamma_{2S} & 0 & 0 & 0 & 0 & 0 & 0 & 0 \\
0 & -\frac{\hbar}{2}\mathrm{i}\gamma_{2S} & 0 & 0 & 0 & 0 & 0 & 0 \\
0 & 0 & -\frac{\hbar}{2}\mathrm{i}\gamma_{2S} & 0 & 0 & 0 & 0 & 0 \\
0 & 0 & 0 & -\frac{\hbar}{2}\mathrm{i}\gamma_{2S} & 0 & 0 & 0 & 0 \\
0 & 0 & 0 & 0 & -\frac{\hbar}{2}\mathrm{i}\gamma_{2P} & 0 & 0 & 0 \\
0 & 0 & 0 & 0 & 0 & -\frac{\hbar}{2}\mathrm{i}\gamma_{2P} & 0 & 0 \\
0 & 0 & 0 & 0 & 0 & 0 & -\frac{\hbar}{2}\mathrm{i}\gamma_{2P} & 0 \\
0 & 0 & 0 & 0 & 0 & 0 & 0 & -\frac{\hbar}{2}\mathrm{i}\gamma_{2P}
\end{pmatrix}
\tag{5.4}
$$

In the first matrix $\mathscr{H}_0$, the diagonal elements denote the eigen energies of the corresponding states in Equation (5.2) when taking the lowest energy state, $2P(F=0, m_F=0)$ state as the reference level. These elements are further represented as:

$$
\begin{aligned}
E_{S_{00}} &= \hbar(\omega_{910} + \omega_{2P}^{\mathrm{HFS}}) \\
E_{S_{1-1}} &= \hbar(\omega_{910} + \omega_{2P}^{\mathrm{HFS}} + \omega_{2S}^{\mathrm{HFS}}) \\
E_{S_{10}} &= \hbar(\omega_{910} + \omega_{2P}^{\mathrm{HFS}} + \omega_{2S}^{\mathrm{HFS}}) \\
E_{S_{11}} &= \hbar(\omega_{910} + \omega_{2P}^{\mathrm{HFS}} + \omega_{2S}^{\mathrm{HFS}}) \\
E_{P_{00}} &= 0 \\
E_{P_{1-1}} &= \hbar(\omega_{910} + \omega_{2P}^{\mathrm{HFS}}) \\
E_{P_{10}} &= \hbar(\omega_{910} + \omega_{2P}^{\mathrm{HFS}}) \\
E_{P_{11}} &= \hbar(\omega_{910} + \omega_{2P}^{\mathrm{HFS}})
\end{aligned}
\tag{5.5}
$$

where ω_{910}, $\omega_{2S}^{\mathrm{HFS}}$, and $\omega_{2P}^{\mathrm{HFS}}$ denote the resonance frequency of the 910 MHz transition, $2S(F=1)$ state hyperfine transition, and $2P(F=1)$ state hyperfine transition, respectively. For the computation, these frequencies are defined as 909.887 MHz, 177.556 86 MHz, and 59.1696 MHz, respectively [7]. Thus, the resonance frequencies of the 910 MHz, 1088 MHz, 1147 MHz transitions are set as follows:

$$
\begin{aligned}
\omega_{910} &= 909.887 \text{ MHz} \\
\omega_{1088} &= \omega_{910} + \omega_{2S}^{\mathrm{HFS}} = 1087.444 \text{ MHz} \\
\omega_{1147} &= \omega_{910} + \omega_{2S}^{\mathrm{HFS}} + \omega_{2P}^{\mathrm{HFS}} = 1146.613 \text{ MHz}
\end{aligned}
\tag{5.6}
$$

In the second matrix $\mathscr{H}_{\mathrm{int}}$, the interaction with the E-fields are represented. The off-diagonal element U and its complex conjugate U^* denote the coupling terms with the MW

E-field formed by the MW spectrometer. U is calculated as:

$$\begin{aligned} U(t) =& \left\langle 2S_{F,m_F} | q\boldsymbol{r} \cdot \boldsymbol{E} \cos\omega t | 2P_{F',m_F'} \right\rangle \\ =& q\cos\omega t \left\langle 2S_{F,m_F} \left| xE_x + yE_y + zE_z \right| 2P_{F',m_F'} \right\rangle \\ =& q\cos\omega t \int \varphi_{200}^* \left(xE_x + yE_y + zE_z \right) \frac{1}{\sqrt{3}} \left(\varphi_{21-1} + \varphi_{210} + \varphi_{211} \right) d\boldsymbol{r} \\ =& \frac{3a_0 q\cos\omega t}{\sqrt{3}} \left(-\sqrt{2}iE_y + E_z \right) \end{aligned} \tag{5.7}$$

where the $2S$ state eigenfunction with a total angular momentum quantum number F and a total magnetic quantum number m_F is dontoed as $|2S_{F,m_F}\rangle$, and the $2P$ state eigenfunction with a total angular momentum quantum number $F^{'}$ and a total magnetic quantum number $m_F^{'}$ is dontoed as $|2P_{F',m_F'}\rangle$. The vector of the MW E-field amplitude is represented as $\boldsymbol{E} = (E_x, E_y, E_z)$. q, ω, and a_0 denote the charge of the electric dipole moment i.e. the elementary charge in the case of H($\bar{\text{H}}$) atom, the frequency of the MW E-field, and the Bohr radius, respectively. Also, φ_{nlm} denotes the eigenfunction of H($\bar{\text{H}}$) atom with a principle quantum number n, an orbital angular momentum quantum number l, and a magnetic quantum number m. The integral is performed with regard to position $\boldsymbol{r}$ for an infinite volume. It is assumed that $|2P_{F',m_F'}\rangle$ can be represented as a superposition of the eigenfunctions with different magnetic quantum number m.

In addition, the decay terms due to the Stark mixing with the DC E-field formed by the Lyman-α detector are represented as the diagonal elements in the second matrix. For hydrogen-like atoms, the decay rate of the $2S_{1/2} - 2P_{1/2}$ hybrid state due to the Stark mixing is calculated to be [2, 77]:

$$\gamma_{2S2P} = \gamma_{2S} + \gamma_{2P}|\mathbf{E}|^2 \left[\frac{|V|^2}{\omega_{\text{Lamb}}^2 + \Gamma_{2P}^2/4} + \frac{|W|^2}{\omega_{\text{fine}}^2 + \Gamma_{2P}^2/4} \right] \cdot \eta + O\left(|\mathbf{E}|^4\right) \text{ Hz} \tag{5.8}$$

where η denotes a constant factor:

$$\eta = 1.63721 \text{ cm}^2/\text{V}^2 \tag{5.9}$$

also, ω_{Lamb} and ω_{fine} represent the resonance frequencies of the $2S_{1/2}$-$2P_{1/2}$ Lamb shift transition and the $2S_{1/2}$-$2P_{3/2}$ fine structure transition in MHz, respectively. The decay rate of $2S$ state and $2P$ state are denoted by $\gamma_{2\text{S}}$ and $\gamma_{2\text{P}}$. $\boldsymbol{E}$ represents the DC E-field amplitude. Γ_{2P}, V, and W are calculated as:

$$\Gamma_{2P} = 99.7Z^4 \text{ MHz} \tag{5.10}$$

$$V = (\sqrt{3}/Z)\left[1 - (5/12)\alpha^2 Z^2\right] \text{ MHz} \tag{5.11}$$

$$W = (\sqrt{6}/Z)\left(1 - \frac{1}{6}\alpha^2 Z^2\right) \text{ MHz} \tag{5.12}$$

where Z and α denotes the atomic number and the fine structure constant.

In the last matrix $\mathscr{H}_{\text{decay}}$, the spontaneous decay rate of each $2S$ and $2P$ states are represented, which are calculated as follows [77]:

$$\gamma_{2S} = 8.2294 \times Z^6 + 2.496 \times 10^{-6} \text{ Hz} \tag{5.13}$$

$$\gamma_{2P} = 6.265 \times 10^8 \text{ Hz} \tag{5.14}$$

5.2 Distribution of Beam and E-field

Based on the Hamiltonian (5.3), the time development of the state (5.2) is calculated by taking into account 3D distributions of the $\bar{\mathrm{H}}$ beam, MW E-fields formed by the HFS and MWS, and DC E-field formed by the Lyman-α detector.

5.2.1 $\bar{\mathrm{H}}$ Beam Distribution

In the $\bar{\mathrm{H}}$ production experiment in 2022, the beam transmission efficiency from the Ps target to $\bar{\mathrm{H}}$ Detector, evaluated by SIMION simulations, was 68% as an upper limit for the $\bar{\mathrm{H}}$, and 74% for the $\bar{p}$, respectively [44]. Figure 5.1 illustrates trajectories of the $\bar{\mathrm{H}}$ beam reconstructed from this transmission efficiency. The trajectories have a uniform angle spread within a certain range.

The beam diameters at the center of the HFS, MWS, Lyman-α detector, and $\bar{\mathrm{H}}$ detector are about 16 mm, 18 mm, 24 mm, and 48 mm, respectively. In the simulation program, the $\bar{\mathrm{H}}$ atoms are tracked on these trajectories and the interactions with the E-fields are calculated.

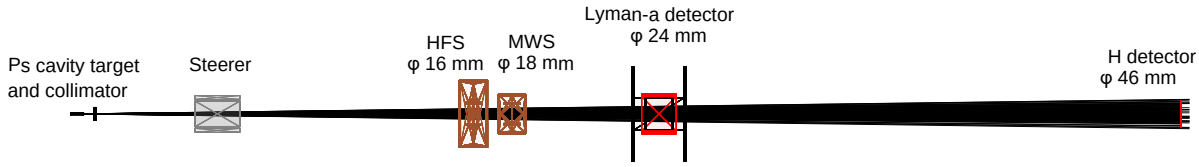

Figure 5.1: Trajectories of the $\bar{\mathrm{H}}$ beam in 2022, reconstructed from the transmission efficiency of 68%. The beam diameter at the center of each component is denoted.

5.2.2 MW E-field Formed by MWS

Concerning spatial distributions of the MW E-field formed by the MWS, a 3D grid data of time-averaged E-field amplitude at a total input MW power of 2 W was generated by using the CST simulation for input MW frequencies from 600 MHz to 1500 MHz by 10 MHz. The data points were generated at 1 mm intervals in each x, y, and z direction. The grid data at each frequency can be input to the simulation program at an arbitrary input MW power by scaling the original power. Figure 5.2 shows the 2D field map of E_z cut by yz plane at a total input MW power of 10 W for different frequencies of (a) 600, (b) 1100, (c) 1500, and (d) 2000 MHz. One can see almost identical distributions regardless of the variation of frequency, as it was designed as a MW transmission line for this frequency range to suppress the frequency-dependency of the power transmission.

5.2.3 MW E-field Formed by HFS

For spatial distributions of the MW E-field formed by the HFS, the 3D grid data was generated likewise. Figure 5.3 shows the 2D field map of E_z cut by yz plane at a total input MW power of 10 W for different frequencies of (a) 600, (b) 1100, (c) 1500, and (d) 2000 MHz. One can see that the maps are relatively frequency-dependent, and the overall distribution is the highest at 1100 MHz, as it was designed to resonate around this frequency for an effective selection of the unwanted $2S(F = 1)$ state.

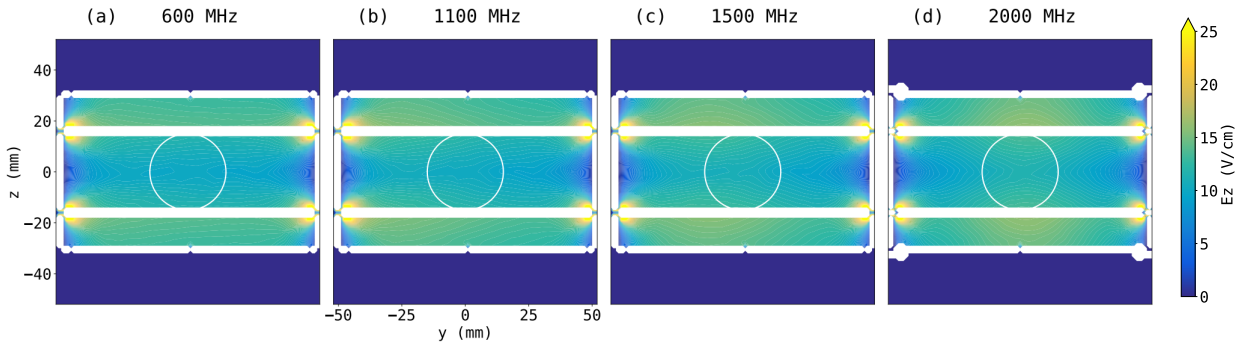

Figure 5.2: 2D field map of time averaged E_z formed by the MWS at a total input power of 10 W, cut by yz plane. The maps are drawn for different frequencies of (a) 600, (b) 1100, (c) 1500, and (d) 2000 MHz.

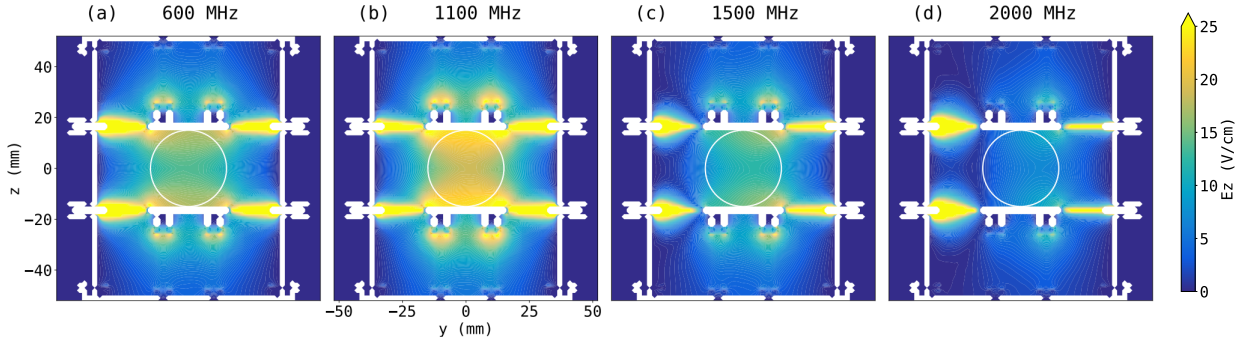

Figure 5.3: 2D field map of time averaged E_z formed by the HFS at a total input power of 10 W, cut by yz plane. The maps are drawn for different frequencies of (a) 600, (b) 1100, (c) 1500, and (d) 2000 MHz.

5.2.4 DC E-field Formed by Lyman-α Detector

Concerning the DC E-field formed by the Lyman-α detector, the 3D grid data was calculated by using a DC field solver in the CST Studio. Similarly to the case of the MWS and HFS, grid data was generated at 1 mm intervals in all three dimensions. Figure 5.3 shows a 2D field map of absolute values of the DC E-field vectors, (a) with the downstream electrode applied 3000 V and the upstream electrode grounded, and (b) with the downstream electrode applied 1500 V and the upstream electrode -1500 V. The support and shielding grid of the detector is denoted in (a). The shielding grid is supposed to intercept the DC-E-field from affecting the bias E-field inside the MCPs, and vice versa.

The geometrical efficiency for the MCPs to accept the emitted Lyman-α photons are compared in Section 5.5, for the E-field configuration (a) and (b) in Figure 5.4.

5.3 Particle Tracking

The $\bar{\mathrm{H}}$ atoms are generated along trajectories sampled from the spatial distribution discussed in Section 5.2.1, and tracked on the trajectories with a time step of 1 ns. During the stepping of 1 ns, the time-dependent Schrödinger equation (5.1) is solved as a set of ordinary differential equations, by using a Runge-Kutta method implemented in scipy.integrate.solve_ivp [90].

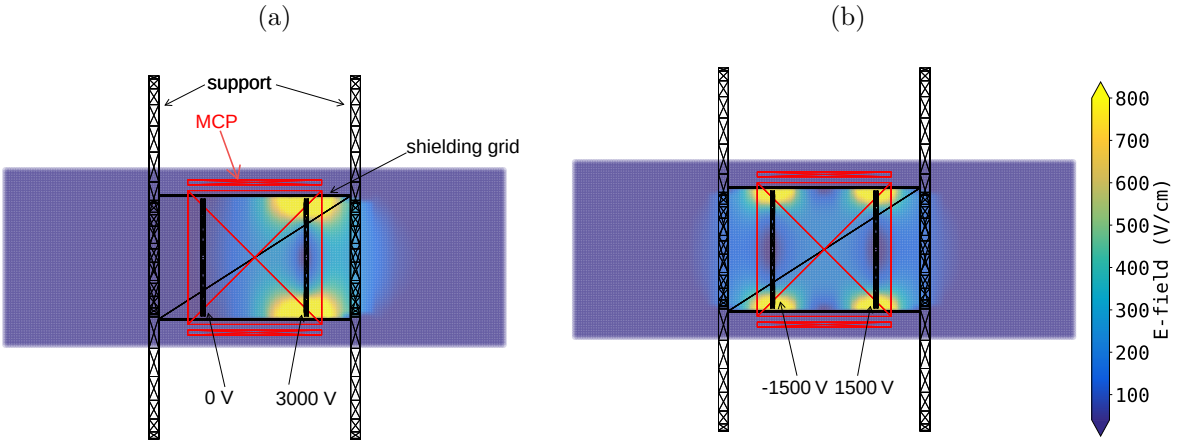

Figure 5.4: 2D field map of an absolute value of the DC E-field vector formed by the Lyman-α detector, (a) with the downstream electrode applied 3000 V and the upstream electrode grounded, and (b) with the downstream electrode applied 1500 V and the upstream electrode -1500 V.

In each step, interactions between the $\bar{\mathrm{H}}$ atom with the E-fields formed by the HFS, MWS, and Lyman-α detector are calculated, adopting the grid points of each field which is the closest to the midpoint of each step. Based on the change in the $2S$ state population before and after the stepping, which is computed from the probability amplitude in each element in the state (5.2), a probability of the deexcitation from the $2S_{1/2}$ to $2P_{1/2}$ state is calculated. Using this probability, a Monte Carlo sampling of the Lyman-α photon emission is executed.

The Lyman-α photon emitted through the Stark mixing between the $2S_{1/2}$ and $2P_{1/2}$ state is known to possess an anisotropy in its angular distribution. The level of anisotropy is correlated to the Lamb shift, and the $2S_{1/2} - 2P_{1/2}$ Lamb shift in deuterium (D) was measured utilizing this characteristic [91].

For the Stark mixing between the $2S_{1/2}$ and $2P_{1/2}$ state, the anisotropy was calculated as [77]:

$$I(\theta) \propto 1 + \mathrm{Re}(\rho)\left(1 - 3\cos^2\theta\right) + |\rho|^2 \frac{1}{2}\left(5 - 3\cos^2\theta\right) \tag{5.15}$$

where

$$\rho = \beta/\alpha \tag{5.16}$$

$$\psi = N^{-1/2}\left[\phi\left(2S_{1/2}\right) + \alpha\phi\left(2P_{1/2}\right) + \beta\sqrt{2}\phi\left(2P_{3/2}\right)\right] \tag{5.17}$$

and the θ, ψ, N, and ϕ denote an angle between the DC E-field and the direction of emitted Lyman-α photon, the state function, a normalization coefficient, and an eigenfunction of the eigen state in the bracket. The α and β represent probability coefficients of the $2P_{1/2}$ and $2P_{3/2}$ state, respectively. The ρ can be approximated under weak E-field assumption [77] to the following form as the lower limit:

$$\rho = \frac{E\left(2S_{1/2}\right) - E\left(2P_{1/2}\right) + i\Gamma_{2P}/2}{E\left(2S_{1/2}\right) - E\left(2P_{3/2}\right) + i\Gamma_{2P}/2} + O\left(|\mathbf{E}|^2\right) \tag{5.18}$$

and the intensity distribution of the Lyman-α photon emission can be calculated as shown in Figure 5.5.

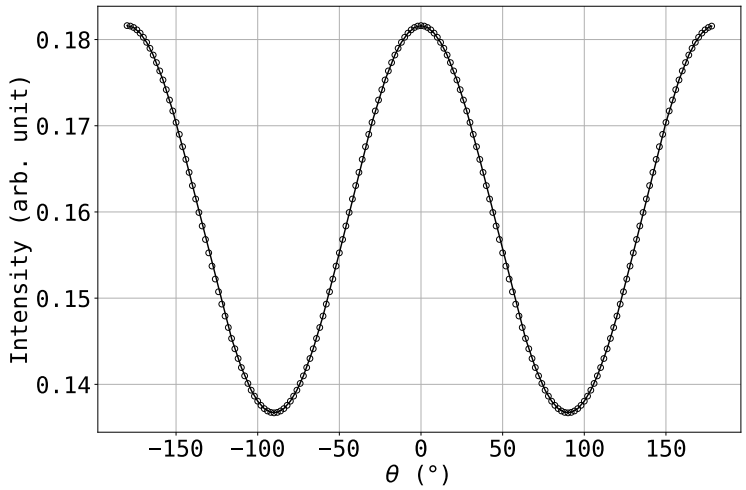

Figure 5.5: Normalized angular distribution of Lyman-α photons emitted from $\bar{\mathrm{H}}$ atoms via the Stark mixing between the $2S_{1/2}$ and $2P_{1/2}$ state under weak E-field assumption.

In the simulation program, trajectories of the Lyman-α photons are generated classically as line segments. Figure 5.6 shows an example of trajectory of a $\bar{\mathrm{H}}$ atom (the black line) flying from the left to the right and a Lyman-α photon (the green line). Also, a hit point of the photon on the MCP is represented as the blue cross.

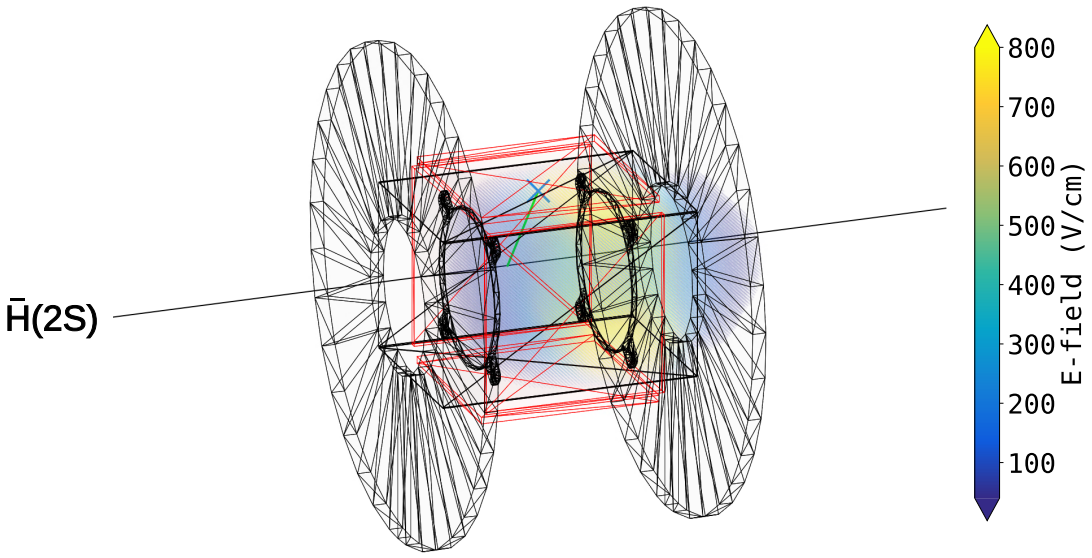

Figure 5.6: Trajectory of a $\bar{\mathrm{H}}$ atom (the black line) flying from the left to the right and a Lyman-α photon (the green line). A hit point of the photon on the MCP is represented as the blue cross.

5.4 State Selection Efficiency of HFS

One of the applications of the simulation program is to evaluate a necessary MW power to input to the MW apparatuses for inducing the Lamb shift transitions. For example, the state selection efficiency of the HFS was investigated. Figure 5.7 shows simulated line shapes of the Lamb shift transition obtained with different total MW powers input to the HFS while a constant power of 5 W is input to the MWS. At each HFS input power, line shapes were calculated for 1000 $\bar{\mathrm{H}}$ trajectories taking into account the spatial distributions of the $\bar{\mathrm{H}}$ beam and MW E-fields, and the averaged line shape is shown. The kinetic energy of the $\bar{\mathrm{H}}$ beam is set 6.10(5) keV, which is the value characterized in the $\bar{\mathrm{H}}$ production experiment in 2022 [44].

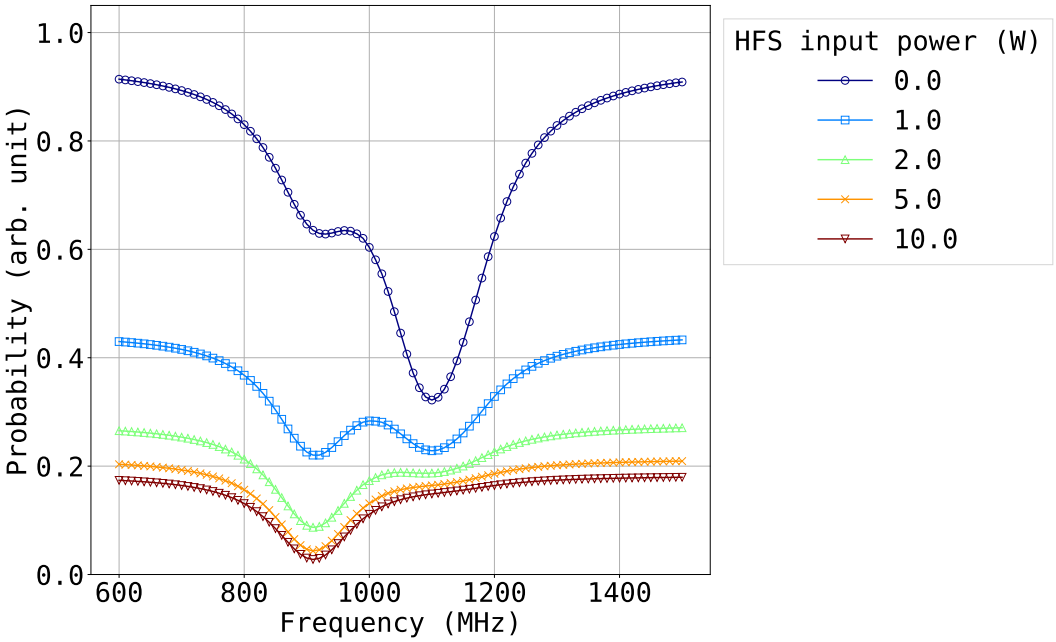

Figure 5.7: Simulated line shapes of the Lamb shift transition obtained with different total MW powers input to the HFS with a constant power of 5 W input to the MWS.

One can see that contributions from the $2S_{1/2}(F = 1)$ states are mostly removed at the HFS input power of 10 W, resulting in a spectrum with a single peak due to the $2S_{1/2}(F = 0)$ state.

Concerning the use of the HFS, it should also be noted that the event rate of Lyman-α photon detection is supposed to decrease at a higher MW power to input to the HFS, simply because the $2S$ state population decreases accordingly. As such, it would be helpful to perform an optimization of the HFS input power to solve the trade-off between measurement precision and time.

5.5 Geometrical Efficiency of Lyman-α Detector

A Monte Carlo simulation of the Lyman-α photon emission was performed to evaluate the geometrical efficiency of the Lyman-α detector, supposing the characteristics of the $\bar{\mathrm{H}}$ beam in 2022.

Figure 5.8 shows the simulated quenching efficiency (orange) and acceptance (blue) of the MCPs for the emitted Lyman-α photons. Each efficiency was calculated for different quenching voltages applied on the downstream electrode while the upstream electrode is kept grounded. Input MW powers for the HFS and MWS were both set 0 W in this simulation. At each voltage, 10,000 $\bar{\mathrm{H}}(2S)$ atoms were calculated, and the error bars are defined as a square-root of the count.

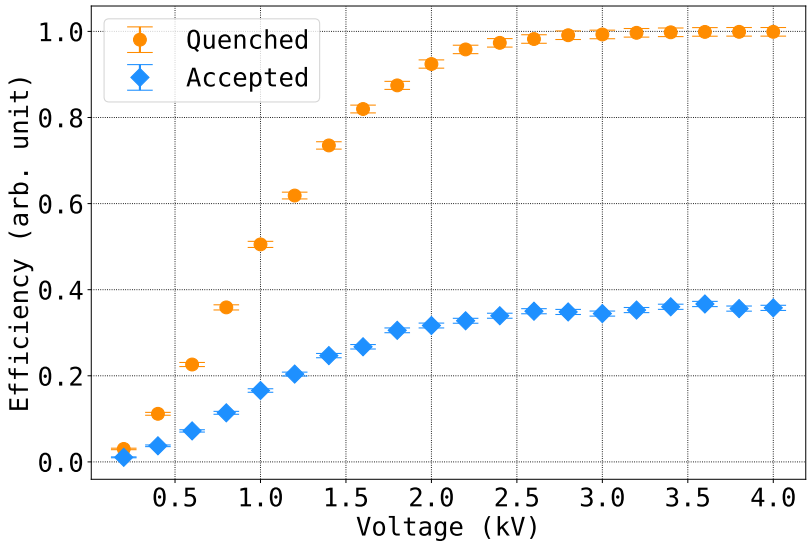

Figure 5.8: Quenching efficiency (orange circle) and acceptance (blue rectangle) of the MCPs for the emitted Lyman-α photons, simulated for different quenching voltages applied on the downstream electrode with the upstream electrode grounded.

One can see that most of the $\bar{\mathrm{H}}(2S)$ atoms are deexcited above 2.5 kV, and more than 30% of emitted Lyman-α photons are accepted by the MCPs.

In the experiments, a quenching scheme of applying 3 kV to the downstream electrode has been typically adopted, which forms the E-field shown in Figure 5.4(a). This configuration gives the acceptance of 34.5(5)% for the $\bar{\mathrm{H}}$ beam in 2022. Multiplying this acceptance and the detection efficiency of the CsI coated MCPs of 22(2)% [72, 79], the total detection efficiency in this configuration can be evaluated as 8(1)%.

For a comparison, the acceptance under the E-field configuration shown in Figure 5.4(b) was also computed. In this case, -1.5 kV and $+1.5$ kV are applied on the upstream and downstream electrode, respectively. The computed acceptance was 28.5(5)%, a little lower than that of the scheme to apply 3 kV to the downstream electrode. This is because a fraction of the incoming $\bar{\mathrm{H}}(2S)$ atoms are already quenched before reaching the center of the detector and having the largest solid angle for the emitted Lyman-α photons to hit the MCPs.

5.6 Line Shape Simulation Towards 10% Precision

Monte Carlo simulations of the line shape measurement were performed to predict periods of data-taking necessary to achieve certain spectroscopy precisions.

In the first line shape measurement, the HFS will not be used and a spectrum containing all possible transitions indicated in Figure 3.2 will be measured by using just the MWS, to demonstrate the measurement with a high event rate in the Lyman-α photon detection, aiming at a precision on the order of 10%.

In this simulation, a production rate of 0.1 $\bar{\mathrm{H}}$ atoms per AD cycle and the $2S_{1/2}$ state population of 15% [44, 45] are assumed. This production rate is being demonstrated in the $\bar{\mathrm{H}}$ production experiment in 2024 as described in Section 7.2. Assuming a few months of the data-taking with 110 seconds of the mixing cycle and 80% of the duty cycle of the AD/ELENA facility, a spectrum of the Lyman-α photon counts i.e. the Lamb shift line shape is expected to be obtained as shown in Figure 5.9. At each frequency, 300 $\bar{\mathrm{H}}$(2S)s were simulated, and a total MW power of 5 W was assumed to be input to the MWS.

To fit the spectrum contributed by all sublevels of the $2S_{1/2}$ state, i.e. $(F, m_F) = (0, 0)$, $(1, 0)$, and $(1, \pm 1)$, three Lorentzian functions are simply adopted. The resonance frequency of the 910 MHz transition was determined to a relative precision of 13% with the reduced χ^2 computed as 0.83. If experimentally demonstrated, this will be the comparable precision achieved in the precedent indirect measurement [35].

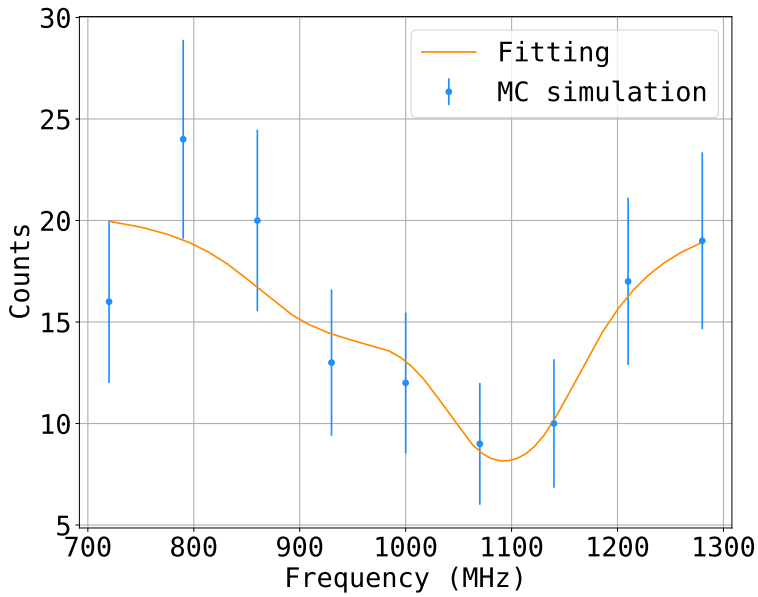

Figure 5.9: Monte Carlo simulation of the Lamb shift spectrum and a fitting curve to the spectrum, expected to be obtained in the first measurement.

5.7 Line Shape Simulation Towards 100 ppm Precision

To estimate the data-taking period and study some systematic uncertainties for achieving a precision on the order of 100 ppm, further Monte Carlo simulations were performed with much higher statistics.

Figure 5.10 shows one of the Lamb shift spectra obtained from such high statistic Monte Carlo simulations and a fitting curve to the spectrum. In this simulation, the production rate of 1500 $\bar{\mathrm{H}}(2S)$ atoms per AD cycle, as discussed in Section 2.6, and a few months of data-taking are supposed. At each frequency, 10^7 $\bar{\mathrm{H}}(2S)$s were simulated, with a total MW power of 10 W and 5 W assumed to be input to the HFS and MWS, respectively.

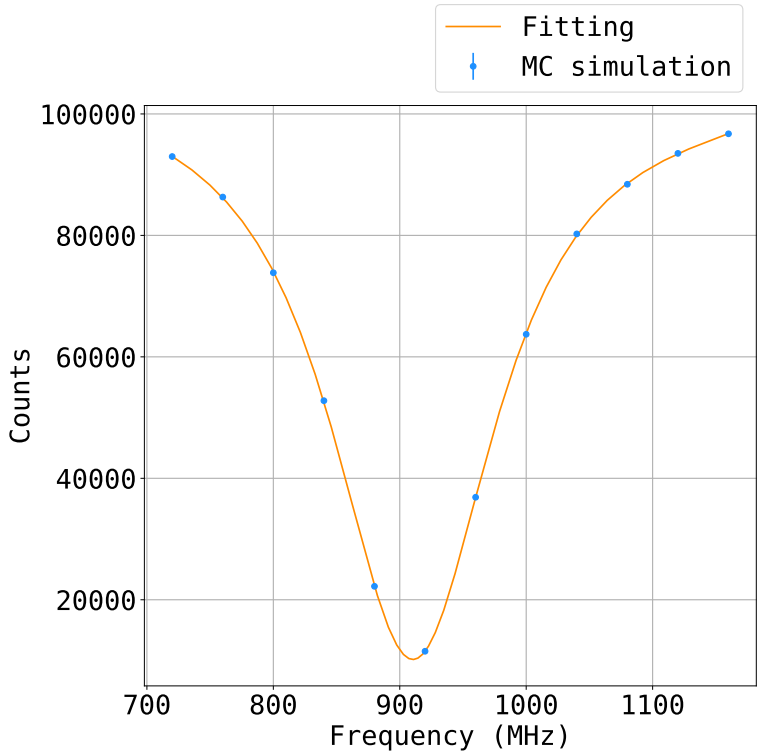

Figure 5.10: Monte Carlo simulation of the Lamb shift spectrum and a fitting curve to the spectrum, expected to be obtained in a high statistic measurement to reach a derivation of the antiproton charge radius.

The resonance frequency of the 910 MHz transition was determined to be 910.43(13) MHz with the reduced χ^2 computed as 1.29. This value is significantly off from 909.887 MHz, the correct resonance frequency given in the Hamiltonian (5.3). This discrepancy is due to Bloch-Siegert effect [92], a systematic shift of the resonance frequency observed generally in a two level system interacting with an oscillating field. This effect is caused by an anti-rotating term contained in the coupling term with the oscillating field, which is neglected in a derivation of the Lorentzian function by applying the rotating wave approximation. The shift is known to be approximately proportional to the applied power at a relatively lower power region.

In order to correct the Bloch-Siegert effect in our setup, the simulations were repeated for different MWS input powers, and a linear function was obtained by fitting the simula-

tion results, which represents the shift as a function of the power. At an input MWS power of 5 W, the shift was evaluated to be 0.60(5) MHz. Therefore, the resonance frequency can be corrected as follows:

$$909.83 \pm 0.13\,(\text{statistical}) \pm 0.05\,(\text{Bloch-Siegert shift})\ \text{MHz} \tag{5.19}$$

Taking into account both the statistical uncertainty and the uncertainty in determining the Bloch-Siegert shift, the relative precision was calculated to be 153 ppm. Towards an extraction of the antiproton charge radius, measurements at this level of precision will be targeted, along with the improvement of the $\bar{\text{H}}(2\text{S})$ production rate.

5.8 Conclusion

We developed a numerical calculation program to simulate the $\bar{\text{H}}$ Lamb shift spectroscopy, taking into account 3D spatial distributions of the $\bar{\text{H}}$ beam and the E-field formed by the HFS, MWS, and Lyman-α detector.

Using this program, it was confirmed that the $2S_{1/2}(F = 1)$ state can be almost completely removed and a clear single peak spectrum due to the $2S_{1/2}(F = 0)$ state can be obtained at a total input power of 10 W for the HFS and 5 W for the MWS.

Also, the Lyman-α detector's efficiency was evaluated to confirm that the total detection efficiency of 8(1)% can be obtained by applying 3 kV on the downstream ring electrode with the upstream electrode grounded.

Furthermore, we estimated that a few month of the data-taking would achieve 10% spectroscopy precision in the first line shape measurement to be performed without the HFS, and a precision on the order of 100 ppm in the high-precision measurement to be performed with both the MWS and HFS. In the simulation for the first line shape measurement, the $\bar{\text{H}}$ production rate of 0.1 $\bar{\text{H}}$ atoms per AD cycle was assumed. As described in Chapter 7.2, this production rate is being demonstrated in the beam time of 2024.

Chapter 6

Commissioning of Lyman-α detector

In this chapter, some commissioning experiments of the Lyman-α detector are described. For characterizing the Lyman-α photon signal, UV photon measurements were performed by using a light emitting diode (LED) source. Also, the Lamb shift spectroscopy using an atomic beam of H was conducted in order to test the triggered operation of the entire spectroscopy setup and check the performance of the Lyman-α photon detector. Furthermore, background measurements for the $\bar{\mathrm{H}}$ Lamb shift spectroscopy were attempted by using the trap-extracted $\bar{p}$ beam, to characterize the background signal rate and investigate sources of the background in comparison with Monte Carlo simulations.

6.1 UV Photon Measurement

In order to characterize the pulse height of the signals due to the Lyman-α photons, a UV LED source was installed in the MW vacuum chamber. This can also be used to monitor the detection efficiency of the CsI-coated MCPs in the Lyman-α detector possibly changing over time.

Figure 6.1(a) shows the photograph of the UV source, which comprises four AlGaN LEDs (VISHAY VLMU35CR40-275-120) attached to a copper gasket. This specific LED is a high power application and normally used for a sterilization purpose. The gasket is mounted on the downstream side of the outer box of the MWS. Figure 6.1(b) shows how it looks from the top flange of the MW vacuum chamber after installation. The power for each LED is supplied from the feedthrough on the top flange. Each LED is typically operated at an input voltage of around 5 V.

The UV photons are emitted downstream in the $\bar{p}/\bar{\mathrm{H}}$ beam line, and each MCP of the Lyman-α detector can be seen directly from the UV source. The wavelength of the photon is around 270 nm, while the wavelength of the Lyman-α photons is 122 nm. Quantum efficiency of CsI for the 270 nm UV photon could be negligible, considering the band gap of 6.3 eV and the electron affinity of 0.1 eV, which gives a threshold wavelength of 194 nm as mentioned in Reference [80]. Therefore, in the context of monitoring the detection efficiency of the Lyman-α detector, it should be noted that the signal seen in this measurement would not necessarily be produced by the photoelectric effect in CsI, and thus may not accurately reflect the status of the CsI coating.

Also, in the context of characterizing the Lyman-α photon signals, it should be emphasized that the kinetic energy of photoelectrons produced by the 270 nm UV source and the 122 nm Lyman-α photon can differ, possibly resulting in signals with different

(a) (b)

Figure 6.1: Photographs of (a) the UV LED source and (b) how it looks from the top flange of the MW vacuum chamber after installation.

characteristics. However, given that both signals are attributed to the single photoelectron produced on the front surface of the MCPs, the UV photon measurements could still provide valuable information for characterizing the Lyman-α photon signals.

6.1.1 UV Photon Detection

The Lyman-α detector demonstrated the detection of the 270 nm UV photons. In the UV photon measurements, the oscilloscope runs in the auto-trigger mode, and records the waveforms for 1 ms, with a dynamic range limited down to around -150 mV. All the other settings are the same as described in Section 3.5.3.

Figrue 6.2(a) shows waveforms from each channel of the Lyman-α detector and detected peaks represented in the purple crosses, which indicate the UV photon signals. For the operation of the MCPs, the back-positive scheme was adopted, and -50 V and 1950 V were applied to the front and back side of each MCP, respectively. In these particular waveforms, 622, 810, 522, and 981 peaks were detected in each channel 1, 2, 3, and 4 respectively, during the data-taking for 1 ms.

Figrue 6.2(b) shows a close-up view of Figrue 6.2(a) in the arbitrary time range for 10 μs to visualize the peaks clearly. The noise level i.e. pedestal of the waveform, is around 0.5(5) mV for each channel. The peaks are detected by using scipy.signal.find_peaks [90] if the pulse height is lower than a certain threshold represented by the horizontal dotted line, which is set -5 mV all for each channel. It was found that the pulse tends to contain an afterpulse or so-called ringing. The ringing peaks are not detected by masking the waveform for a few tens of nanoseconds from the main prompt peak.

The detection efficiency of the MCPs for the 270 nm UV photons can roughly be estimated as follows. The total current and power read at the power supply for the UV source are typically 20 mA and 100 mW. The external quantum efficiency is reported to be around 5% for 270 nm range UV source which adopts AlGaN LED tip [93] Therefore, the power consumed for emitting the UV photons is roughly evaluated to be 5 mW. Dividing this value by the energy of 270 nm UV photon, one can estimate the UV photon flux to be 7×10^{15} per second. Given the recording time of 1 ms, and supposing the total

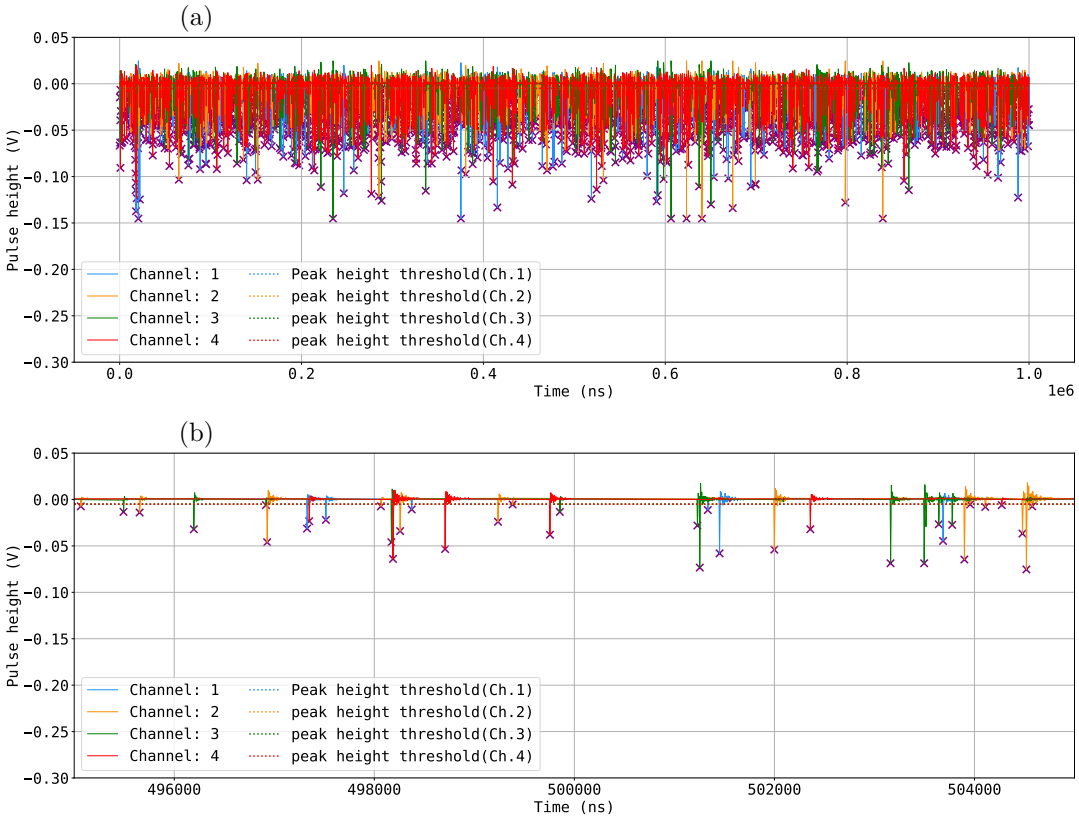

Figure 6.2: (a) Waveforms from each MCP channel of the Lyman-α detector and detected peaks of the UV photons when -50 V and 1950 V were applied to the front and back side of each MCP respectively, and (b) a close-up view in the arbitrary time range for 10 μs.

solid angle of the MCPs to be on the order of 1%, which takes into account the radiation angle distribution described in the data sheet of the LED, one could approximate that the photons on the order of 10^{10} should hit MCPs per measurement. The measured count By dividing the measured total peak count of about 3000 by the expected hit count of 10^{10}, the detection efficiency for the 270 nm photon is evaluated to be on the order of 10^{-7}. Concerning single stack MCP, the detection efficiency was reported to be 10^{-9} for 260 nm UV photon [78].

6.1.2 Peaks from Different MCP Bias Scheme

The data-taking was repeated a couple of tens of times to accumulate the statistics, and the same dataset was taken for other MCP bias voltages as well, to compare the peak count rate or the pulse height spectra.

Figure 6.3 shows histograms of the pulse height spectra of the peaks detected at each channel of the MCP, with the front side of the MCP applied on -50 V, 0 V, 50 V, and with the back side applied on 1950 V, 2000 V, 2050 V respectively, thus keeping the potential difference 2000 V. The histograms are normalized by the number of repetition of the data-taking for each MCP bias voltage. The peak count is noted in the legend of the plot for each MCP bias voltage.

The peak count increases as a higher bias voltage is applied to the front side of the MCP even with the constant potential difference of 2000 V. For example at channel 1, the

counts are 573.25, 691.65, and 746.45 for the front bias voltage of $-50\,\mathrm{V}$, $0\,\mathrm{V}$, and $50\,\mathrm{V}$, respectively. This suggests that the efficiency of collecting the photoelectrons improves at a higher front bias voltage, as expected. However, in Figure 6.3, one can observe that the shape of the pulse height spectrum changes at each channel in a way that the higher pulse height region is more pronounced at a higher front bias voltage. This indicates that at a higher front bias voltage, the MCP tends to collect free electrons that were initially far from the MCP but attracted by the positive front bias and subsequently detected. Such electrons can produce higher pulses than the photoelectrons due to the additional acceleration, on top of the original gain of the MCP. Therefore, it is possible that the MCPs are simply more susceptible to noise at a higher positive front bias voltage.

Furthermore, it should be pointed out that each histogram has a peak from $20\,\mathrm{mV}$ to $40\,\mathrm{mV}$, except the first prompt peak. For example the front bias voltage of $-50\,\mathrm{V}$, the peaks of the histograms can be found around $38\,\mathrm{mV}$, $30\,\mathrm{mV}$, $34\,\mathrm{mV}$, and $40\,\mathrm{mV}$ at channel 1, 2, 3, and 4, respectively. These values have been used to determine thresholds for signal selections in data analysis of the Lamb shift spectroscopy using an atomic beam of H which is described in Section 6.2.

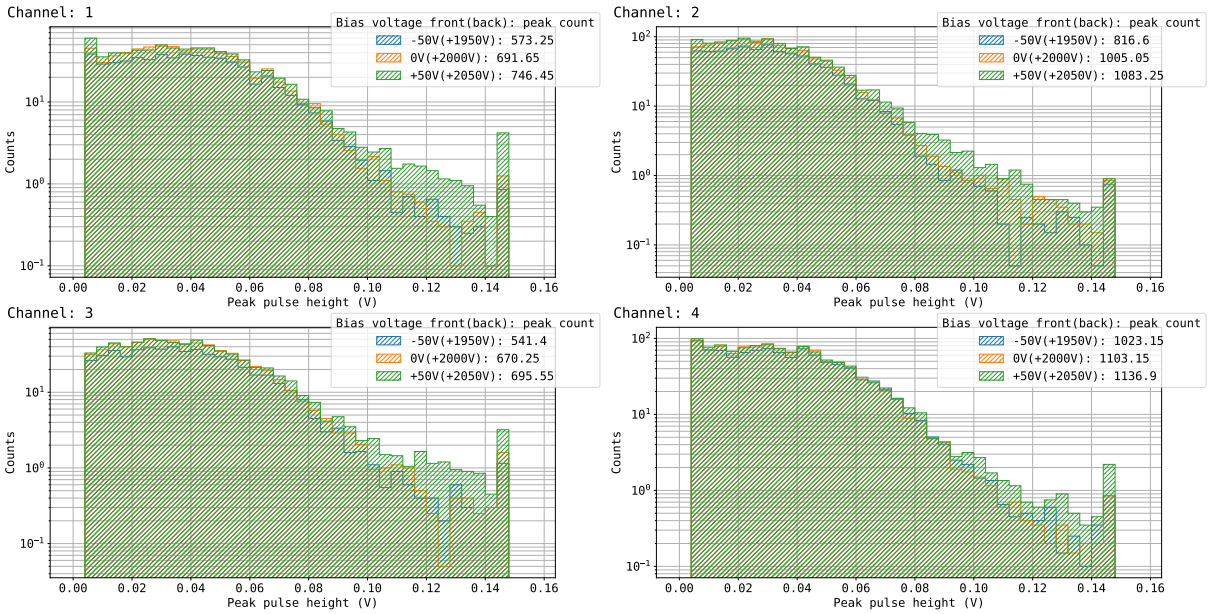

Figure 6.3: Pulse height spectra of the peaks detected at each channel of the MCP in the UV photon measurements, with the front side of the MCP applied on $-50\,\mathrm{V}$, $0\,\mathrm{V}$, $50\,\mathrm{V}$, and with the back side applied on $1950\,\mathrm{V}$, $2000\,\mathrm{V}$, $2050\,\mathrm{V}$ respectively, to keep the potential difference $2000\,\mathrm{V}$.

A similar dataset was taken in the front-negative scheme as well. Figure 6.4 shows histograms of the pulse height spectra of the peaks detected at each channel of the MCP, with the front side of the MCP applied on $-2000\,\mathrm{V}$, $-2100\,\mathrm{V}$, $-2200\,\mathrm{V}$, and with the back side grounded.

In this case, the potential difference i.e. the gain of the MCP is explicitly increased. As a result, the count rate increases, and the spectrum shows a more pronounced higher tail, as a higher gain is applied.

It should also be noted that the peak of the histogram itself might look less clear in each plot than in those of Figure 6.3. This implies that a determination of the threshold in the peak height to effectively select the Lyman-α photon signal would require some more quantitative discussion than the case of the back-positive scheme.

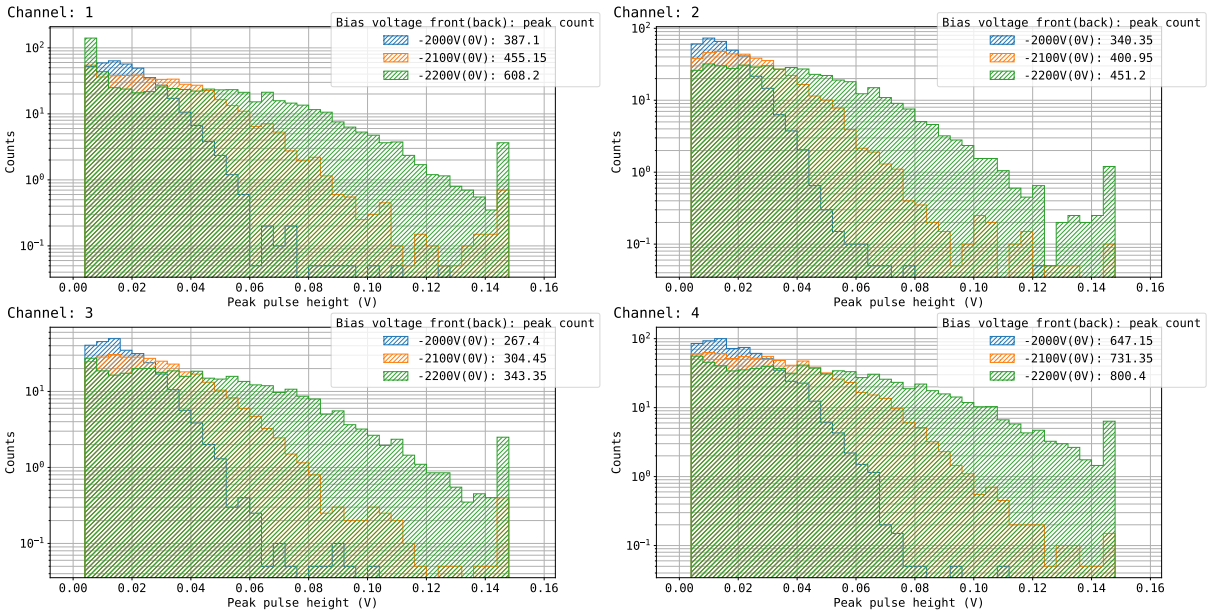

Figure 6.4: Pulse height spectra of the peaks detected at each channel of the MCP in the UV photon measurements, with the front side of the MCP applied on $-2000\,\mathrm{V}$, $-2100\,\mathrm{V}$, $-2200\,\mathrm{V}$, and with the back side grounded.

6.2 Pilot Measurement Using H^- Beam & C-foil

Towards the $\bar{H}$ Lamb shift spectroscopy, the Lamb shift spectroscopy of H atoms have been attempted using the H^- ion beam provided by the ELENA [26] facility and a thin carbon foil (C-foil). There are mainly two objectives in this experiment.

First objective of the H^- & C-foil experiment is to test the triggered operation of the entire spectroscopy setup. The $\bar{H}$ atoms provided as a pulsed beam requires a triggered operation of the spectroscopy setup and the data acquisition (DAQ) system, and some experimental parameters such as the MW frequency or power need be controlled shot-by-shot. This can be tested using the pulsed beam of H atoms produced from the pulsed H^- beam provided by the ELENA.

Second objective of the H^- & C-foil experiment is to optimize the experimental parameters for the $\bar{H}$ Lamb shift spectroscopy. Compared with the Lamb shift spectroscopy on H atoms, the Lyman-α photon count rate will be much low in our experiment. In the first phase of the experiment aiming at a spectroscopy precision of 10%, the event rate is expected to be on the order of 0.001 per AD cycle. To perform the experiment in a realistic period of time, the experimental parameters need to be optimized as much as possible in advance. Such parameters include the MCP bias voltages or quenching electrode voltages of the Lyman-α detector, as well as the MW frequency scan points or the power. In the H Lamb shift measurement, the theoretical Lyman-α photon count rate is much higher than in the $\bar{H}$ experiment. Therefore, one should be able to effectively work on a part of the optimization studies.

6.2.1 Production of H Beam

To produce the atomic beam of H, a beam foil technique is adopted by using the the H^- beam and a thin C-foil. ELENA is capable of providing a pulsed beam of H^- ions with almost the same level of intensity, spatial and time structure, as those of the $\bar{p}$ beam, at a repetition cycle of 15 seconds. The H^- beam is normally utilized for tuning steering parameters for the $\bar{p}$ beam. The H^- beam is first slowed down by the drift tube decelerator to 6 keV, then passed through the $\bar{p}$ trap and transported to the reaction chamber.

Figure 6.5 illustrates the setup of the H^- & C-foil experiment, and Figure 6.6 shows a photograph of the C-foil. In the reaction chamber, the decelerated H^- beam is injected onto the C-foil attached at the movable target holder in the reaction chamber as illustrated in Figure 2.4. The C-foil was produced by Arizona Carbon Foil, and has a thickness of a few nm, and an area of 14 mm × 9 mm.

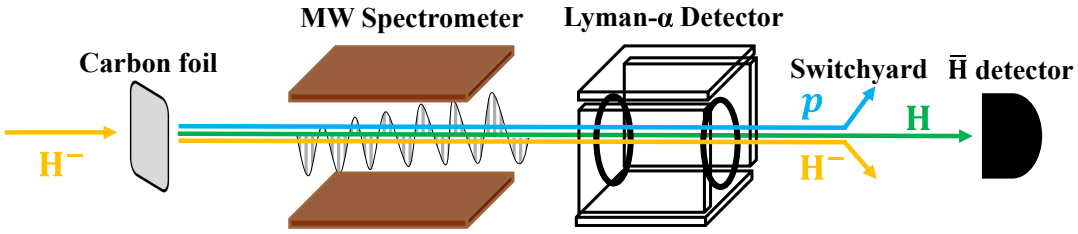

Figure 6.5: Setup of the H^- & C-foil experiment.

Inside the C-foil, the H^- ions are expected to experience two ionization processes. One process is the positive ionization to become protons by getting the orbiting electrons ripped off. The other process is the negative ionization to become H atoms or even H^-

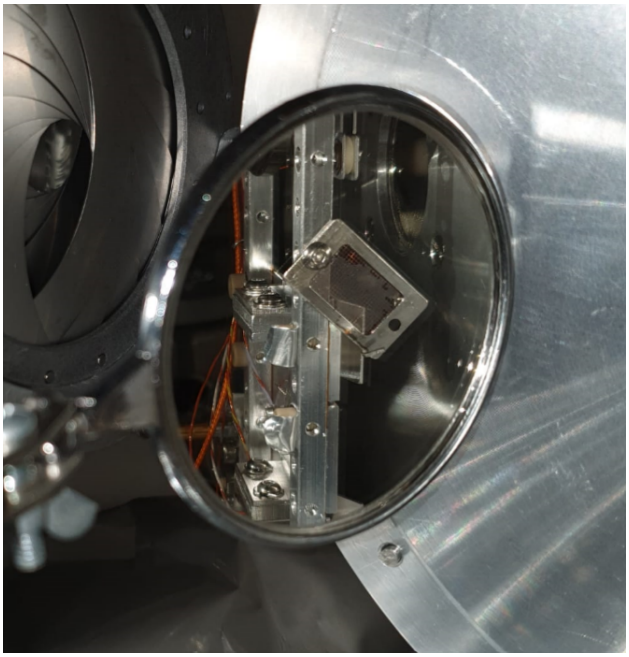

Figure 6.6: Photograph of the C-foil installed in the reaction chamber.

ions, by capturing free electrons in the conductive band of the foil. Depending on which charge state the particle is in when exiting from the foil, the production ratio of the H atoms is determined.

In some beam foil experiments using a low-energy proton beam and a few nm thick C-foil [94,95], the production ratios of H atom, proton, and H^- were measured to be about 80%, 15%, and 5% respectively, at an incident kinetic energy of the proton of 6 keV. One could assume the same production ratios in our experiment too, but should still note that it is a H^- beam, not a proton beam, that is injected onto the C-foil in our experiment.

In addition to the ionization processes, the particles also experience scattering with electrons or nuclei inside the C-foil, and exit from the foil with some angle spread, as well as kinetic energy spread. After the C-foil, a part of the particles passes through the MW spectrometer and the Lyman-α detector. A further fraction of the particles can make it to the switchyard, where only the H atoms are selected and then detected at the $\bar{H}$ detector.

6.2.2 Intensity of H($2S$)

The intensity of the $2S_{1/2}$ state H atoms passing through the Lyman-α detector can be evaluated from measurements and simulations. For the total number of H atoms arriving at the $\bar{H}$ detector, one can count the number of pixel clusters detected by the $\bar{H}$ detector. Figure 6.7 shows a typical image from the CCD camera of the $\bar{H}$ detector obtained in the H^- & C-foil experiment. The image shows pixel clusters made by neutral atoms hitting on the detector, which are bounded by the red rectangles. On average, about 1000 clusters are detected per ELENA cycle, depending on the beam steering condition.

The detection efficiency of a Chevron type MCP, for some neutral atoms, is known to converge to the channel open area ratio, as the kinetic energy is increased up to 5 keV [96]. This predicts that almost 2000 H atoms arrive at the $\bar{H}$ detector per ELENA cycle, given the 55% open area ratio of the MCP of, and the kinetic energy of the H atoms of about 5 keV which is discussed in the following paragraphs.

In order to estimate the number of H atoms passing through the Lyman-α detector,

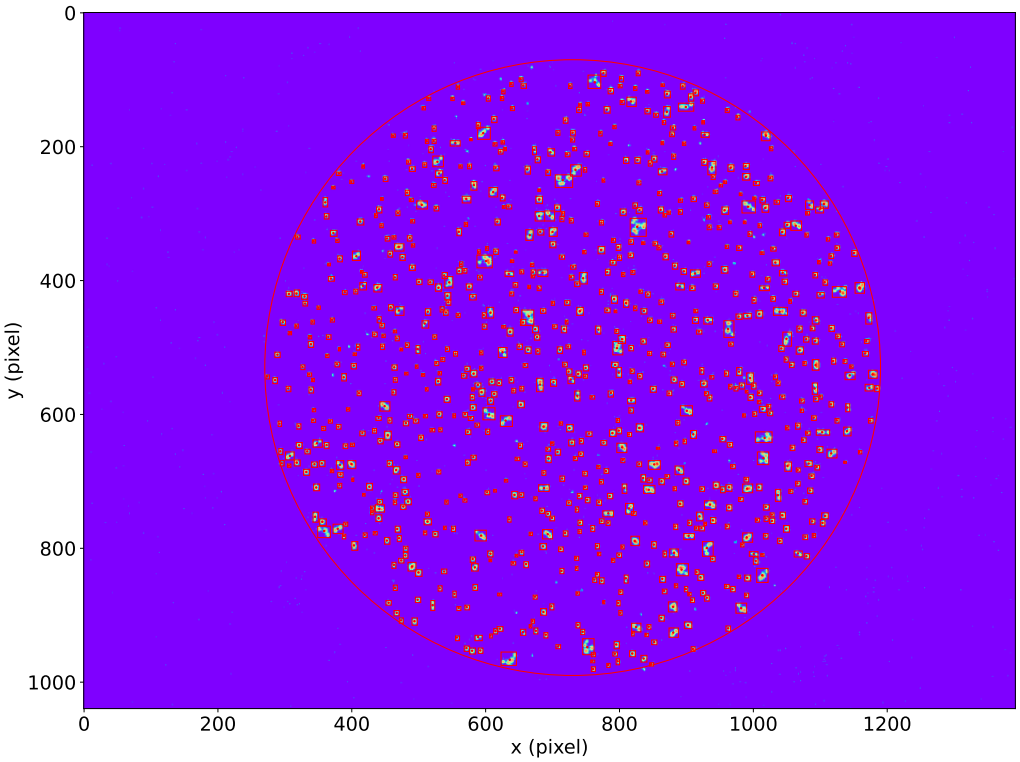

Figure 6.7: Image from the CCD camera of the $\bar{H}$ detector obtained in the H^- & C-foil experiment

trajectories of the H atoms were simulated by using SRIM2013 code [97]. First, to define the thickness of the carbon layer used in the simulation, a measured kinetic energy of particles after interacting with the C-foil and simulated kinetic energies under different thicknesses of the carbon layer were compared.

Figure 6.8 shows waveforms from the $\bar{H}$ detector representing the time-of-flight (TOF) spectra, and Gaussian fit curves to the spectra. The waveforms and fit curves are shown for both the case when the C-foil was positioned on the beam axis, and when it was removed. By comparing the center of the fit curve in each case, the mean value of the kinetic energy of the particles after interacting with the C-foil is evaluated to be 5.2 keV.

On the simulation side, first, scattering angles of protons with an incident kinetic energy of 6 keV were calculated for different thicknesses of the carbon layer. Figure 6.9(a) shows scattering angle spectra, for the layer thicknesses of 1 nm, 5 nm, 10 nm, and 20 nm. In this simulation, the protons were injected as a pencil beam vertically onto the layer. Among all the simulated protons, only the protons with a scattering angle small enough to hit the $\bar{H}$ detector (less than 0.65°) are selected. For the selected protons, kinetic energy spectra are shown in Figure 6.9(b). The mean kinetic energy of around 5.2 keV can be found for the thickness of 10 nm. Therefore, the thickness of the C-foil can roughly be evaluated as 10 nm.

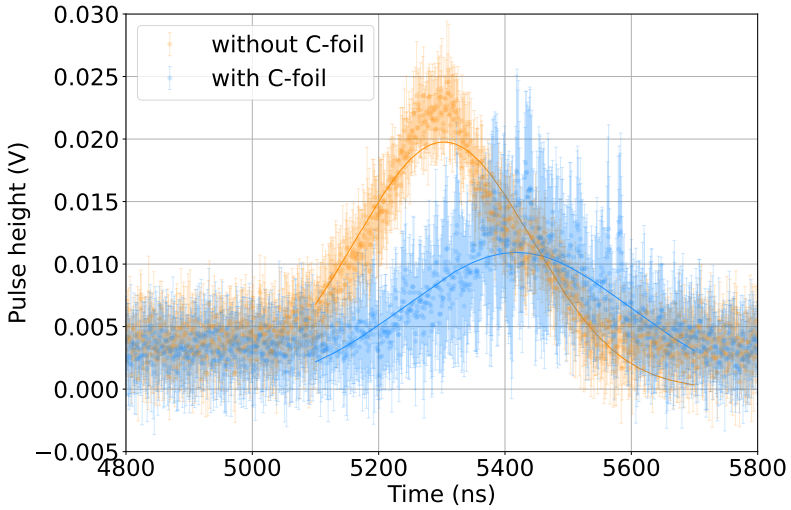

Figure 6.8: Waveform from the MCP of the $\bar{H}$ detector showing the TOF spectrum of the H atoms with (blue) and without (orange) the C-foil.

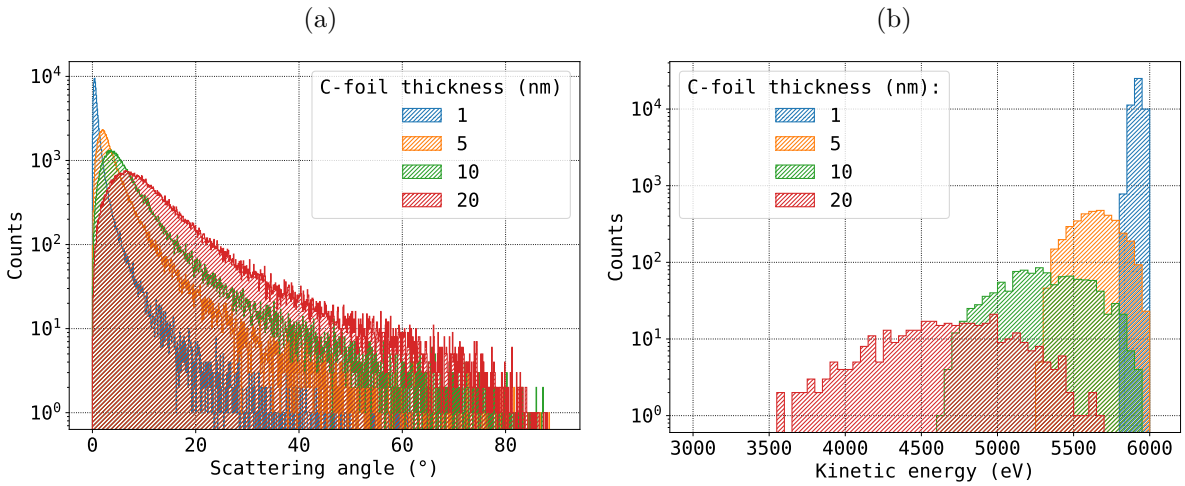

Figure 6.9: Simulated spectra of (a) scattering angle and (b) Kinetic energy of protons injected on the carbon layer at 6 keV, for different thicknesses of the layer. The kinetic energy spectra are shown only for the protons having scattering angle small enough to hit the $\bar{H}$ detector.

By using momentum vectors of protons simulated under the carbon layer thickness of 10 nm, trajectories of the protons are reconstructed over the entire region of the spectroscopy setup, as shown in Figure 6.10. The trajectories are shown for 1000 protons, and the color of the trajectory represents the kinetic energy of each proton. Ratios of the protons passing through each component of the setup are denoted in the figure, which are 83.5(9)%, 3.6(2)%, 3.5(2)%, and 2.3(2)% for the electrostatic steerer, MW spectrometer, Lyman-α detector, and $\bar{H}$ detector, respectively.

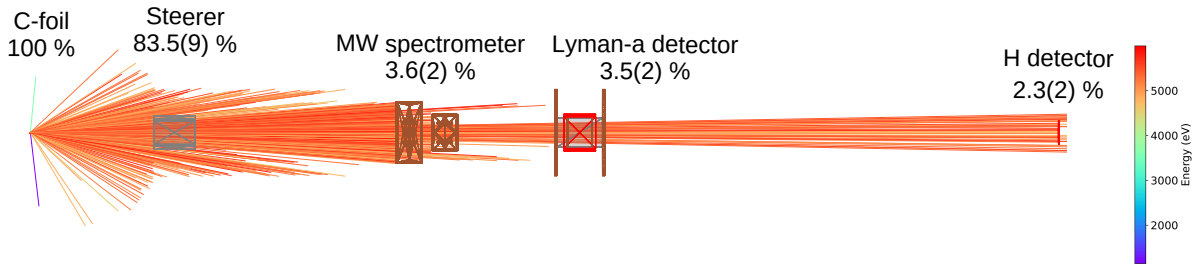

Figure 6.10: Trajectories of the protons over the entire region of the spectroscopy setup, reconstructed from the momentum vectors of protons simulated under the carbon layer thickness of 10 nm.

This beam transmission efficiency predicts that approximately 3000 H atoms pass through the Lyman-α detector per ELENA cycle, given the measured number of H atoms at the $\bar{H}$ detector of around 2000.

Out of the 3000 H atoms, one could expect around 160 H atoms to be in the $2S$ state, according to the $2S$ state population ratio of 0.054 mentioned as a rule of thub in Reference [79]. However, it should be noted that the estimation performed here is quite rough, and would merely give a lower limit taking into account the fact that a few pixel clusters are not detected in Figure 6.7.

6.2.3 Attempt of Lyman-α Photon Detection

In the H^- & C-foil experiment, a triggered operation of the entire experimental setup was confirmed. For the DAQ, the read-out oscilloscope of the Lyman-α detector is operated in an external triggered mode. From the ELENA facility, a TTL signal is distributed 1 ms before the beam extraction. This signal is delayed by a fewsby a delay generator, so that the time-zero of the waveform is adjusted at a fewsbefore the arrival time of the beam. Then, the oscilloscope starts recording the waveforms with the configuration described in Section 3.5.3 for 10 μs.

Figure 6.11 shows waveforms from each MCP channel obtained from one ELENA cycle and detected peaks. The back-positive MCP bias scheme, described in Section 3.5.2(b) was adopted here, with the front and back side of each MCP applied on -50 V and 1950 V, respectively i.e. the same setting as that used for taking the waveforms in Figure 6.2. Only the peaks within an expected time window, represented by the two vertical black solid lines, are detected and shown as the purple crosses. One can see that a couple of peaks are detected within the time window in each channel.

For this shot, the MWS was operated at a frequency of 1060 MHz, which is the mean frequency of the resonance frequencies of the 910 MHz transition, two 1088 MHz transitions, and 1147 MHz transition described in Figure 3.2(a). Thus, contributions of the Lyman-α photon from the H(2S) atoms are suppressed, since a majority of the H(2S) must have been de-excited to the ground state via the Lamb shift transition at the MW spectrometer. Therefore, most of the peaks seen in Figure 6.11 are considered to be background signals due to scattered ions or electrons.

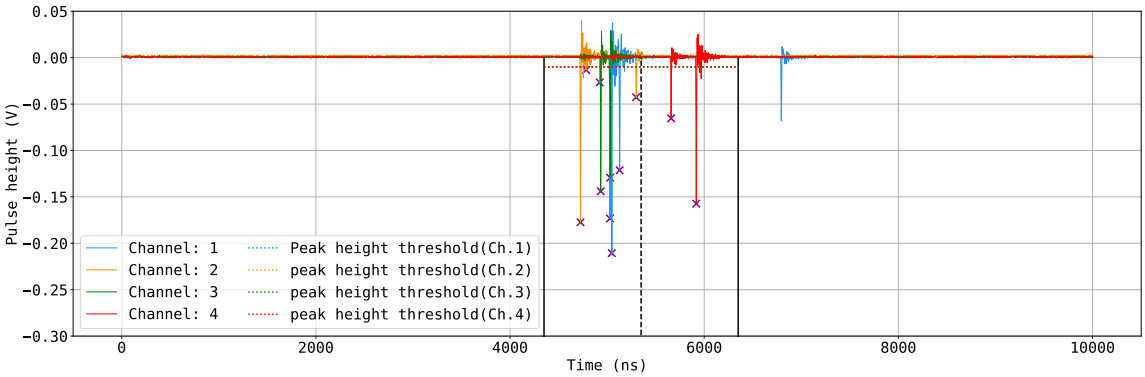

Figure 6.11: Waveforms from each MCP channel of the Lyman-α detector obtained from one ELENA cycle, and detected peaks.

The data-taking was repeated to accumulate statistics of the peak signals, for both case of the MW frequency set on-resonance i.e. 1060 MHz, and off-resonance e.g. 600 MHz. Figure 6.12 shows a time series plot of the peak counts in the on-resonance (blue) and off-resonance (orange) mode respectively, with error bars defined as the square-root of the counts. The data was taken for about 30 minutes alternately for each mode, in order to be less subject to time-dependent systematice effects. The H^- beam sometimes fails to get extracted from the ELENA, which results in, for example in this figure, the empty region from 20 to 21 o'clock.

Using this dataset, Histograms of the peak counts are made and shown in Figure 6.13 for both the off-resonance mode (orange) and on-resonance mode (blue). The mean value and standard deviation of the counts are 11.01 and 4.18 for the off-resonance mode, and

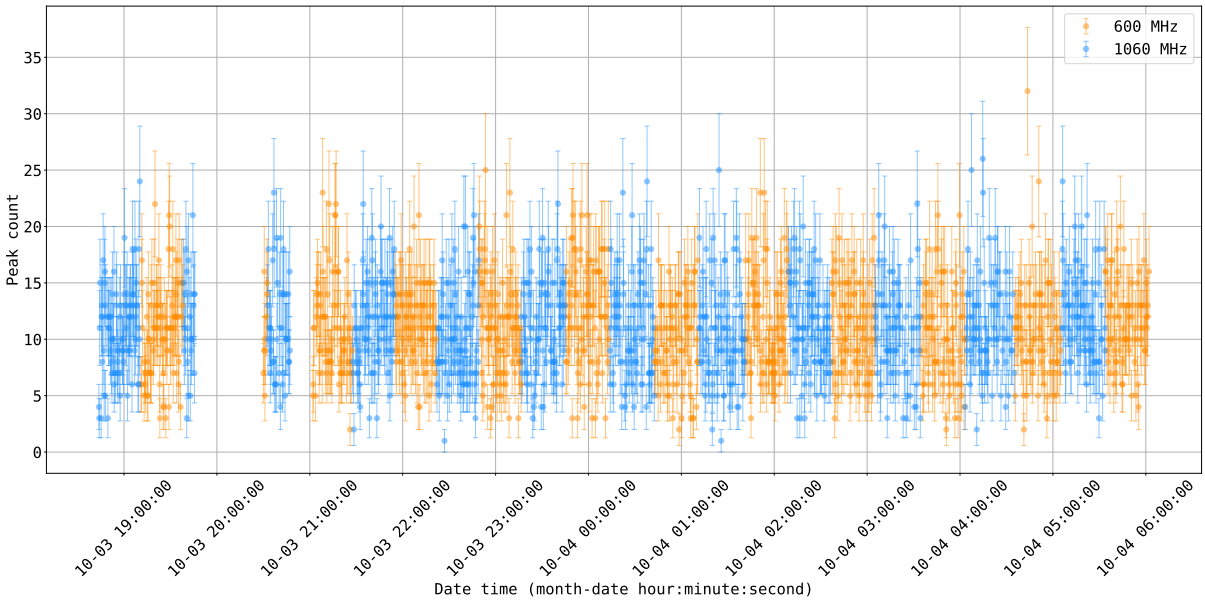

Figure 6.12: Time series plot of the peak counts in the on-resonance (blue) and off-resonance (orange) mode respectively, with error bars defined as the square-root of the counts.

11.05 and 4.21 for the on-resonance mode, respectively.

The number of the H(2S) atoms passing through the Lyman-α detector per ELENA cycle is evaluated in Section 6.2.2 to be at least around 160. For the H beam, the de-excitation efficiency by the MWS field and the total detection efficiency of the Lyman-α detector are evaluated to be around 60% and 10%, respectively, by using the simulation described in Chapter 5. Taking these values into account, the mean value of the peak count in the off-resonance mode is predicted to be higher than that in the on-resonance mode by around 10, which is clearly not the case in this dataset. A hypothesis test predicts a significance of 0.02 σ when normalizing the counts by both the number of shot and the intensity of the H^- beam per shot, assuming two independent Poisson distribution for the peak count rate in the on-resonance mode and off-resonance mode.

Besides this dataset, a several more datasets were taken, by switching the MW power on and off instead of the frequency on-resonance and off-resonance, or by adopting different MCP bias voltages. Also, selections of the peaks were performed by setting pulse height thresholds based on the pulse height spectra discussed in Section 6.1.2. However, we could not clearly see a reproducible excess of the Lyman-α photon counts in the off-resonance mode.

Given this result, one thing that has been suspected is a degradation of the detection efficiency of the Lyman-α detector. CsI coated on the MCP is a hygroscopic material, and the photoelectric conversion efficiency can decrease due to absorption of water molecules [80]. Since the last H Lamb shift spectroscopy in the GBAR experiment in 2021 which demonstrated the line shape measurement, there have been some vacuum incidents in the beam line, and the Lyman-α detector was exposed to an air pressure of up to 10^{-3} mbar a couple of times. These accidents could have deteriorated the photoelectric conversion efficiency of CsI.

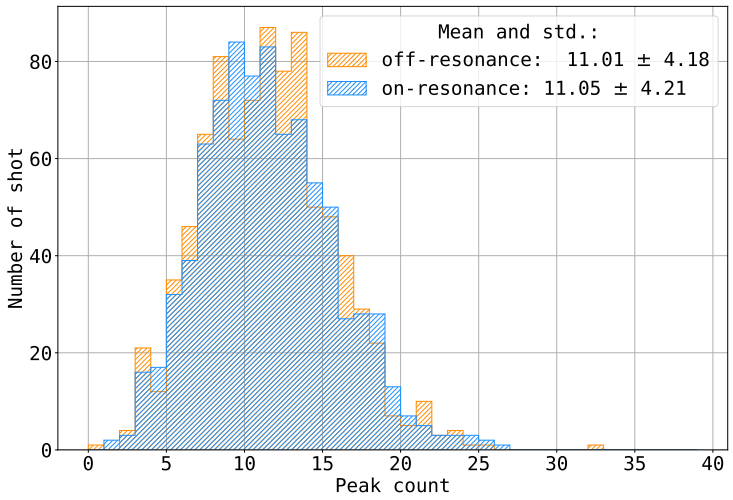

Figure 6.13: Histograms of the peak counts for both the off-resonance mode (orange) and on-resonance mode (blue).

6.3 $\bar{p}$ Background Measurement

Though the Lyman-α photon signals were not detected in the H^- & C-foil experiment, background signals were certainly detected as seen in Figure 6.11, which are assumed to be mainly due to protons, H atoms, or H^- ions hitting the MCPs. As such, during the beam time in 2024, background measurements of the Lyman-α detector were carried out by using the $\bar{p}$ beam extracted from the $\bar{p}$ trap for the first time.

Such background measurements are essential for the following reasons. When an $\bar{p}$ hits a material at a kinetic energy of 6 keV, it loses its kinetic energy and eventually annihilates with a proton or neutron of a nucleus inside the material, and produces about three charged pions ($\pi^{\pm}$s) and two neutral pions (π^0s) on average, depending on the nuclide of the nucleus of the annihilation target. A majority of the π^0s immediately decay to γ-rays, which can then produce $e^{\pm}$s by the pair creation process inside materials. Most of these charged particles are the minimum ionizing particles. On top of that, these high-energy secondary particles can produce further particles through interactions with the surrounding material in principle. Therefore, characterization of the background rate is important to realistically evaluate the data-taking period to achieve the Lamb shift spectroscopy at a certain precision. Also, understanding the background particle type and its process of origin and so on will be a key for upgrading the spectroscopy setup to improve the signal over noise ratio.

6.3.1 Setup and Characteristics of $\bar{p}$ Beam

Figure 6.14 illustrates the setup of the background measurement. The $\bar{p}$ beam extracted from the $\bar{p}$ trap is injected to the Ps cavity target, and passed through the MW spectrometer and Lyman-α detector, then transported to the $\bar{H}$ detector.

Depending on the beam profile i.e. spatial divergence of the trap-extracted $\bar{p}$ beam, a substantial amount of the background can emerge from the $\bar{p}$ annihilation at the entrance of the Ps cavity target or at the collimator behind the reaction target. The cavity target has a rectangle opening of 2 mm × 1.5 mm as illustrated in Figure 2.3 in Section 2.4, and

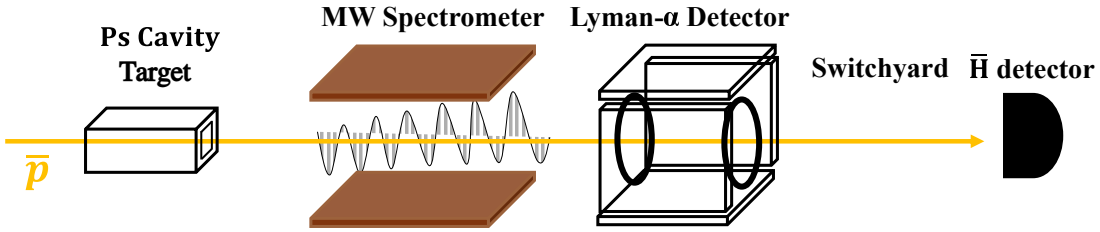

Figure 6.14: Setup of the $\bar{p}$ background measurement.

the collimator has a diameter of 5 mm as illustrated in Figure 7.2 in Section 7.1.

In order to diagnose the $\bar{p}$ beam profile at the target region, a MCP is installed at the exit of the reaction chamber, and images can be obtained by a phosphor screen and CCD camera. Figure 6.15 shows images of the $\bar{p}$ beam profile taken from this MCP (a) when the $\bar{p}$ beam passes through the free space i.e. the reaction region without the target nor the collimator, as illustrated in Figure 2.4, and (b) when the $\bar{p}$ beam passes through the cavity target and the collimator. The circumference of the MCP is represented by the circle, and the beam center is represented by the cross.

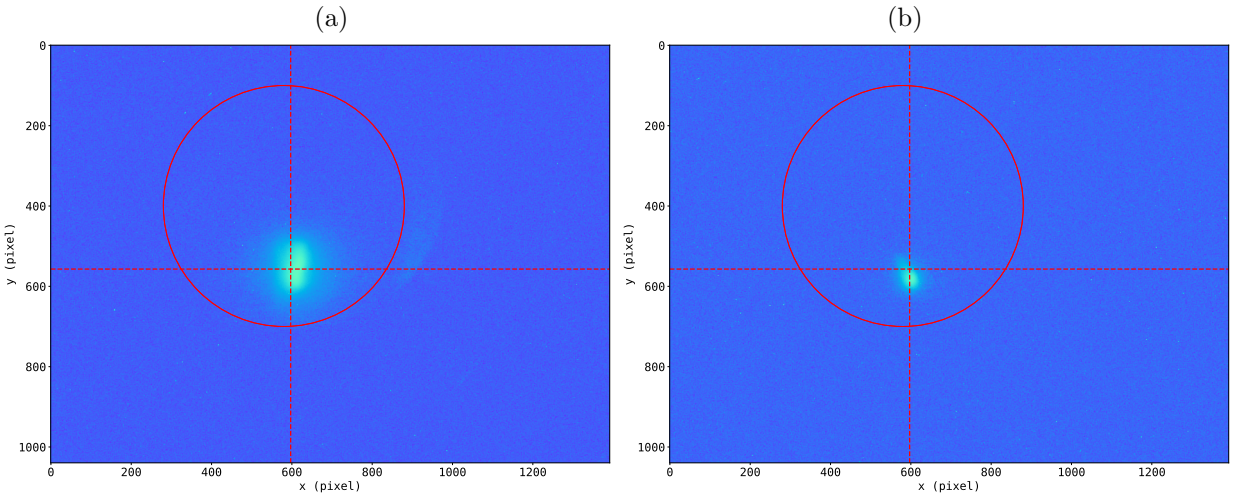

Figure 6.15: Images of the $\bar{p}$ beam profile taken from the MCP in the reaction chamber (a) when the $\bar{p}$ beam passes through the free space, and (b) when the $\bar{p}$ beam passes through the cavity target and the collimator.

One can see that the $\bar{p}$ beam profile is smaller in Figure 6.15(b) than in (a). Thus, the beam is clipped by the cavity target or collimator, which indicates $\bar{p}$ annihilation on the surface of these materials.

From this MCP in the reaction chamber, waveforms can also be obtained to study the bunch length of the beam. Figure 6.16 shows waveforms from the MCP (a) when the $\bar{p}$ beam passes through the free space and (b) when the $\bar{p}$ beam passes through the cavity target and the collimator. A few waveforms are shown in both cases. The waveforms overlap very precisely, which indicates reproducibility of the TOF spectra. In each case, one can see that the TOF spectra have characteristic multiple peaks, which are considered due to bunching at the extraction from the $\bar{p}$ trap, and contain long after tails. The FWHM of the spectra are roughly 150 ns in each case.

Another thing to note in the waveforms is that with the cavity target, the pulse height decreases to almost 20% of that in the case of free space. Supposing that the beam intensity is more or less proportional to the pulse height, this indicates that 80% of the beam could be lost at the entrance of the cavity target or at the collimator, and the remaining 20%, which corresponds to 10^6 $\bar{p}$s, pass through the cavity target.

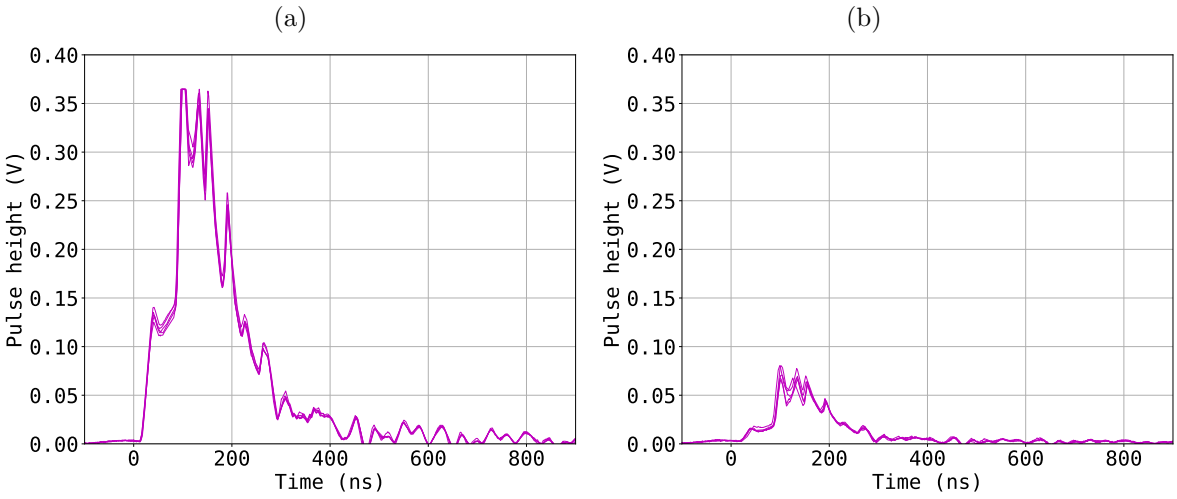

Figure 6.16: Waveforms of the $\bar{p}$ beam obtained from the MCP in the reaction chamber (a) when the $\bar{p}$ beam passes through the free space, and (b) when the $\bar{p}$ beam passes through the cavity target and the collimator.

6.3.2 Background Signal Detection

Using the $\bar{p}$ beam with these characteristics, a few shots were taken for the background measurements during the $\bar{\mathrm{H}}$ production experiment in 2024. The measurements should have been conducted under a condition similar to the actual spectroscopic measurement as much as possible, but we compromised to take the data without the high voltages on the quenching electrodes of the Lyman-α detector. This is because we observed so large background signals when the high voltages were applied, that the power supply of the MCPs tripped once with a certain current limit. This suggests that the $\bar{p}$ beam was off-centered and the trajectory was deviated by the quenching E-field, which has a axially symmetric distribution in principle. Therefore, a dedicated beam steering has to be performed with the quenching E-field present, to reduce the background for the planned $\bar{\mathrm{H}}$ Lamb shift spectroscopy. In addition, another compromise was made to operate the MCPs of the Lyman-α detector with relatively low bias voltages of 0 V and 1800 V on the front and back side respectively, to avoid the risk of damaging the MCPs under such a high background rate.

In this measurement, as well as the planned $\bar{\mathrm{H}}$ Lamb shift spectroscopy, the oscilloscope of the Lyman-α detector is triggered based on the timing of the beam extraction from the $\bar{p}$ trap. Figure 6.17 shows waveforms from each MCP channel obtained from one shot of the trap-extracted $\bar{p}$ beam, with a CAD model of the beam line to indicate the geometry corresponding to the timing. Within the expected time window of 100 ns represented by the two vertical black solid lines, the detected peaks are shown as the purple crosses. The peak detection threshold is set -10 mV for all the channels. The time window is defined more tightly than in the H^- & C-foil experiment, so that it captures precisely the period from when $\bar{p}$s enter the upstream ring support until they exit the downstream ring support

of the Lyman-α detector. This tighter definition is preferred due to frequent background signals before and after the beam arrival time.

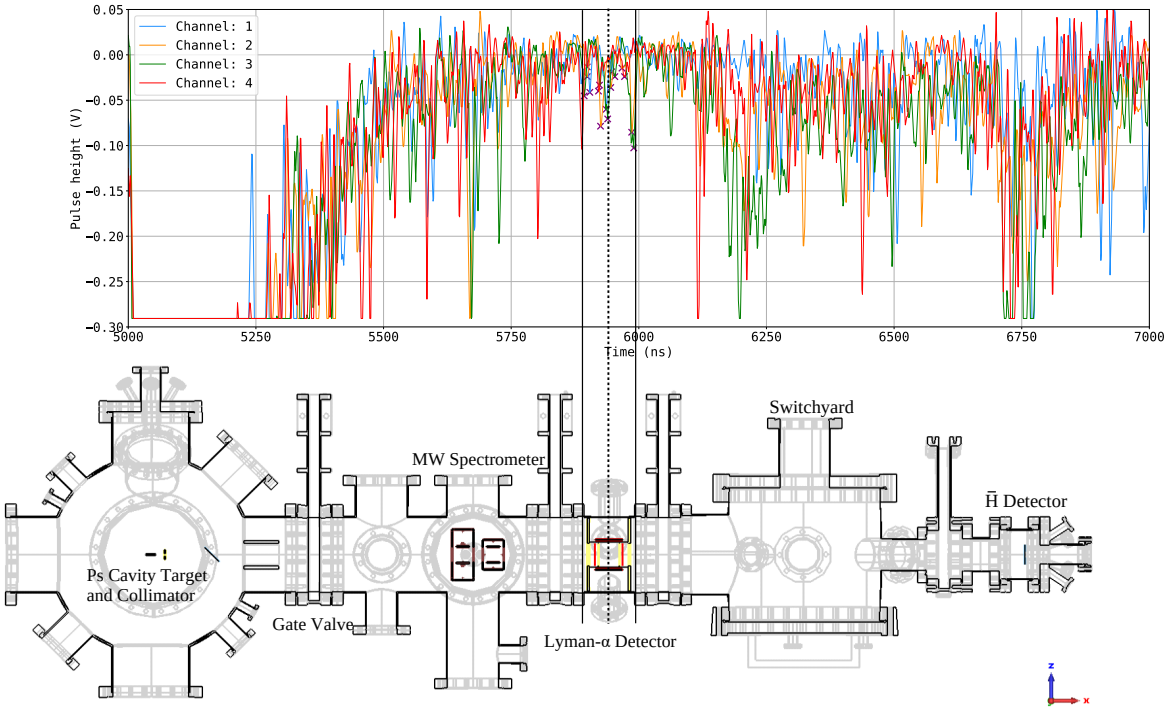

Figure 6.17: Waveforms and detected peaks from each MCP channel of the Lyman-α detector obtained from one extraction of the $\bar{p}$ beam from the trap.

Within this time window, this particular shot in Figure 6.17 detected 3, 5, 5, and 3 peaks for channels 1, 2, 3, and 4, respectively. Also, one can see that the waveform is saturated around 5 μs, which is more or less when the $\bar{p}$s are arriving at the reaction target and producing a lot of the secondary particles from their annihilation. Besides, outside the time window, certain populations of the peaks can be seen around 6.25 μs, 6.50 μs, and 6.75 μs, which correspond to the arrival time at the entrance and exit of the switchyard, and the $\bar{\text{H}}$ detector, respectively.

The data-taking was repeated 5 times to accumulate statistics of the peak signals. Figure 6.18 shows a histogram of the total peak count of all channels of the MCPs normalized by the number of shots, with a bin width of 10 ns. The peaks outside the time window are also analyzed here and counted to the histogram to see the background time spectrum in a wide range. The dashed line at 5.10 μs represents the arrival time of the beam center to the center of the reaction chamber, where there are the cavity target and collimator. The absence of the peak from 5.00 μs to 5.25 μs is because the peak finder fails to work due to the saturation of the waveform.

The total peak count within the time window for 100 ns, which is represented by the same solid lines as those in Figure 6.17, is 13.2. This means the background rate of almost 1 per 10 ns within the time window.

In 2022, a similar background measurements were performed. At the time, the 20 mm bore model MW spectrometer were used in a smaller vacuum chamber. Also, the $\bar{p}$ beam was transported without the $\bar{p}$ trap, thus having a larger spatial divergence. Furthermore, the flat target shown in Figure 2.3(a) was used instead of the cavity target, which allowed the $\bar{p}$ beam propagate downstream with a larger halo. As a consequence, much more

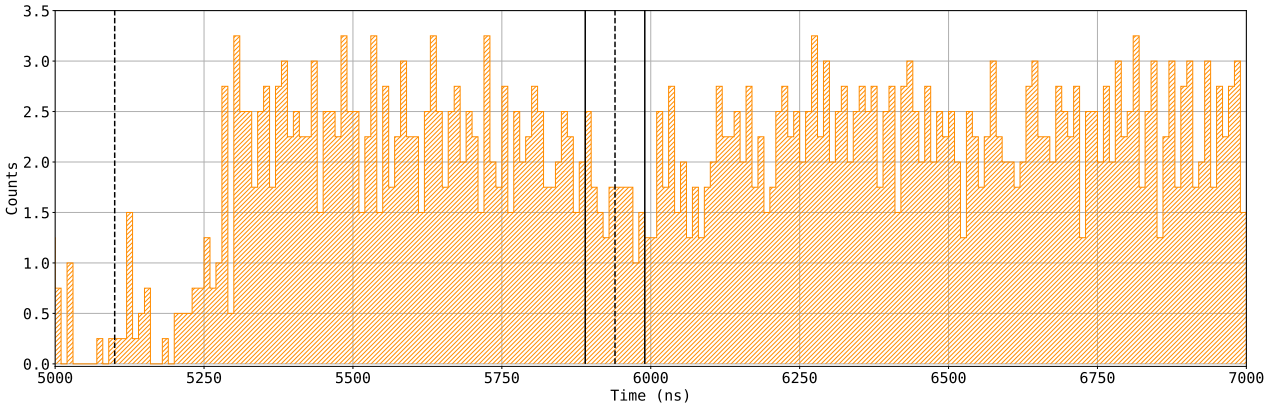

Figure 6.18: Histogram of the total peak count of all channels of the MCPs in the Lyman-α detector. The peaks outside the time window are also analyzed here.

$\bar{p}$s were annihilating around the spectroscopy setup, and the waveforms of the Lyman-α detector exhibited the saturation even around the time window.

The background signals observed in 2024 are significantly reduced compared with those observed in 2022, and the experimental conditions have improved to the point where the single peak detection is now feasible within the time window.

6.3.3 Closed-valve Background Measurement

The background signals can originate mainly from $\bar{p}$s annihilating close enough to the Lyman-α detector when the $\bar{p}$ beam is passing through the detector region. On top of that, considering that a majority of the $\bar{p}$s extracted from the $\bar{p}$ trap annihilate in the reaction chamber, there can be some $\bar{p}$s from a slow component of the beam annihilating inside the reaction chamber but unfortunately within the time window, and secondary particles traveling nearly at the speed of light strike the MCPs and contribute as background signals within the time window.

Contributions by such delayed annihilation can be characterized by obtaining waveforms when the whole $\bar{p}$s in a bunch annihilate all at once and evaluating the count rate of the delayed signals. For this purpose, additional shots of the $\bar{p}$ beam were taken with a gate valve between the reaction chamber and MW spectrometer closed, which ensures that the $\bar{p}$s completely annihilate at the valve. The valve position is indicated in Figure 6.17 Such a closed-valve background measurement allows for the extraction of a time spectrum resulting from the full annihilation of the $\bar{p}$ beam.

Figure 6.19 shows waveforms obtained from each MCP channel of the Lyman-α detector obtained in the closed-valve background measurement. The dashed line at 5.10 μs represents the arrival time of the $\bar{p}$ beam center to the center of the reaction chamber. The arrival time to the valve is around 5.37 μs, which is represented by the purple dashed line.

The peaks detected within the time window are shown as well, which are represented by the purple crosses. The peak detection threshold, represented by the horizontal dashed line, is set -10 mV. One can see that even after the arrival time at the valve, the background signals remain for more than a couple of us, fully covering the time window.

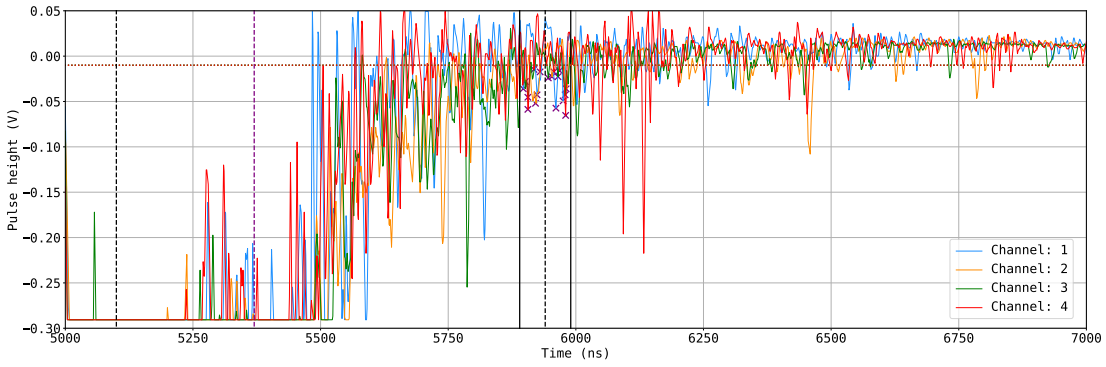

Figure 6.19: Waveforms and detected peaks from each MCP channel of the Lyman-α detector obtained from one extraction of the $\bar{p}$ beam from the trap, obtained in the closed-valve background measurement.

The data-taking was repeated 4 times to accumulate statistics. Figure 6.20(a) shows a histogram of the total peak count of all channels of the MCPs normalized by the number of shots, with a bin width of 10 ns. In Figure 6.20(b), the same histogram is shown with the full time range. The arrival time to the center of the reaction chamber and valve are represented by the black dashed line at 5100 ns and the purple dashed line at 5370 ns, respectively. In this case as well, the peaks are not detected at the saturated region in the waveforms, which is wider than that in Figure 6.18 and extends to around 5.5 μs because of the additional annihilation at the valve after the cavity target.

The total peak count within the time window in this case is 20.2, which is higher

by 7 than the standard background measurement in Figure 6.18. Also, one can see in Figure 6.20(b) that the signals due to the delayed annihilation remains even for 4 μs after the arrival time at the valve.

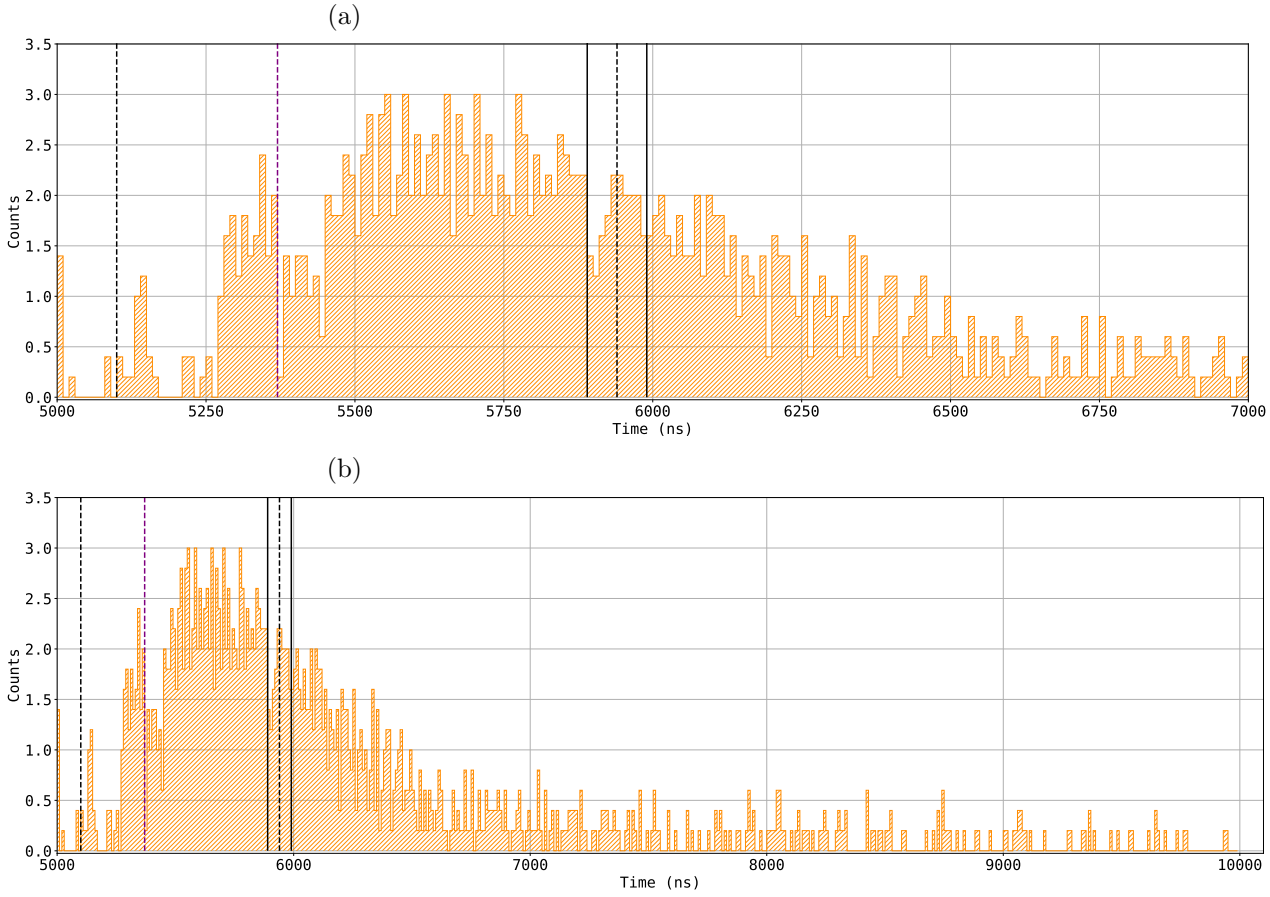

Figure 6.20: (a) Histogram of the total peak count of all channels of the MCPs in the Lyman-α detector, and (b) the same histogram with the full time range, obtained in the closed-valve background measurement. The peaks outside the time window are also analyzed here.

6.3.4 Possible Source of the Background Events

To interpret the results obtained in the previous section, the following sources are considered: First, the temporal structure of the $\bar{p}$ pulsed beam. Second, high-energy particles and γ-rays associated with delayed decays of unstable nuclei generated by the $\bar{p}$ annihilation. Third, Rutherford scattering of $\bar{p}$s by target nuclei.

For the temporal structure, a Gaussian beam is assumed with a full width at 4σ of 250 ns, corresponding to a FWHM of 150 ns, equivalent to 2.35σ in measurements. For a beam of 10^6 $\bar{p}$s, the fraction of components extending beyond 250 ns is approximately 0.003% or 30 $\bar{p}$s. Assuming a pencil beam hitting the valve, the solid angle of the four MCPs in the Lyman-α detector is approximately 10^{-3}. The total multiplicity of the secondary particle can be assumed to be 5, accounting for 3 $\pi^{\pm}$ and 2 $e^{\pm}$ from the pair creation process. Using all the estimates above, the background rate 250 ns after the arrival time at the valve is approximated as 0.15, which is only 5% of the value of 3 seen around the corresponding timing (5.6 μs) in Figure 6.20. This suggests that the actual

contribution of the temporal structure may be higher.

The contributions of unstable nuclei generated by the $\bar{p}$ annihilation and $\bar{p}$ Rutherford scattering were qualitatively studied using Geant4 (v11.2.2) [98–100]. The simulations employed the FTFP_BERT_EMZ physics list, combined with the G4EmStandardPhysicsWVI model to account for large-angle scattering by nuclei. A simplified CAD model of the experimental apparatus was used for the simulations.

To study the contribution by unstable nuclei, $\bar{p}$ annihilation was simulated by placing 10^6 $\bar{p}$s on the surface of the valve, thus immediately annihilating the $\bar{p}$s. Figure 6.21 shows the TOF spectrum of $\pi^{\pm}$, $e^{\pm}$, $\mu^{\pm}$, and photons detected by any of the four MCPs, binned every 10 ns. e^{-}s plotted in the figure are exclusively those generated via pair production from γ-rays. The time-zero corresponds to the moment of the $\bar{p}$ annihilation, with the Lyman-α detector's time window indicated by the vertical lines. There are a couple of counts around 250 ns, and a long tail can be seen following the prompt annihilation peak. Since the temporal structure of the $\bar{p}$ beam was not incorporated in this estimate, the tail contribution is underestimated.

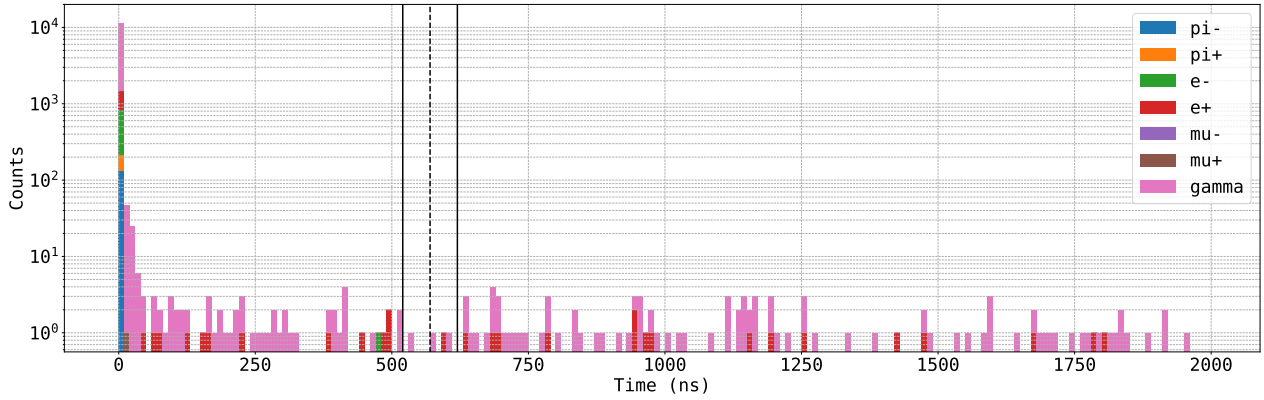

Figure 6.21: Histogram of simulated timing at which tracks hit the front surface of the MCPs, stacked for some different particle types. All the $\bar{p}$s are placed on the surface of the valve with zero kinetic energy, so that all the $\bar{p}$s annihilate at the time-zero.

For the Rutherford scattering of $\bar{p}$s, it should be noted that there is insufficient experimental data for $\bar{p}$ scattering by nuclei at keV energies. The only relevant data comes from a reanalysis of the OBELIX experiment at the LEAR facility before the AD/ELENA era, which reported a 20 – 30% reflection probability for 1 – 10 keV $\bar{p}$s interacting with aluminum vacuum chamber walls [101, 102]. The phenomenon is not firmly validated by any other experiments. In general, for heavier nuclei in the stainless steel used for the vacuum chambers of this study, $\bar{p}$ scattering is expected to result predominantly in annihilation.

Based on these premises, another Geant4 simulation was performed injecting 10^6 pencil beam of $\bar{p}$s to the valve at 6 keV in the simplified CAD model. The resulting time spectrum is shown in Figure 6.22. The prompt peak arises from the $\bar{p}$ annihilation. The broad peak observed around 100 ns is attributed to the backscattered $\bar{p}$s annihilating on the surface of upstream components, such as vacuum chamber walls or beam steering electrodes. The 100 ns delay corresponds approximately to the flight time from the valve to these upstream structures. The extended tail likely results from $\bar{p}$s traveling further distances or multiple reflections. The reflection probability in this simulation is 20%. It should be noted that Geant4 is primarily developed for high-energy particles' interaction and is unsuitable for quantitative analysis of low-energy $\bar{p}$s. The backscattering cross-section for low-energy $\bar{p}$s with nuclei remains unknown, necessitating future experimental verification by any

experiments at the ELENA facility.

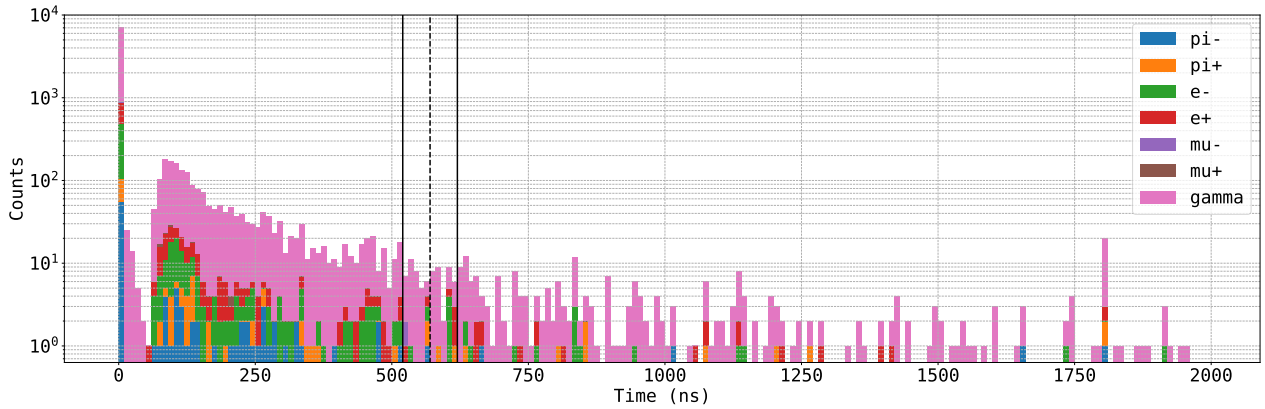

Figure 6.22: Histogram of simulated timing at which tracks hit the front surface of the MCPs, stacked for some different particle types. $\bar{p}$s are injected to the valve as a pencil beam at 6 keV.

The background contributions to the Lyman-α detector are likely due to the factors outlined above. The followings are under consideration to mitigate these effects:

- Introducing apertures upstream of the reaction target along the $\bar{p}$ beam line to remove the beam halo that does not contribute to the $\bar{\mathrm{H}}$ production.
- Blocking slow components of the $\bar{p}$ beam by a pulsed high voltage.
- Employing a novel detector combining a wavelength shifter and a photomultiplier instead of MCPs, which are highly sensitive to low-energy charged particles.

In Addition, applying the bias voltages on the MCPs only during the time window for detecting the Lyman-α photons would minimize the large background coming from the reaction chamber and stabilize the baseline signal. This modification would be essential to reduce interference caused by excessive charged particle detection.

6.4 Conclusion

We conducted some commissioning experiments of the Lyman-α detector to check the performance of the defector and measure the background signal for the upcoming Lamb shift measurement.

Firstly, the Lyman-α detector's response to UV photons were characterized by using a UV LED source. Pulse height spectra of the UV photon signal were obtained under different bias voltages on the MCPs, which will be informative for the data analysis in the Lamb shift measurement.

Secondly, a pilot measurement of the Lamb shift transition was conducted using a H beam produced by a H^- ion beam and a C-foil. In this measurement, we managed to test the triggered operation of the spectroscopy setup and the DAQ system. However, signal count rates obtained from the off-resonance mode did not clearly show the excess over those obtained from the on-resonance mode, which could indicate a decline in the Lyman-α detector's efficiency. If this is indeed the case, the efficiency decline can be attributed to deliquescency of CsI coated on the MCPs in the Lyman-α detector.

Lastly, some measurements of the background signals were performed, using the $\bar{p}$ beam extracted from the $\bar{p}$ trap for the first time. We confirmed that the upgraded MW spectrometer, featuring a larger borehole, combined with the use of the trap-extracted $\bar{p}$ beam and the Ps cavity target, resulted in significantly lower count rates compared to previous measurements. Also, the time spectrum of the background signal was studied by completely annihilating the $\bar{p}$ beam and comparing the measurement with Monte Carlo simulations. In this study, surprisingly long time spectrum of the background was observed, which is suspected to be due to the temporal structure of the $\bar{p}$ beam, delayed radioactive decay of unstable nuclei, and delayed annihilation of backscattered $\bar{p}$s. Regardless of the variations in these processes, background signals would be suppressed by either trimming the $\bar{p}$ beam profile or deflecting the slow component in the beam's temporal structure. Additionally, another type of Lyman-α detector can be envisioned, which, for example, employs a wavelength shifter and photomultiplier to be less sensitive to charged particles.

Chapter 7

$\bar{\mathrm{H}}$ Production Experiment

Towards the $\bar{\mathrm{H}}$ Lamb shift measurement, we participated in the $\bar{\mathrm{H}}$ production experiment conducted by the GBAR collaboration. In this chapter, the first production experiment in 2022 is reviewed with detailed descriptions of the data analysis method. Then, the second experiment ongoing in 2024 is described with a preliminary analysis result.

7.1 Mixing on Flat Target

In the beam time of 2022, the GBAR experiment conducted the $\bar{\mathrm{H}}$ production experiment with the decelerated 6 keV $\bar{p}$ beam for the first time, and demonstrated a production of beam-like $\bar{\mathrm{H}}$ atoms via the charge-exchange reaction [44].

Figure 7.1 illustrates the scheme of the $\bar{p}/\bar{\mathrm{H}}$ beam line as of the beam time in 2022. As a major difference than the beam line which is described in Section 2.5.1, the $\bar{p}$ trap was in test phase at the time and a simple transfer line had been installed between the decelerator and the reaction chamber. Also, instead of the 30 mm model MW apparatuses, the 20 mm models described in Section 4.5 had been installed, with a smaller vacuum chamber than what is described in Section 4.4.4. The decelerated $\bar{p}$ beam has a larger divergence, and we could not well focus the beam to the Ps cavity target, thus adopted the flat target for the most of the beam time.

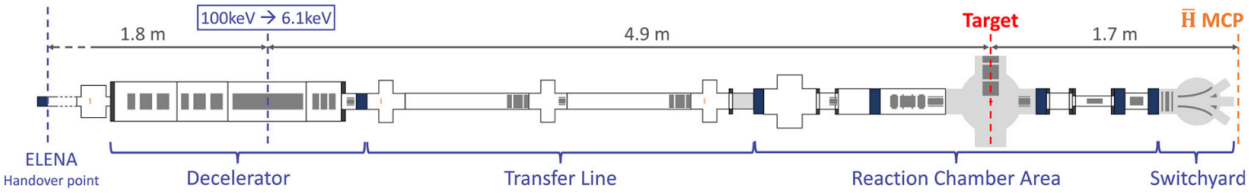

Figure 7.1: Scheme of the GBAR $\bar{p}/\bar{\mathrm{H}}$ beam line as of 2022, adapted from Reference [44]

Figure 7.2 illustrates the scheme of mixing the $\bar{p}$ beam and the e^+ beam with the flat target. First, the e^+ beam is extracted from the HFT onto the flat target, with an intensity of 3.9×10^7, a time width of 17 ns (FWHM), and an implantation energy of 4.3 keV [44]. At this implantation energy, the Ps atoms starts to emit from the target surface after 10 ns with RMS of 2 ns [103]. As shown in Figure 7.2, the e^+ beam has a rectangle profile of 5 mm height and 10 mm length. The Ps atoms emit with a cosine distribution, and the Ps cloud diffuses in the vacuum following a Maxwell-Boltzmann velocity distribution with an average of 0.121 mm/ns [104, 105]. The total number of Ps atoms were measured by a

$PbWO_4$ scintillation detector as $6.8(1.5) \times 10^6$ [44] per pulse, which means a efficiency of the e^+ converting to the Ps of 20%. 30 ns after the arrival of the e^+ beam on the target plane, the $\bar{p}$ beam arrives at the center of the target plane, which is the optimum timing to maximize the overlap between the $\bar{p}$ and Ps.

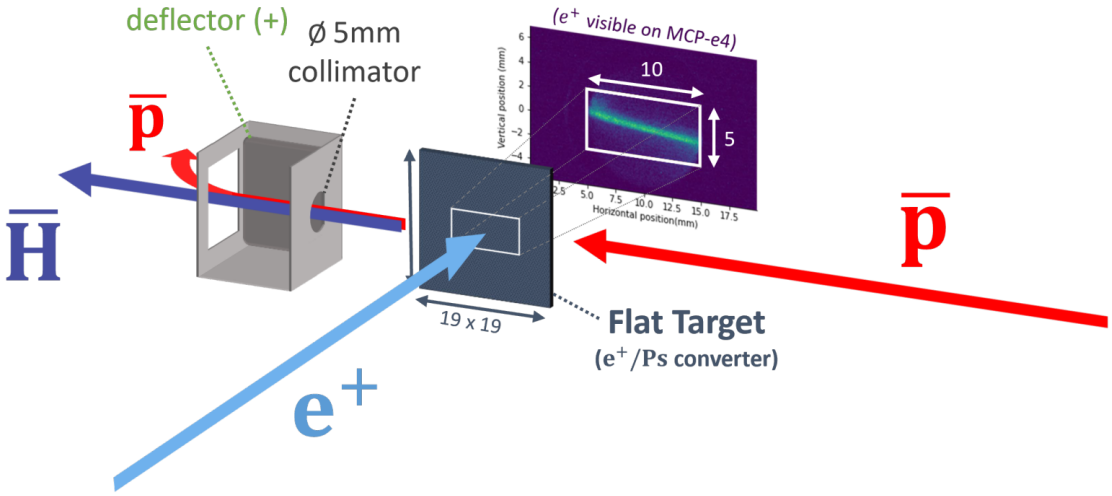

Figure 7.2: Scheme of mixing the decelerated $\bar{p}$ beam and the e^+ beam with the flat Ps target, apapted from Reference [56].

The $\bar{p}$ beam had a Gaussian timing profile with a standard deviation of 96 ns, and a mean kinetic energy of 6.10(5) keV [44,56]. From SIMION simulations, the beam transmission efficiency — a ratio of the number of particles accepted by the $\bar{H}$ detector downstream over the total number of particles passing through the reaction target — was evaluated for the $\bar{p}$ and $\bar{H}$ atom to be 72% and 68%, respectively [44, 56].

For an evaluation of the intensity of the $\bar{p}$ beam passing through the target region, a few shots of the $\bar{p}$ beam were taken offline to pass through the $\bar{p}$ beam to the $\bar{H}$ detector and completely annihilate $\bar{p}$ on the MCP of the $\bar{H}$ detector. Then, high-energy secondary particles from the $\bar{p}$ annihilation were detected by a CMOS image sensor (SONY IMX264LLR equipped with Baumer VCXG-51M) used as a 2D tracking detector, which was installed right above the vacuum chamber of the $\bar{H}$ detector. Most of the secondary particles are almost minimum ionizing particles such as $\pi^\pm$ from the $\bar{p}$ annihilation and $e^\pm$ produced by the pair creation process of a γ-ray from neutral π^0 decay. The number of the detected secondary particles was converted to the number of $\bar{p}$s annihilating on the MCP by multiplying a conversion factor which takes into account a multiplicity of the secondary particles that can emerge from one $\bar{p}$ annihilation with nucleus of the MCP surface material, an approximate solid angle of the CMOS sensor seen from the center of the MCP, and the $e^\pm$ pair creation probability inside a few mm thick stainless wall of the vacuum chamber which is the main material present between the annihilation point and the CMOS sensor. The $e^\pm$ pair creation probability and the $\pi^\pm$ absorption probability were calculated by a simple Monte Carlo simulation by using Geant4 [98–100]. Correcting the $\bar{p}$ beam intensity measured as such by the transmission efficiency evaluated by the SIMION simulations, the $\bar{p}$ beam intensity at the reaction target was finally evaluated to be $3.1(7)\ 10^6$ [44].

Inputting these characteristics of the $\bar{p}$ beam and e^+ beam to Equation (2.4), the expected $\bar{H}$ production rate was computed as 1.1 ± 0.4 $\bar{H}$ per 100 shots with the cross-section from the Close Coupling method [45] and 2.5 ± 0.9 $\bar{H}$ with the cross-section from

the Coulomb-Born approximation [48].

After the reaction target, the electrostatic deflector deviates the $\bar{p}$ beam, and the $\bar{p}$s almost completely annihilate hitting on the reaction chamber wall, which significantly reduce the background in the $\bar{H}$ detector located about 1.7 m downstream.

During the beam time, the data-taking were conducted mainly for the mixing (MIX) mode, where both the $\bar{p}$ and e^+ beam are injected to the reaction target, and for the $\bar{p}$ background (BGD) mode, where only the $\bar{p}$ beam is injected to the target. After selecting the data on the criteria of the presence of the beam at the right timing, 6897 and 8468 shots (AD cycles) were found for the MIX and BGD mode, respectively [44].

7.1.1 Waveform Analysis

As a consequence of deflecting the $\bar{p}$ beam right after the reaction target, only the neutral particles i.e. the $\bar{H}$ atoms pass through the beam line towards the $\bar{H}$ detector. The $\bar{H}$ atoms have a characteristic kinetic energy of 6.10(5) keV taken over from the $\bar{p}$ beam, which marks a characteristic arrival time to the $\bar{H}$ detector.

By applying a typical bias voltage of 2200 V on the $\bar{H}$ detector MCP, Electric pulse signals of incident particles were clearly observed. Only the pulse signals showing up within an expected time window, which was calculated in advance from a TOF spectrum of the $\bar{p}$ beam without the deflection, were analyzed.

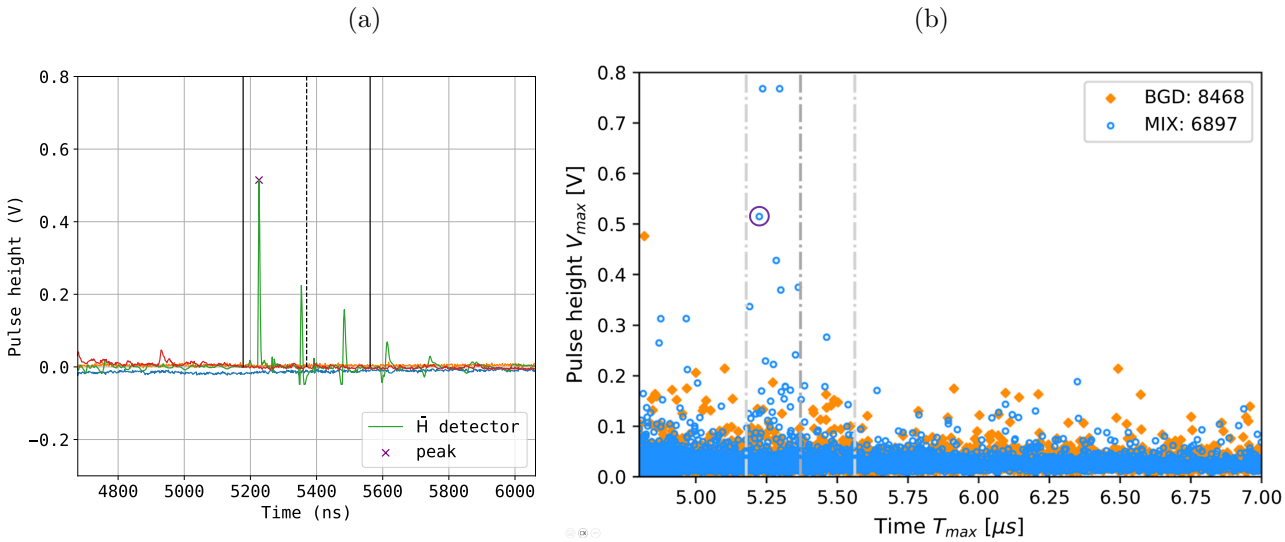

Figure 7.3: (a) Waveform (green) of an $\bar{H}$ candidate event obtained from the $\bar{H}$ detector, and (b) scatter plot of the timing and pulse height of the peaks which are the highest peaks from each shot. (b) is adapted from Reference [44].

Figure 7.3(a) shows a waveform (green) of an $\bar{H}$ candidate event obtained from the $\bar{H}$ detector. The expected time window of 5370 ± 192 is represented by the solid lines. As shown in the figure, it was found that the pulse signals accompany with the ringings repeated a couple of times with a period of about 130 ns, presumably due to reflections of the electric signals. In the waveform analysis, peaks of the pulse signals were detected using the scipy.signal.find_peaks [90], as represented by the purple crosses in Figure 7.3(a). Only the peaks above a certain pulse height threshold and within the time window were selected, and the peaks of the ringings were removed by masking the region of the waveform behind the first main peak for a few hundreds ns.

Figure 7.3(b) shows a scatter plot of the timing and pulse height of the peaks which are the highest peaks from each shot. The data point of the peak in Figure 7.3(a) is bounded by the purple circle. Selecting only the highest peak out of each waveform is to ensure that the data points are not from the ringings but from the main peaks of the shot, considering that there should be hardly any shots containing more than one $\bar{H}$ candidate event given the production rate of almost 1 $\bar{H}$ per 100 shots [44].

Using these peak signals detected both in the MIX and BGD mode, binomial tests was performed to examine a null hypothesis that the MIX peaks and BGD peaks are sampled from the same population of a binomial distribution. A main free parameter in the peak detection is the pulse height threshold. By setting a threshold value of 0.1 V, 32 MIX peaks and 15 BGD peaks are selected, and the null hypothesis was rejected with a statistical significance of 3.1σ [44]. Supposing an absolute detection efficiency of the MCP for the 6.1 keV $\bar{H}$ atoms to be 50%, a cross-section of the charge-exchange reaction (2.1) at this energy was evaluated to be $11 \pm 5 \times 10^{-16}$ cm^2 [56]. It should be noted that this was preliminary evaluated as a lower limit of the cross-section, considering an ambiguity of the $\bar{H}$ transmission efficiency discussed in Reference [56].

7.1.2 Image Analysis

To compliment the waveform analysis, images taken from the phosphor screen and CCD camera were analyzed as well. When an $\bar{H}$ atom hits the MCP at a kinetic energy of 6 keV, the $\bar{p}$ loses its kinetic energy and eventually annihilates with a proton or neutron of a nucleus inside the MCP, and produces about three $\pi^{\pm}$s and two π^0s on average, depending on the nuclide of the nucleus of the annihilation target. The $\pi^{\pm}$s traveling some distance inside the MCP with a kinetic energy of around 200 MeV can produce longer pixel clusters in the image, compared to those created by background particles. Also, annihilation of a $\bar{H}$ atom on the MCP surface can deposit more energy, possibly exhibiting a brighter pixel cluster.

Furthermore, additional dataset was taken in a run called Low Pbar Number (LPN) mode, where just the $\bar{p}$ beam was transported through the beam line under steering parameters which enable only a few $\bar{p}$s to hit the $\bar{H}$ detector. As such, single event of the $\bar{p}$ annihilation on the MCP can be analyzed to characterize the signal of the $\bar{H}$ atom.

The images were taken with a typical bias voltage of 4000 V on the phosphor screen, and the CCD camera was triggered at the arrival time of the $\bar{H}$ atoms and exposed for 1 μs to fully cover the time window. To analyze the pixel clusters, a couple of different clustering algorithms were used, and the analysis described in this thesis adopts an algorithm called segmentation [106]. There is a variety of segmentation algorithms, especially for classifying multiple objects in RGB images. In our analysis, the images are all in greyscale, and just a binary classification ($\bar{H}$ atom or background) is of interest at the moment. Therefore, the simplest version of the segmentation algorithm, which groups adjacent pixels above a certain threshold in pedestal subtracted images, was adopted to detect clusters. For the implementation, scikit-image library [107] was used.

Figure 7.4 (a) shows an image including a pixel cluster of an $\bar{H}$ candidate event obtained by the CCD camera of the $\bar{H}$ detector, which is from the same shot as that of the waveform in Figure 7.3. The detected clusters are bounded by the red rectangles. The largest cluster in the right bottom region of the image is the $\bar{H}$ candidate event.

Assuming that the pixel value is positively correlated to the energy deposited on the corresponding point on the MCP, one could expect that the charge i.e. sum of pixel values of the cluster, could correlate to the total energy deposited by the event, which should also correlate to the pulse height of the corresponding peak obtained in the waveform analysis.

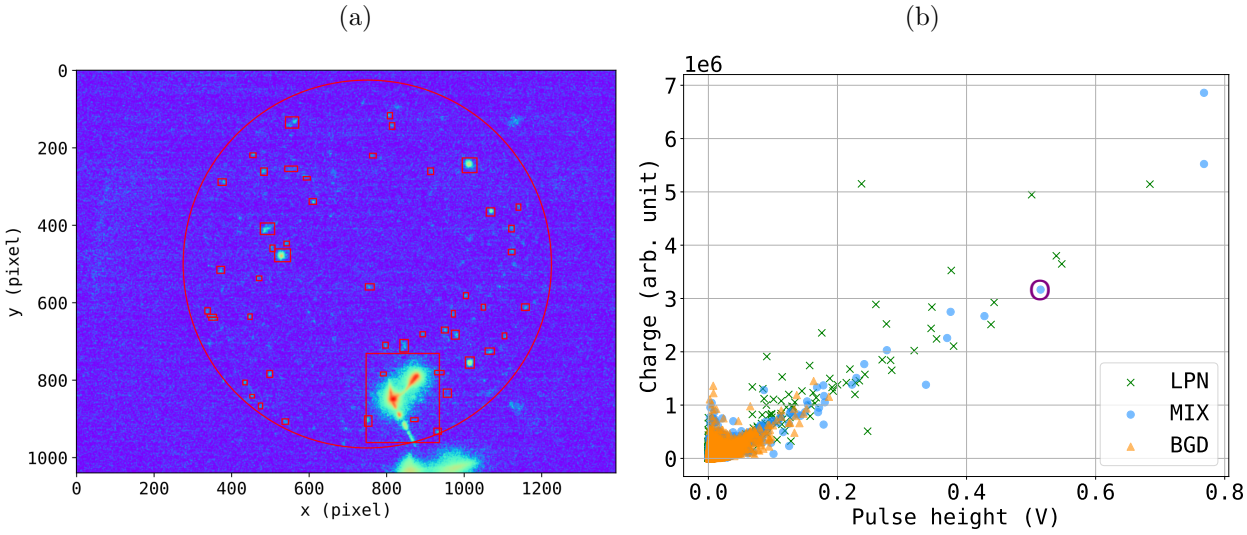

Figure 7.4: (a) Pixel cluster of an $\bar{H}$ candidate event, and (b) correlation plot between the pulse height of the highest peak in each shot and the largest charge among clusters in the corresponding shot, displayed for the MIX(blue circle), BGD(orange triangle), and LPN(green cross) modes

Therefore, both the charge and pulse height are expected to be larger in the MIX or LPN modes due to the $\bar{p}$ annihilating on the MCP, than in the BGD mode.

Figure 7.4(b) shows a correlation plot between the pulse height of the highest peak in each shot and the largest charge among clusters in the corresponding shot, displayed for the MIX(blue circle), BGD(orange triangle), and LPN(green cross) modes. The data point of the $\bar{H}$ candidate cluster in Figure 7.4(a), thus the same event leaving the pulse signal in Figure 7.3(a), is bounded by the purple circle. One can see that the charge values in the MIX mode distribute with a higher tail as well as those in the LPN mode, while those in the BGD mode distribute only up to around 1.5×10^6. Also, a certain positive linear correlation between the charge and the pulse height can be seen in all three modes.

It should be noted that in the case of image analysis, all the signals recorded during the 1 μs exposure time are detected as clusters, while in the case of waveform analysis, only the signals inside the time window are detected as peaks. Therefore, some large clusters can still be seen even without accompanied by any high peaks within the time window of the corresponding waveform, which are the data points populating a little bit along the y-axis in Figure 7.4(b).

In a similar cluster analysis described in Reference [44], 22 and 6 clusters were obtained from the MIX and BGD dataset respectively, by setting a charge threshold value of 5×10^5. The binomial test supports the observation of the $\bar{H}$ atoms with a statistical significance of 3.6 σ, a similar value to that in the waveform analysis.

7.2 Mixing in Cavity Target

In the beam time of 2024, the GBAR experiment conducted the second $\bar{H}$ production experiment using the $\bar{p}$ beam extracted from the $\bar{p}$ trap for the first time, with some more other improvements. Figure 7.5 illustrates the scheme of the $\bar{p}/\bar{H}$ beam line in 2024, which is described in Section 2.5.1. In this setup, the MW spectrometer and vacuum chamber described in Section 4 has been installed.

The trap-extracted $\bar{p}$ beam has a much smaller divergence, and the intensity at the position of the downstream MCP ('MCP-p3') is preliminarily measured to be around 5×10^6, which is almost the half of the intensity at the extraction from the ELENA.

On the e^+ side, more than an order of magnitude of increase in the beam intensity has been observed at the extraction from the HFT, compared to 2022, as a consequence of the BGT operation with the SiC remoderator and an upgrade of the electrode stack in the HFT and extraction accelerator.

Furthermore, automated parameter optimization programs were developed for the beam steering, which have been improving the beam intensity for both the e^+ beam line and $\bar{p}$ beam line.

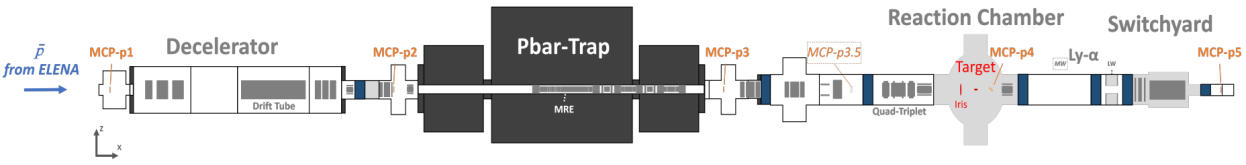

Figure 7.5: Scheme of the GBAR $\bar{p}/\bar{H}$ beam line as of 2024, adapted from Reference [59]

Given all these improvement, the number of $\bar{p}$s passing through the cavity target and the number of Ps atoms produced inside the target have been preliminarily measured as around 10^6 by the CMOS sensor and 7×10^6 by the $PbWO_4$ scintillation detector, respectively. By inputting these beam characteristics into Equation (2.4), the expected $\bar{H}$ production rate has been calculated to reach the order of 0.1 $\bar{H}$ per AD cycle.

7.2.1 Preliminary Waveform Analysis

The production experiments have been performed with a couple of different kinetic energies for the $\bar{p}$ beam. Using an $\bar{p}$ beam of 6 keV, a few thousands of shots were taken in both the MIX and BGD mode. As a preliminary result from the ongoing experiment, Figure 7.6 shows a scatter plot of the timing and pulse height of the peaks detected by the $\bar{H}$ detector, obtained in the production experiment using the 6 keV $\bar{p}$s.

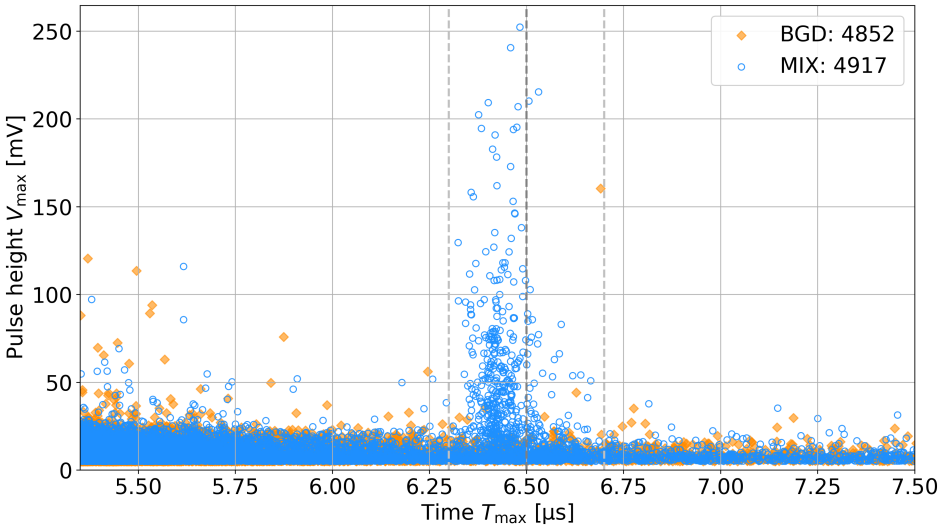

Figure 7.6: Scatter plot of the timing and pulse height of the peaks being obtained by the $\bar{H}$ detector using the 6 keV $\bar{p}$ beam in 2024.

In this dataset, 388 MIX peaks and 13 BGD peaks are detected with a pulse height threshold of 20 mV, and the $\bar{H}$ production rate has been evaluated to be 0.08 $\bar{H}$ per AD cycle, which is roughly 8 times more than in 2022. With this improved production rate, the Monte Carlo simulation of the spectroscopy described in Section 5.6 predicts a spectroscopy precision of 10% for a few months of data-taking. This would be the first goal to be achieved in the next beam times.

7.3 Conclusion

The $\bar{H}$ production experiments were conducted by the GBAR collaboration for the first time during this research. In this experiment, we have collected two different dataset, the MIX mode to use both the e^+ beam and $\bar{p}$ beam to produce the $\bar{H}$ atoms, and the BGD mode to use only the $\bar{p}$ beam to extract the background signals.

In the first experiment in 2022, the Ps flat target was employed and datasets of a few thousand AD cycles were recorded for both the MIX and BGD modes. In the data analysis, we analyzed both the waveforms and images obtained from the $\bar{H}$ detector, and confirmed the production of $\bar{H}$ atoms. The production rate in this experiment was evaluated to be almost 0.01 $\bar{H}$s per AD cycle. This was the world's first demonstration of $\bar{H}$ synthesis under the charge-exchange reaction (2.1) in the keV energy regime.

In the subsequent experiment conducted in 2024, a number of efforts were made by the GBAR collaboration for both the e^+ beam line and $\bar{p}$ beam line. In particular, the $\bar{p}$ trap has started operating, which has allowed for the employment of the Ps cavity target. A preliminary analysis on a dataset obtained during this beam time shows the $\bar{H}$ production rate of almost 0.1 $\bar{H}$s per AD cycle, which is almost an order of magnitude of improvement compared to the first experiment in 2022. With this production rate, the Lamb shift measurement aiming at 10% spectroscopy precision would be feasible as numerically demonstrated in Section 5.6.

Chapter 8

Conclusion

8.1 Summary

Towards a direct measurement of the $2S_{1/2}$-$2P_{1/2}$ Lamb shift transition frequency in $\bar{\mathrm{H}}$ atoms, development of a MW spectrometer and $\bar{\mathrm{H}}$ production experiments in the GBAR experiment are mainly described in this thesis.

The Lamb shift in $\bar{\mathrm{H}}$ atoms has never been directly measured, and experimental determination of the antiproton charge radius is yet to be achieved. In the GBAR experiment, an $\bar{\mathrm{H}}$ production experiment has been running by using a charge-exchange reaction between $\bar{p}$s at a few keV and Ps atoms. In this reaction, the production of $\bar{\mathrm{H}}(2\mathrm{S})$ atoms is predicted, which will be available for the Lamb shift spectroscopy in a magnetic field-free region.

One of the keys for the spectroscopy is to reduce background signals due to $\bar{p}$ annihilation around the spectroscopy setup. A MW spectrometer with a borehole diameter of 20 mm was previously installed in the GBAR beam line till 2022, and a significant amount of the background signals were observed due to $\bar{p}$s annihilating at the MW spectrometer. To reduce the $\bar{p}$ annihilation at the MW spectrometer, we developed a new MW spectrometer with a borehole diameter of 30 mm, by updating geometries of the 20 mm bore model based on MW simulations. The MW spectrometer consists of two apparatuses, the HFS and MWS. The HFS de-excites $\bar{\mathrm{H}}(2\mathrm{S})(F = 1)$ atoms in advance, and the MWS sweeps the MW frequency to obtain the Lamb shift spectrum by the selected $\bar{\mathrm{H}}(2\mathrm{S})(F = 0)$ atoms, in order to achieve a high-precision spectroscopy. The HFS produced in this research is optimized to have a resonant property at 1.1 GHz for efficiently de-exciting $\bar{\mathrm{H}}(2\mathrm{S})(F = 1)$ atoms, and the MWS is optimized to realize a high MW transmission efficiency with a small frequency dependency over the frequency range to scan. We installed the MW spectrometer to the GBAR beam line, and performed online power characterization to confirm that an expected power of MW signal was input to the apparatus.

To evaluate the performance of the spectroscopy setup and estimate the data-taking period and so on, we developed a numerical calculation program by implementing spatial distributions of the $\bar{\mathrm{H}}$ beam, MW E-fields, and DC E-field of the Lyman-α detector. Using this program, de-excitation efficiency of the MW apparatuses and detection efficiency of the Lyman-α detector were first evaluated. Then, combining the line shape calculation and Monte Carlo simulation of the Lyman-α photon emission, we estimated spectroscopy precisions achievable for a few months of the data-taking. In the first measurement to be conducted without the HFS, the simulation predicts a spectroscopy precision of 10% assuming the $\bar{\mathrm{H}}$ production rate of 0.1 $\bar{\mathrm{H}}$ atoms per AD cycle. In the high-precision measurement to be conducted with both the HFS and MWS, the simulation predicts a

precision on the order of 100 ppm supposing a $\bar{\mathrm{H}}$ production rate of 10^4 per AD cycle, which is evaluated from the GBAR proposal.

Additionally, we performed some commissioning of the Lyman-α detector. Through an experiment using a UV LED photon source, responses of the UV photons to the Lyman-α detector were characterized under certain configurations. In another experiment using an atomic beam of H, degradation of the detection efficiency was indicated, which is probably due to deliquescency of CsI coated on MCPs in the Lyman-α detector. Furthermore, we carried out background measurements of the $\bar{\mathrm{H}}$ Lamb shift spectroscopy by using the $\bar{p}$ beam extracted from the $\bar{p}$ trap for the first time. As a consequence of upgrading the MW spectrometer to the larger bore model, and using the trap-extracted $\bar{p}$ beam with the Ps cavity target, the measured count rate was confirmed to be much lower than before. In another background measurement, we completely annihilated the $\bar{p}$ beam on a gate valve before the spectroscopy setup, and observed surprisingly long time spectrum of the background signal. The result implies delayed background signals contributed by a slow component of the beam, radioactive decay of unstable nuclei, backscattered $\bar{p}$s, and so on.

Lastly, this research contributed to the data-taking and analysis of the $\bar{\mathrm{H}}$ production experiments conducted for the first time by the GBAR collaboration. In the initial experiment conducted in the beam time of 2022, the Ps flat target was employed, and datasets comprising several thousand AD cycles were recorded for both the MIX and BGD modes. Our analysis of waveforms and images from the $\bar{\mathrm{H}}$ detector confirmed the $\bar{\mathrm{H}}$ production with a statistical significance of approximately 3σ in both analyses. This marked the world's first demonstration of $\bar{\mathrm{H}}$ synthesis via charge-exchange reaction (2.1) in the keV energy regime. The follow-up experiment in 2024 saw a number of improvements by the GBAR collaboration in both the e^+ and $\bar{p}$ beam lines. Notably, the $\bar{p}$ trap became operational, enabling the use of the Ps cavity target. Preliminary analysis of data obtained during this beam time indicates the $\bar{\mathrm{H}}$ production rate of nearly 0.1 $\bar{\mathrm{H}}$s per AD cycle, representing an almost tenfold improvement compared to the 2022 experiment. This enhanced production rate suggests the feasibility of the Lamb shift measurements with 10% spectroscopic precision, as numerically demonstrated in Section 5.6.

8.2 Prospects

8.2.1 Concerns of Lyman-α Detection

Increasing the $\bar{\mathrm{H}}$ production rate is one of the largest keys to the successful Lamb shift measurement. On the other hand, increasing the efficiency in the Lyman-α photon counting or improving the signal-to-noise ratio are also crucial to perform the data-taking within a realistic period of time.

Concerning the current Lyman-α detector, we have seen, in Section 6.2, that the detection efficiency for the Lyman-α photons probably have been degraded. Therefore, re-coating the MCPs with CsI would be worth attempting. The CsI re-coating and re-installation of the current Lyman-α detector are foreseen towards the middle of the beam time in 2025. After the re-installation, the UV photon measurement for the signal characterization and the observation of the Lyman-α photons using the H beam will be performed for commissioning the detector.

Concerning the reduction of the $\bar{p}$ background itself, a promising solution would be to collimate the beam as upstream as possible, regardless of the origins of the background, such as annihilation of $\bar{p}$s from the slow component of the beam, radioactive decay of unstable nuclei, or annihilation of the backscattered $\bar{p}$s. Also, the slow component of the

beam could be removed by applying a pulsed high voltage.

Besides, an undershoot has been observed in the signal time window on the waveform from the Lyman-α detector, due to the substantial amount of the $\bar{p}$ annihilation at the reaction chamber. To reduce the undershoot, it would be effective to gate the MCPs bias voltages so that the MCPs are biased only within the time window.

Meanwhile, the scheme of the Lyman-α detection itself could be revised. The detector is required to be sensitive to the Lyman-α photons, while being less sensitive to charged particles. A wavelength shifter, for example, could be a candidate that has good efficiency in converting the 122 nm Lyman-α photons to visible light. Using such a wavelength shifter in combination with a photomultiplier, the background signals would be lower than the current scheme.

8.2.2 Plans of Spectroscopy Measurement

During the $\bar{p}$ beam times in the coming years, the following measurements are anticipated, in accordance with the increase in the $\bar{\mathrm{H}}$ production rate.

Given the current $\bar{\mathrm{H}}$ production rate reaching the order of 0.1 $\bar{\mathrm{H}}$, and assuming the $2S$ state production ratio of 15% [45], and current Lyman-α detector's theoretical efficiency of 8(1)% as discussed in Section 5.5, the Lyman-α signal count rate is expected to be on the order of 0.001 per shot. If the background is completely removed, this count rate predicts 10 signals out of 10,000 shots, which means a significance of about 3 σ assuming a Poissonian count distribution. An observation of the Lyman-α photon signal with this significance will probably be first targeted, in an experiment switching the MW frequency on-resonance and off-resonance. By taking coincidences with the signals at the $\bar{\mathrm{H}}$ detector, the production ratio of $\bar{\mathrm{H}}$(2S) atoms can be evaluated in this measurement, determining the cross-section of $\bar{\mathrm{H}}$(2S) synthesis in the charge-exchange reaction (2.1). This will be followed by the first line shape measurement of the Lamb shift at 10% spectroscopy precision, as theoretically demonstrated in the Monte Carlo simulation described in Section 5.6. These measurements would be performed by the middle of the beam time in 2026.

Then, the LS3, a long shutdown of the accelerator complex in CERN, is planned until 2029. After the LS3, the high-precision line shape measurement will be worked on aiming at a precision on the order of 100 ppm, as theoretically demonstrated in the Section 5.7. At this stage, the world's first determination of the antiproton charge radius would be demonstrated.

Towards a spectroscopy precision comparable to that achieved in H Lamb shift measurement, the Ramsey method [8] can be applied to our setup. For the H Lamb shift, The Ramsey spectroscopy has achieved a precision of 9 ppm with the PCR determined to 3% precision [7]. If such a high-precision measurement is accomplished in our case as well, it would open up the possibility of testing CPT symmetry through a comparison of the PCR and antiproton charge radius.

Besides, the similar spectroscopic technique can be applied to measure the resonance frequency of the $2S_{1/2}$-$2P_{3/2}$ fine structure transition. By combining the fine structure spectroscopy with the theoretical value of the $2P_{1/2}$-$2P_{3/2}$ energy split, the $2S_{1/2}$-$2P_{1/2}$ Lamb shift can also be studied. The designing of the MW spectrometer for the fine structure spectroscopy is in progress in our group.

Bibliography

[1] W.E. Lamb and R.C. Retherford, *Phys. Rev.*, **72**, 241 (1947).

[2] W.E. Lamb and R.C. Retherford, *Phys. Rev.*, **79**, 549 (1950).

[3] H. A. Bethe, *Phys. Rev.* **72**, 339 – 341 (1947).

[4] V.A. Yerokhin, *Ann. Phys.* **531**, 1800324 (2019).

[5] R. Hofstadter and R. W. McAllister, *Phys. Rev.* **98**, 217 (1955).

[6] G. Newton *et al.*, *Philos. Trans. R. Soc. A*, **290**, 35 (1979).

[7] S. R. Lundeen and F. Pipkin, *Metrologia* **22**, 9 (1986).

[8] N. F. Ramsey, *Phys. Rev.*, **76**, 996 (1949).

[9] N. Bezginov *et al.*, *Science*, **365**, 1007 (2019).

[10] R. Pohl *et al.*, *Nature*, **466**, 213 (2010).

[11] A. Antognini *et al.*, *Science* **339**, 417 – 420 (2013).

[12] P. J. Mohr *et al.*, *Rev. Mod. Phys.* **84**, 1527 (2012).

[13] X. Zhan *et al.*, *Phys. Lett. B* **705**, 59-64 (2011).

[14] A. Beyer, *et al.*, *Science*, **358**, 6359 (2017).

[15] H. Fleurbaey *et al.*, *Phys. Rev. Lett.* **120**, 183001 (2018).

[16] A. Marsman *et al.*, *Phys. Rev. A* **98**, 012509 (2018).

[17] W. Xiong, *et al.*, *Nature* **575**, 7781, 147-150 (2019).

[18] A. Grinin, *et al.*, *Science*, **370**, 6520 (2020).

[19] A. D. Brandt *et al.*, *Phys. Rev. Lett.*, **128**, 023001 (2022).

[20] P. Mohr, E. Tiestinga *et al.*, CODATA 2022 (`https://physics.nist.gov/constants`) (Accessed December 20, 2024)

[21] R. Bluhm *et al.*, *Phys. Rev. Lett.*, **82**, 2254 (1999).

[22] V. A. Kostelecký and A. J. Vargas, *Phys. Rev. D*, **92**, 056002 (2015).

[23] G. Baur *et al.*, *Phys. Lett. B* **368**, 251-258 (1996).

[24] G. Blanford *et al.*, *Phys. Rev. Lett.*, **80**, 3037 (1998).

[25] C. Alanzeau *et al.*, 10.5170/CERN-2014-002 (2014).

[26] W. Bartmann *et al.*, *Philos. Trans. R. Soc. A* **376**, 20170266 (2017).

[27] D. Gamba *et al.*, 10.18429/JACoW-COOL2023-THPAM1R3 (2023).

[28] The ALPHA collaboration, CERN-SPSC-2005-006/SPSC-P-325 (2005).

[29] E. Widmann *et al.*, *Hyperfine Interact.* **215**, 1 (2013).

[30] M. Diermaier *et al.*, *Hyperfine Interact.* **233**, 35-40 (2015).

[31] The ASACUSA collaboration, CERN-SPSC-2019-035/SPSC-P-307-ADD-2 (2019).

[32] M. Ahmadi *et al.*, *Nature* **548**, 66-69 (2017).

[33] M. Ahmadi *et al.*, *Nature* **557**, 71-75 (2018).

[34] M. Ahmadi *et al.*, *Nature* **561**, 211-215 (2018).

[35] M. Ahmadi *et al.*, *Nature* **578**, 375-380 (2020).

[36] The GBAR Collaboration, CERN-SPSC-2011-029/SPSC-P-342 (2011).

[37] P. Perez and Y. Sacquin, *Classical Quantum Gravity* **29**, 184008 (2012).

[38] P. Indelicato *et al.*, *Hyperfine Interact.* **228**, 141 (2014).

[39] P. Perez *et al.*, *Hyperfine Interact.*, **233**, 21 (2015).

[40] The AEgIS collaboration, CERN-SPSC-2007-017/SPSC-P-334 (2007).

[41] S. Aghion *et al.*, *Nat. Commun.*, **5**, 4538 (2014).

[42] J. Storey *et al.*, *Hyperfine Interact.*, **228**, 151 (2014).

[43] E. K. Anderson *et al.*, *Nature* **621**, 716-722 (2023).

[44] P. Adrich *et al.*, *Eur. Phys. J. C*, **83**, 1004 (2023).

[45] C. M. Rawlins *et al.*, *Phys. Rev. A* **93**, 012709 (2016).

[46] P. Crivelli *et al.*, *Phys. Rev. D*, **94**, 052008 (2016).

[47] N. Kuroda *et al.*, *J. Phys. Conf. Ser.*, **875**, 022054 (2017).

[48] K. Lévêque-Simon and P.-A. Hervieux, *Phys. Rev. A*, **107**, 052813 (2023).

[49] P. Comini *et al.*, *New J. Phys.* **23** 029501 (2021).

[50] P. Comini and P.-A. Hervieux, *New J. Phys.*, **15**, 095022 (2013).

[51] P. Comini *et al.*, *Hyperfine Interact.*, **228**, 159-165 (2014).

[52] P. Comini, Ph.D. Thesis, Université Pierre et Marie Curie - Paris VI (2014).

[53] K. Lévêque-Simon, Ph.D. Thesis, Université de Strasbourg (2020).

[54] T. Yamashita *et al.*, *New J. Phys.*, **23**, 012001 (2021).

[55] T. Yamashita *et al.*, *Phys. Rev. A*, **105**, 052812 (2022).

[56] C. Roumegou, Ph.D Thesis, Université Paris-Saclay, France (2023).

[57] J. P. Merrison *et al.*, *Phys. Rev. Lett.*, **78(14)**, 2728 – 2731 (1997).

[58] SPHINX, French ANR funded project, ANR-22-CE31-0019-01.

[59] GBAR Collaboration, CERN-SPSC-2024-006/SPSC-SR-341 (2024).

[60] GBAR Collaboration, CERN-SPSC-2022-003/SPSC-SR-302 (2022).

[61] A. Husson *et al.*, *Nucl. Inst. Methods Phys. Res. A*, **1002** (2021).

[62] Kyoung-Hun Yoo *et al.*, *J. Instrum.*, **17**, T10003 (2022).

[63] M. Charlton *et al.*, *Nucl. Inst. Methods Phys. Res. A*, **985** (2021).

[64] P. Blumer *et al.*, *Nucl. Inst. Methods Phys. Res. A*, **1040** 167263 (2022).

[65] J. R. Danielson *et al.*, *Rev. Mod. Phys.*, **87**, 247 (2015).

[66] A. M. M. Leite, Ph.D Thesis, Université Paris-Saclay, France (2017).

[67] S. Niang, Ph.D Thesis, Université Paris-Saclay, France (2020).

[68] D. A. Cooke, *J. Phys. B*, **49**, 014001 (2015).

[69] N. Kuroda *et al.*, *Phys. Res. ST. AB*, **15(2)**, 024702 (2012).

[70] R. G. Greaves and C. M. Surko., *Phys. Rev. Lett.*, **85(9)**, 1883-1886 (2000).

[71] R. G. Greaves and C. M. Surko., *Phys. Plasmas*, **8(5)**, 1879-1885 (2001).

[72] G. Janka *et al.*, *Eur. Phys. J. C* **80**, 804, (2020).

[73] N. Kolachevsky *et al.*, *Phys. Rev. Lett.*, **102**, 213002 (2009).

[74] S. Lundeen *et al.*, *Phys. Rev. Lett.*, **34**, 377 (1975).

[75] A. Kramida, *At. Data and Nucl. Data Tables*, **96**, 6, 586-644 (2010).

[76] W. Demtröder, Atoms, Molecules and Photons An Introduction to Atomic-, Molecular-, and Quantum Physics (2nd ed.), Springer Berlin, Heidelberg (2010).

[77] G. W. F. Drake, *Adv. At. Mol. Phys.*, **18**, 399-460, (1982).

[78] J. L. Wiza *et al.*, *Nucl. Inst. Methods Phys. Res.*, **162(1-3)**, 587 601 (1979).

[79] G. Janka, Ph.D. Thesis, ETH Zürich (2022).

[80] S. R. Jelinsky *et al.*, *Proc. SPIE*, **2808** (1996).

[81] O. Siegmund *et al.*, *Proc. SPIE*, **5920** (2005).

[82] O. H. W. Siegmund *et al.*, *Proc. SPIE*, **10397** (2017).

[83] B. Ohayon *et al.*, *Phys. Rev. Lett.* **128**, 011802 (2022).

[84] G. Janka *et al.*, *Nat. Commun.* **13**, 7273 (2022).

[85] A. Husson, Ph.D Thesis, Université Paris-Saclay, France (2018).

[86] B. M. Latacz, Ph.D Thesis, Université Paris-Saclay, France (2019).

[87] T. A. Tanaka *et al.*, *Interactions*, **245**, 30 (2024).

[88] URL: `https://www.cst.com`

[89] T. A. Tanaka, Master Thesis, The University of Tokyo (2020).

[90] P. Virtanen *et al.*, *Nature Methods*, **17(3)**, 261 – 272 (2020).

[91] A. van Wijngaarden and G. W. F. Drake, *Phys. Rev. A*, **17**, 1366 (1978).

[92] F. Bloch and A. Siegert, *Phys. Rev.*, **57**, 522 (1940).

[93] H. Amano *et al.*, *J. Phys. D*, **53**, 503001 (2020).

[94] M. Gonin *et al.*, *Rev. Sci. Instrum.*, **65(3)**, 648-652 (1994).

[95] F. Allegrini *et al.*, *J. Geophys. Res. Space Phys.*, **121(5)**, 3931 – 3950 (2016).

[96] N. Takahashi *et al.*, *Nucl. Inst. Methods Phys. Res. B*, **315**, 51-54 (2013).

[97] J. F. Ziegler, SRIM-2013 software package, `http://www.srim.org.`

[98] S. Agostinelli *et al.*, *Nucl. Inst. Methods Phys. Res. A*, **506**, 250-303 (2003).

[99] J. Allison *et al.*, *IEEE Trans. Nucl. Sci.*, **53**, 270-278 (2006).

[100] J. Allison *et al.*, *Nucl. Inst. Methods Phys. Res. A*, **835**, 186-225 (2016).

[101] A. Bianconi *et al.*, *Phys. Rev. A* **78**, 022506 (2008).

[102] A. Bianconi *et al.*, *Hyperfine Interact.* **194**, 297 – 303 (2009).

[103] A. Deller *et al.*, *New J. Phys.*, **17**, 043059 (2015).

[104] D.B. Cassidy *et al.*, *Phys. Rev. A*, **81**, 012715 (2010).

[105] M. W. Heiss, Ph.D. Thesis, ETH Zürich (2021).

[106] R. M. Haralick and L. G. Shapiro. *Comput. Gr. Image Process.*, **29(1)**, 100-132 (1985).

[107] S. Van der Walt *et al.*, *PeerJ*, **2**, 453 (2014).

Acknowledgement

はじめに、本研究の指導教官である松田恭幸教授に深く御礼申し上げます。松田教授には、本研究へのご指導に加え、海外出張の手続きや生活面においてもご支援を頂きました。また、就職についての相談にも何度も付き合って頂き、大変感謝しております。また、黒田直史助教に深く御礼申し上げます。博士課程では CERN への長期滞在の機会を与えて頂き、本研究においては最も懇切にご指導を賜りました。本研究の共同研究者である浅利真奈美氏、田中香津生氏、樋口嵩氏、Philipp Blumer 氏、Gianluca Janka 氏、Ben Ohayon 氏、Christian Regenfus 氏、Paolo Crivelli 氏にも感謝致します。皆様との度重なる議論のおかげで、本研究を遂行することが出来ました。また、GBAR collaboration の皆様には、本研究を支えて頂いただけでなく、スイス・フランスでの生活をサポートして頂きました。大変感謝しております。そして何より、五年間ものあいだ私を精神的かつ経済的に支えてくれた父、母、兄に深く感謝致します。